

**Modeling Flow Regimes in Porous Media: Correcting
Permeability Models by Combining Numerical
Simulation and Experimentation**

by

Rasoul Arabjamaloei

A Thesis submitted to the Faculty of Graduate Studies of
The University of Manitoba
in partial fulfillment of the requirements of the degree of

DOCTOR OF PHILOSOPHY

Department of Mechanical Engineering
University of Manitoba
Winnipeg
Canada

Copyright © 2017 by Rasoul Arabjamaloei

ABSTRACT

In this research, single phase flow regimes in porous media were studied both numerically and experimentally to determine methods to predict the effects of rarefied gas flow and inertial flow. The results of this research were initially compared with the conventional methods of treating rarefied gas flow, the Klinkenberg equation and inertial flow, the Forchheimer equation. In the first section of the research, the slip condition for rarefied gas flow in low permeability, two-dimensional simple porous media was studied by the Lattice Boltzmann method (LBM) and new corrections to the Klinkenberg model and higher order slip models were investigated. To apply LBM, new corrections were introduced to the solid-fluid boundary condition and a new relationship was proposed to relate LBM viscosity and Knudsen number. To validate the LBM model, the slip flow simulation results were compared to analytical methods and experimentation. It was shown that the modified LBM simulator was capable of predicting the experimentally observed Knudsen minimum. By comparing the numerical simulation results with analytical models extracted from the up-to-date literature, the analytical model that most closely matched numerical model results was identified.

In the second section of this research, the apparent permeability reduction due to inertial effects in simple and complex porous structures was studied. LBM based simulator was developed to model single-phase three-dimensional fluid flow in porous media. The simulator was verified by experimental and analytical solution tests and then was implemented to study high Reynolds number flow processes in irregular shaped porous structures. The effects of inertial on the onset and extent of non-Darcy flow in different

geometries was studied. It was shown that the Forchheimer equation does not accurately fit the high Reynolds number flow. A new empirical correlation was proposed that correlates the scaled permeability and mass flow rate relationship very well and is more accurate than the Forchheimer equation. To validate the LBM, a modified experimental technique was designed and utilized to analyze permeability and mass flow rate relationships in high Reynolds number flows. The experimental results showed that the correlation in the present research is far more accurate than the Forchheimer equation.

ACKNOWLEDGEMENTS

I would like to express my extreme thanks to Professor Douglas Ruth, for his continuous guidance and wise supervision throughout the course of my research work. I would also like to thank Mr. Zeev Kapitanker for his assistance in setting up the unsteady state core flow test instruments. Also, my sincere thanks goes to the examination committee (Professor Bing-Chen Wang, Professor Qiang (Chong) Zhang and Professor Steven Bryant), for their time and valuable input in this thesis. The financial Support for this work provided by the National Science and Engineering Research Council of Canada is much acknowledged.

DEDICATION

I would like to dedicate this thesis to my lovely parents who supported me during every single stage of my life including my academic career.

TABLE OF CONTENTS

ABSTRACT.....	i
ACKNOWLEDGEMENTS.....	iii
DEDICATION.....	iv
TABLE OF CONTENTS.....	v
LIST OF TABLES.....	vii
LIST OF FIGURES.....	viii
NOMENCLATURE.....	xiv
1 CHAPTER 1: INTRODUCTION.....	1
2 CHAPTER 2: LITERATURE SURVEY.....	6
2.1 Rarefied-Gas Flow and Slip Effects.....	7
2.2 Laminar Inertial Effects.....	11
2.3 The Pulse-Decay Method.....	16
3 CHAPTER 3: NUMERICAL METHOD AND EXPERIMENTAL SET-UP.....	19
3.1 The Kinetic Theory and the Lattice Boltzmann Method.....	19
3.1.1 The Kinetic Theory and the Boltzmann Equation.....	19
3.1.2 The Lattice Boltzmann Method.....	24
3.2 LBM Model Validation.....	36
3.2.1 2D LBM Model Validation.....	37
3.2.2 3D LBM Model Validation.....	40
3.3 Experiment Set-Up.....	45
4 CHAPTER 4: SLIP EFFECTS AND THE KLINKENBERG MODEL.....	51
4.1 Theoretical Study.....	51

4.2	Numerical Study.....	56
4.2.1	Higher than Navier-Stokes Level Knudsen Accuracy	59
5	CHAPTER 5: LAMINAR INERTIAL EFFECTS AND THE FORCHHEIMER MODEL	75
5.1	Numerical Study.....	75
5.2	Unsteady-State Core Flow Tests	93
6	CONCLUSIONS AND RECOMMENDATIONS FOR FUTURE WORKS	101
6.1	Conclusions	101
6.2	Recommendations for Future Studies	104
7	BIBLIOGRAPHY	106
A.	APPENDIX A.....	112
B.	APPENDIX B	115
C.	APPENDIX C	117

LIST OF TABLES

Table 2-1: Rarefied-gas flow regimes characterized by specified Kn range.	6
Table 2-2: Correlations relating the Forchheimer coefficient (β) to porous medium properties.....	13
Table 2-3: Flow regimes classified by the critical and transitional Reynolds number.	16
Table 3-1: Velocity and weight sets for D2Q9.	29
Table 3-2: Velocity and weight sets for D2Q21.	29
Table 3-3: Velocity and weight sets for D2Q37.	29
Table 3-4: Velocity and weight sets for D3Q15.	30
Table 3-5: Physical and LBM dimension conversion relationships.	38
Table 3-6: Physical and lattice properties used to test the developed LBM simulator.	41
Table 4-1: Different relationships between the relaxation time, viscosity and Kn in the literature.	63
Table 4-2: Reported values in the literature for the constants in equation 4.6.	68
Table 4-3: Correlated values of C_1 and C_2 for different ranges of Kn.....	70
Table 4-4: Correlated values of C_1 and C_2 for different ranges of Kn.....	71
Table 5-1: The schematics and characteristics of the different porous structures used to study the inertial effects in body force driven flow.	77
Table 5-2: List of parameters applied in mesh size effect analysis	78
Table 5-3: List of parameters applied in viscosity effect analysis.....	80
Table 5-4: The specifications of the tube combinations designed for flow tests.....	94

LIST OF FIGURES

Figure 3-1: Schematic of D2Q9 velocity set.....	27
Figure 3-2: a) The on-lattice velocity component and b) the off-lattice velocity component. Here the black dots show the lattice nodes and the arrows show a discrete velocity vectors.	30
Figure 3-3: Flowchart showing the algorithm for applying the Lattice Boltzmann method. This algorithm could be modified for various boundary and inlet-outlet conditions.	31
Figure 3-4: The bounceback boundary condition. The incoming flux from the lattice nodes (black filled circles) towards the wall are reflected in the opposite direction in one time step. The fictitious nodes in the solid wall (shown by circles) are placed just for clarification. Here the discrete velocities are color coded, the solid lines are the incoming flux and the dashed lines are the reflected flux.....	32
Figure 3-5: The half-way bounceback boundary condition. The incoming flux from the lattice nodes (black filled circles) towards the wall are reflected in the opposite direction in one time step. The fictitious nodes in the solid wall (shown by circles) are placed just for clarification. Here the discrete velocities are color coded, the solid lines are the incoming flux and the dashed lines are the reflected flux.	33
Figure 3-6: The specular boundary condition. The incoming flux from the lattice nodes (black circles) towards the wall are reflected like a mirror surface. The fictitious nodes in the solid wall are placed just for clarification. Here the discrete velocities are color coded, the solid lines are the incoming flux and the dashed lines are the reflected flux.	34
Figure 3-7: Schematic of the velocity set at the inlet and the outlet of the channel.	35
Figure 3-8: Schematic of the 2D channel. The parabolic curve and arrows are used to display the fully developed velocity profile.....	37
Figure 3-9: Velocity profiles obtained by LBM and analytical solution of NSE.	39

Figure 3-10: Streamwise velocity predicted by LBM and solution of NSE for the body force driven flow in circular pipe. Here $u(y)$ shows the velocity at distant y from one of the walls towards the center of the pipe.....	41
Figure 3-11: Schematic of varying diameter circular pipe designed to test the LBM simulator.	42
Figure 3-12: Gravity drainage test set-up designed to find the permeability of the sample.	43
Figure 3-13: LBM predicted scaled permeability and mass flow rate in SI units.	45
Figure 3-14: The modified pulse-decay experimentation apparatus.....	46
Figure 3-15: A schematic of the proposed set-up for the modified step-decay gas flow test.	47
Figure 3-16: the upstream (a) and downstream (b) pressure change vs. the incremental volume (kPa vs. m^3).....	49
Figure 3-17: A sample of pressure recordings for a 3-stage flow test.	49
Figure 4-1: Schematic of the flow channel. The arrows and the parabolic curve represent the parabolic velocity profile.	52
Figure 4-2: Kn range for low permeability and different mean hydrostatic pressure.....	55
Figure 4-3: Velocity profiles and velocity at the wall for different r_f and $\vartheta=0.0025$	57
Figure 4-4: Velocity profiles and velocity at the wall for different r_f and $\vartheta=0.025$	57
Figure 4-5: Velocity profiles and velocity at the wall for different r_f and $\vartheta =0.25$	57
Figure 4-6: Velocity profiles and velocity at the wall for different r_f and $\vartheta=2.5$	58
Figure 4-7: Non-dimensional flow rate (Q) for a wide range of reflection coefficient (r_f).	59
Figure 4-8: The half-way bounceback process in D2Q21. The velocity vectors are color coded. The solid arrows show the incoming flux towards the wall and the dashed arrows show the reflected flux.....	62

Figure 4-9: Velocity profiles and velocity ratio at the wall for different Knudsen numbers using D2Q9 model. Here U_w is the bulk velocity at the wall and U_{max} is the maximum bulk velocity which happens at the center of the channel.	65
Figure 4-10: Velocity profiles and velocity ratio at the wall for different Knudsen numbers using D2Q21 model. Here U_w is the bulk velocity at the wall and U_{max} is the maximum bulk velocity which happens at the center of the channel.	65
Figure 4-11: Velocity profiles and velocity ratio at the wall for different Knudsen numbers using D2Q37 model. Here U_w is the bulk velocity at the wall and U_{max} is the maximum bulk velocity which happens at the center of the channel.	66
Figure 4-12: Prediction of mass flow rate (Q) with different orders of Hermite polynomials and velocity sets.	66
Figure 4-13: Prediction of the ratio of apparent permeability (K) and absolute permeability (K_{abs}) with different orders of Hermite polynomials and velocity sets. H2 in the legend shows the 2 nd order expansion on Hermite polynomials.	67
Figure 4-14: The ratio of the gas permeability (K) to the absolute value of permeability (K_{abs}) for a range of Kn	69
Figure 4-15: The permeability prediction by the LBM model and equation 4.6.....	70
Figure 4-16: The permeability ratio prediction by LBM and equation 4.6 with three different sets of constants from table 4-3.....	71
Figure 4-17: The permeability ratio prediction by LBM and equation 4.6 with different sets of constants for different Kn ranges from table 4-4.....	72
Figure 4-18: The permeability ratio prediction by LBM and equation 4.6 with C_1 set to 1 for Kn range of 0-10.	72
Figure 4-19: The permeability ratio prediction by LBM and equation 4.6 with C_1 set to zero for Kn range of 0-10.	73
Figure 5-1: The LBM predicted scaled permeability (k_s) and mass flow rate relationship with the Forchheimer equation prediction.	75

Figure 5-2: The streamwise velocity profile at the exit of the pipe-cube porous structure for 4 different mesh sizes and the relative difference(Diff.) velocity profile of each case with respect the highest resolution case.....	79
Figure 5-3: The streamwise velocity profiles at the exit of the pipe-cube structure for 4 different viscosity values and the relative difference (Diff.) of each case with respect to case#2.....	80
Figure 5-4: Scaled permeability vs. mass flow rate for a range of body force acceleration and the best Forchheimer equation fit for the pipe-sphere structure. a) Data fitted for the whole range of \dot{m} b) Data fitted after non-Darcy onset.	82
Figure 5-5: Scaled permeability vs. mass flow rate for a range of body force acceleration and the best Forchheimer equation fit for the pipe-cube structure. a) Data fitted for the whole range of \dot{m} b) Data fitted after non-Darcy onset.	82
Figure 5-6: Scaled permeability vs. mass flow rate for a range of body force acceleration and the best Forchheimer equation fit for the pipe-ellipsoid structure. a) Data fitted for the whole range of \dot{m} b) Data fitted after non-Darcy onset.	83
Figure 5-7: Scaled permeability vs. mass flow rate for a range of body force acceleration and the best Forchheimer equation fit for the bent channel structure. a) Data fitted for the whole range of \dot{m} b) Data fitted after non-Darcy flow onset.....	83
Figure 5-8: Scaled permeability vs. mass flow rate for a range of body force acceleration and the best Forchheimer equation fit for the pipe-throat structure. a) Data fitted for the whole range of \dot{m} b) Data fitted after non-Darcy onset.	84
Figure 5-9: The linear and semi-log plots of mass flow rate in lattice units and scaled permeability for the pipe-ellipsoid structure in table 5-3.....	85
Figure 5-10: The linear and semi-log plots of mass flow rate in lattice units and scaled permeability for the pipe-cube structure in table 5-3.....	85
Figure 5-11: Velocity contours at a range of mass flow rate at the middle plane of the pipe-ellipsoid structure. The absolute black color shows the solid part and the brightness of the color inside the brown channel represents the flow velocity.....	87

Figure 5-12: Velocity contours at a range of mass flow rate at the middle plane of the pipe-cube structure. The absolute black color shows the solid part and the brightness of the color inside the brown channel represents the flow velocity.88

Figure 5-13: The schematic of the Berea sandstone porous structure. The black fill represents the solid part and the white fill is the void space. The length of each side of the cube is 1mm (Imperial College London Website, 2016).90

Figure 5-14: The mass flow rate in lattice units and scaled permeability relationship for the Berea porous rock sample. The two graphs are generated for two ranges of mass flow rates.90

Figure 5-15: The linear and semi-log plot of mass flow rate in lattice units and scaled permeability for the Berea sandstone structure and the new proposed correlation fit.92

Figure 5-16: Left: The pressure decay profile of upstream chamber (P_u) and the downstream pressure profile (P_d). Right: The scaled permeability vs. mass flow rate in a semi-log plot for the structure#1.95

Figure 5-17: Left: The pressure decay profile of upstream chamber (P_u) and the downstream pressure profile (P_d). Right: The scaled permeability vs. mass flow rate in a semi-log plot for the structure#2.96

Figure 5-18: Left: The pressure decay profile of upstream chamber (P_u) and the downstream pressure profile (P_d). Right: The scaled permeability vs. mass flow rate in a semi-log plot for the structure#3.96

Figure 5-19: Left: The pressure decay profile of upstream chamber (P_u) and the downstream pressure profile (P_d). Right: The scaled permeability vs. mass flow rate in a semi-log plot for the structure#4.97

Figure 5-20: Left: The pressure decay profile of upstream chamber (P_u) and the downstream pressure profile (P_d). Right: The scaled permeability vs. mass flow rate in a semi-log plot for the structure#5.97

Figure 5-21: Comparison of scaled permeability fitting of the proposed model (equation 5.1) and the Forchheimer model (equation 2.3) by experimental results of structure#1. ...98

Figure 5-22: Comparison of scaled permeability fitting of the proposed model (equation 5.1) and the Forchheimer model (equation 2.3) by experimental results of structure#2. .	98
Figure 5-23: Comparison of scaled permeability fitting of the proposed model (equation 5.1) and the Forchheimer model (equation 2.3) by experimental results of structure#3. .	99
Figure 5-24: Comparison of scaled permeability fitting of the proposed model (equation 5.1) and the Forchheimer model (equation 2.3) by experimental results of structure#4. .	99
Figure 5-25: Comparison of scaled permeability fitting of the proposed model (equation 5.1) and the Forchheimer model (equation 2.3) by experimental results of structure#5. .	100
Figure B-1: The schematic of the falling head permeameter apparatus. H is the height of the water tank to be drained through the porous sample. Z is the height of the sample. Arrows represent the flow direction. .	115
Figure C-1: The semi-log plots of mass flow rate in lattice units and scaled permeability for the pipe-sphere structure in table 5-1. .	117
Figure C-2: The semi-log plots of mass flow rate in lattice units and scaled permeability for the bent pipe structure in table 5-1. .	117
Figure C-3: The semi-log plots of mass flow rate in lattice units and scaled permeability for the throat structure in table 5-1. .	118
Figure C-4: The plot of mass flow rate in lattice units and scaled permeability predicted by LBM simulation for the pipe-sphere structure fitted with equation 5.1. .	118
Figure C-5: The plot of mass flow rate in lattice units and scaled permeability predicted by LBM simulation for the pipe-cube structure fitted with equation 5.1. .	119
Figure C-6: The plot of mass flow rate in lattice units and scaled permeability predicted by LBM simulation for the pipe-ellipsoid structure fitted with equation 5.1. .	119
Figure C-7: The plot of mass flow rate in lattice units and scaled permeability predicted by LBM simulation for the bent pipe structure fitted with equation 5.1. .	120
Figure C-8: The plot of mass flow rate in lattice units and scaled permeability predicted by LBM simulation for the throat structure fitted with equation 5.1. .	120

NOMENCLATURE

Lattice Boltzmann (Dimensionless)

A	<i>Area (m^2)</i>
D	<i>Number of space dimensions</i>
\vec{F}_i	<i>External body force</i>
H	<i>Height (m)</i>
Kn	<i>Knudsen number (dimensionless)</i>
L_0	<i>Characteristic length (m)</i>
M_0	<i>Characteristic mass (kg)</i>
P	<i>Hydrostatic pressure (Pa)</i>
Q	<i>Number of discrete velocity vectors</i>
R	<i>Radius (m)</i>
Re	<i>Reynolds number (dimensionless)</i>
T_0	<i>Characteristic time (s)</i>
U	<i>Potential energy from the external force</i>
V	<i>Volume (m^3)</i>
$V_{(2)}$	<i>Two-body interaction force</i>
W	<i>Width (m)</i>
\vec{a}	<i>Acceleration from external body force</i>
\vec{c}	<i>Velocity vector</i>
\vec{c}_i	<i>Discretized velocities</i>
c_s	<i>Speed of sound</i>
e	<i>Internal energy</i>
f	<i>Particle distribution function</i>
f^{eq}	<i>Equilibrium distribution function</i>
\vec{g}	<i>Acceleration from external body force</i>
k	<i>Permeability (m^2)</i>
k_s	<i>Scaled permeability (dimensionless)</i>
k''_s	<i>Second derivative of k_s with \dot{m}</i>

\dot{m}	<i>Mass flow rate (kg/s)</i>
\vec{p}	<i>Momentum</i>
q	<i>Volumetric flow rate (m³/s)</i>
r	<i>Radius (m)</i>
t	<i>Time</i>
u	<i>Streamwise velocity (m/s)</i>
\hat{u}	<i>Bulk speed</i>
\vec{u}	<i>Bulk velocity vector</i>
w_i	<i>Weights associated with different lattice velocities</i>
\vec{x}	<i>Location</i>
z	<i>Length (m)</i>
Φ	<i>Piezometric pressure (atm)</i>
$\Delta\hat{t}$	<i>Time step</i>
Δx	<i>Grid spacing (m)</i>
$\Delta\hat{x}$	<i>Lattice spacing</i>
μ	<i>Dynamic viscosity (Pa.s)</i>
$\hat{\nu}$	<i>Lattice viscosity</i>
ρ	<i>Fluid density (kg/m³)</i>
$\hat{\rho}$	<i>Bulk density in lattice units</i>
σ	<i>Stress tensor</i>
τ	<i>Relaxation time</i>

CHAPTER 1: INTRODUCTION

The Darcy law provides a basic linear equation for single-phase fluid flow in porous media in idealized conditions. The one-dimensional Darcy equation relates the fluid dynamic viscosity μ , the porous medium permeability k , the flow area A , the medium length L and the piezometric pressure difference $\Delta\Phi$ to the volumetric fluid flow rate through the porous sample q , as:

$$q = \frac{kA \Delta\Phi}{\mu L} \quad (1.1)$$

The piezometric pressure difference is caused by the hydrostatic pressure difference ΔP and the elevation difference of the two ends of the sample Δz , as:

$$\Delta\Phi = \Delta P + \rho g \Delta z \quad (1.2)$$

In the above equation, ρ is the density of the injected fluid and g is the gravitational acceleration.

It is generally accepted that the validity of the Darcy equation for a porous medium is dependent on the size of the pores as compared to the mean-free path of molecules characterized by the Knudsen number Kn , and on the flow regime characterized by the Reynolds number Re (Dullien 1992). The Knudsen number is a dimensionless number representing the ratio of the mean free path of the gas molecules to the width of the flow path as:

$$Kn = \frac{\lambda}{W} \quad (1.3)$$

where λ is the mean free path of the molecules and W is the width of the flow path. The Reynolds number is defined as the ratio of the inertial forces to viscous forces as:

$$Re = \frac{\rho u W}{\mu} \quad (1.4)$$

where ρ is the fluid density, u is the streamwise velocity, W is the flow path width and μ is the dynamic viscosity.

The phenomena that cause invalidity of Darcy equation are typically termed “non-Darcy effects”. Non-Darcy effects occur either at low pressure in rarefied gas flow, where molecular slippage at the solid-fluid contact and gas rarefaction affects the flow regime, or in high Re flow where laminar inertial effects are dominant. The slippage and rarefaction effects occur mostly in low permeability porous media (*e.g.* tight gas reservoirs) and the inertial effects occur mostly in high permeability porous media (*e.g.* gravel and aggregates). The objective of the present study was to model and simulate these two phenomena in porous media and to correct the existing mathematical models that are used to characterize these effects.

Tight gas reservoirs are of prominent importance among unconventional petroleum reserves. Due to the complicated flow dynamics of gas in tight porous media, corrections have to be applied to the Darcy equation so that it can properly predict gas flow dynamics. As the mean pore width of tight rocks (*e.g.* shales) decreases, the ratio of the mean free path to the pore width rises, that is when the Kn increases and gas rarefaction effects

becomes important – specifically, the condition of no-slip on the pore surface is violated. Proper treatments of these complexities have been attempted by using either classical continuum fluid mechanics approaches or by using kinetic theory of gases approaches.

The continuum fluid dynamics model, characterized by the Navier-Stokes equations (NSE), is an important tool used to study fluid hydrodynamics in a wide range of motions where the continuity assumption is valid. Going beyond the regime where the NSE are valid needs proper treatment of higher order velocity moments and slip condition effects. An example of the physical phenomena where the NSE cannot be directly applied is the case of rarefied gas flow in microchannels, where Kn approaches to values greater than unity (Gad-el-Hak 1999; Lockerby *et al.* 2005). Effectively, Kn is the parameter which determines how closely the flow system conforms to the continuum assumptions. The simplest method to correct the Darcy equation for high Kn effects is to use a “corrected” permeability.

The most well-known permeability correction to account for the existence of slip was presented by Klinkenberg (1941) as:

$$k = k_a \left(1 + \frac{b}{P} \right) \quad (1.5)$$

Here k is the corrected permeability, k_a is the intrinsic permeability (the permeability that would obtain if slip did not occur), P is the hydrostatic pressure, and b is a constant related to fluid and porous medium properties.

In the present research, rarefied gas flow in low permeability porous media was studied by the Lattice Boltzmann Method (LBM) and new corrections to the Klinkenberg model were investigated. These corrections allow the extension of the Klinkenberg model to higher ranges of Kn .

The Darcy equation has been shown to be valid in flow processes at sufficiently low Re (Muljadi *et al.* 2015). At higher Re , inertial effects cause extra hydrodynamic head losses and the Darcy equation becomes invalid. The Forchheimer equation is a semi-empirical relationship which accounts for inertial effects. The Forchheimer equation is written as:

$$-\frac{dP}{dx} = \frac{\mu u}{k} + \beta \rho u^2 \quad (1.6)$$

where β is termed the “Forchheimer coefficient”, μ is the dynamic viscosity of the fluid, u is the average streamwise velocity of the fluid, k is the permeability and ρ is the fluid density. The Forchheimer equation has been historically the most used model for predicting apparent permeability reduction due to inertial effects.

In the present research, laminar flow in simple porous structures was simulated by LBM to evaluate the capability of the Forchheimer equation to model permeability reduction due to inertial effects. The porous structures were designed so that the main geometrical effects including expansion, contraction and flow direction change were prominent. High Re flow was simulated in these structures, the permeabilities for a range of mass flow rate were calculated, and the effectiveness of the Forchheimer equation to match the simulation results was investigated. Furthermore, the numerical simulation results were used to develop a correlation that is more effective than the Forchheimer equation. All the

numerical simulations in this work were performed using custom codes developed in MATLAB scripts. High velocity flow tests were also performed to test the Forchheimer equation and the proposed correlation. The results showed that the proposed model correlates the permeability and mass flow rate relationship far more accurate than the Forchheimer equation.

In the following chapter, three sections contain summaries of up-to-date literature reviews of rarefied gas flow in porous media, inertial flow in porous media, and unsteady state flow tests. In chapter 3 the methods applied in the current research are discussed in two sections. In the first section, LBM and the kinetic theory behind it are explained, and the numerical simulator development and validation is discussed. In the second section of chapter 3, the experimental methods developed to validate the simulation results are explained. In chapter 4 the LBM results for high Kn flow are presented and discussed. The simulation and experimental flow tests for high Re flow are presented and discussed in Chapter 5. Chapter 6 contains conclusions and recommendations for future studies.

Parts of this thesis are based on material published in the Journal of Natural Gas Science and Engineering (Aabjamaloei *et al.* 2016). Permission was obtained from the publisher to use the contents of these articles in this thesis.

CHAPTER 2: LITERATURE SURVEY

Non-Darcy effects during fluid flow in porous media have been known and studied since the early 1900s. Non-Darcy effects can be classified into two categories; slip effects and inertial effects. Slip effects are important for high Kn flow processes. For the purpose of the present research, the rarefied-gas flow regimes are categorized, based on Kn , into the four different regimes summarized in table 2-1.

Table 2-1: Rarefied-gas flow regimes characterized by specified Kn range.

Flow Regime	Knudsen number range
No-slip flow	$Kn < 0.01$
Slip flow	$0.01 < Kn < 0.1$
Transitional flow	$0.1 < Kn < 10$
Free molecular flow	$Kn > 10$

In the no-slip flow regime the continuum assumptions are valid and the NSE with zero velocity (no-slip) at the fluid-wall contact is applicable. In the slip flow regime, the continuum assumptions are still valid; however the fluid velocity at the solid wall is not zero. The NSE with corrected wall condition can be applied in this regime. The transitional regime is the zone where neither continuum nor diffusion effects are dominant. As Kn approaches to 10, the flow regime gets closer to free molecular diffusion. In the diffusion regime, the collision of the molecules with other molecules does not play an important role in flow dynamics and viscosity becomes meaningless. Regarding natural porous media in petroleum reservoirs, high Kn flow happens in tight gas reservoirs, such as shale gas

reservoirs, where the average pore width is so small that even moderate-pressure gas flows are associated with high Kn .

Inertial effects, attributed to high Re fluid flow in porous media, are sometimes confused with turbulence effects. However, these two effects are distinct types of phenomena happening at different ranges of Re . While the turbulence effect is attributed to very high Reynolds numbers ($Re > 2000$), the inertial effect exists in porous media in low ranges of Reynolds number ($Re \approx 1$), as a result of the complexity of the flow path inside the pore throats and the constant change of direction and cross section in the pores. These effects cause a hydrodynamic head loss which accounts for a considerable portion of the total head loss in flow through porous media processes.

In this chapter the literature on slip effects and laminar inertial effects are presented in the first two sections. In the present thesis, non-Darcy effects are studied predominantly in the context of pulse-decay permeability measurements. In the last section of this chapter, a brief review of unsteady state pulse-decay tests is provided.

2.1 Rarefied-Gas Flow and Slip Effects

For Kn above the no-slip regime, the continuum assumptions becomes invalid and the gas is treated as being “rarefied”. Rarefied gas flow has been studied extensively. The current literature in the field of rarefied gas flow in small channels can be classified into three general categories based on the scale of the fluid system. In these categories, rarefied gas dynamics is studied in nano-scale, meso-scale and macro-scale.

The first category is the works done by using molecular and kinetic theory based methods such as the molecular dynamics method (MDM) and Direct Simulation Monte Carlo (DSMC) in nano-scale (Oran *et al.* 1998). In the MDM method, the trace and interaction of individual molecules are tracked and calculated by means of Newton's laws of the motion (Jakobsen 2014). In the DSMC method, the molecule motion is tracked exactly but the interaction of molecules are modeled by probabilistic methods (Piekos & Breuer 1996; Yan & Farouk 2002). Nano-scale modeling of rarefied gas flow studies the dynamics of fluid flow with the largest amount of detail of all the methods. However, because of the high computational costs of these nano-scale methods, their application is limited to very small scale systems (Fan & Shen 2001; Cai *et al.* 2000).

The second category is the works done in the meso-scale. One of the most popular methods in this category is the Lattice Boltzmann method (LBM). The LBM is a method derived from the kinetic theory of gasses (Suga *et al.* 2010). However, unlike the MDM and DSMC methods, the LBM does not track the positions and velocities of individual molecules but considers only frequency distributions for velocities of molecules at specified locations. LBM brings the advantage of validity beyond the flow regimes for which the Navier-Stokes equations can be applied (Chikatamarla & Karlin 2006; Shan *et al.* 2006). LBM has been a popular method to study non-equilibrium flow problems such as rarefied gas flow with high Kn and it has been shown to be efficient and accurate when compared to experimental measurements (Tang *et al.* 2005a; Tang *et al.* 2005b; Tang *et al.* 2007; Zhang *et al.* 2015). Numerous researchers have utilized LBM to simulate high Kn flow and found a good match between simulation and experimental results. Nie *et al.* (2002) showed that LBM can capture the fundamental behavior of rarefied gas flow including the slip condition at the

wall and nonlinear pressure drop. Lim *et al.* (2002) showed that LBM predicted velocity matches very well with experimental results for Kn up to 0.1. Zhang *et al.* (2005) applied LBM to simulate high Kn flow and found that their method is in good agreement with experimental data in the literature. In the present research, LBM was utilized to simulate rarefied gas flow associated with high Kn . Another popular kinetic based method of rarefied gas flow modeling in meso-scale is direct solution of the linearized Boltzmann equation (Aristov 2001; Xu 2001; Ohwada & Kobayashi 2004). In this method the Boltzmann equation is directly solved analytically or numerically by assuming a Maxwellian-type equilibrium distribution function for particles. This method was not utilized in the current research because there is not enough proof in the literature for the validity of this method.

In macro-scale, two approaches are described in the literature. First there are the methods that use the Navier-Stokes equations (NSE) with a slip model at the wall (Hadjiconstantinou 2003). As mentioned before, the problem with these methods is that for high Kn flow processes, the continuity assumptions and the NSE equations are not valid. Second there are the methods that assume that adding up diffusion flow rate calculated by Fick's diffusion equation and Darcy flow rate calculated by Darcy's equation would be the proper model for all the flow processes in the high Kn regime (Zhang *et al.* 2015). The problem with these methods is that the assumptions made for the model cannot be analytically and fundamentally verified. Harley *et al.* (1995) ran rarefied gas flow tests in microchannels for $0.001 < Kn < 0.4$ and found that the NSE with slip conditions at the wall matched the experimental results in very low Kn range very well. Arkilic *et al.* (1997) applied dimensional analysis to the NSE and first order slip condition at the wall and

derived analytical solutions for rarefied gas flow in microchannels. They used an experimental set-up to measure mass flow rate in a single channel for Kn up to 0.15 and found reasonable agreements between the model prediction and experiments. Beskok & Karniadakis (1999) proposed a second order slip condition at the wall to be implemented with the NSE and developed a second order analytical solution for rarefied gas flow in circular pipes. They compared their results with experiments and found a good agreement in the slip and free molecular regime. They proposed that the assumption of parabolic velocity profile is valid in all ranges of Kn except the transitional flow. Fluid flow in the transitional zone cannot be treated as either continuous nor as free molecular flow (Ho & Tai 1998).

The main concern in the rarefied gas flow regime is the wall condition. A comparison of the DSMC results with solutions of NSE including the slip condition at the wall show some differences (Zheng *et al.* 2002; Xu & Li 2004; Szalmás *et al.* 2007), which brings up the necessity of using higher order accuracy than that provided by the Navier-Stokes equations.

In the field of gas flow in tight natural porous media, the Klinkenberg equation has been historically used to modify the rock permeability in the slip flow regime (Klinkenberg 1941). There have been attempts to extend the Klinkenberg correction and derive a higher order accurate wall velocity and more accurate permeability corrections (Ashrafi Moghadam & Chalaturnyk 2014). Fathi *et al.* (2012) also modified the Klinkenberg equation and proposed a more accurate model. Javadpour *et al.* (2007) studied gas production mechanisms in tight shales with low permeability of less than 150 nano-Darcy and found that the gas flow could be predicted by a diffusion model with reasonable

accuracy. In their diffusion model the viscous effects were neglected and the flow rate was directly related to concentration difference and a constant diffusivity. Their experiments were performed in a Kn range corresponding to the free molecular diffusion regime. In the diffusion regime, the molecules do not sense much resistance caused by collision with other molecules and therefore ignoring viscous forces is reasonable.

The aim of the current study was to investigate the limits of the Klinkenberg equation and its higher order expansions in determining the permeability of a simple structured porous medium.

2.2 Laminar Inertial Effects

Laminar inertial effects are expected to become important when the local Re (based on the pore width) is greater than unity. These effects are called “laminar” because they happen at Re that are low when compared to Re that characterize turbulence effects. The Forchheimer effect is another name attributed to the laminar inertial effects in porous media flow (Forchheimer 1901).

The quadratic relationship of pressure drop and velocity has been found by numerical simulation of incompressible flow through cylinder arrays (Coulaud *et al.* 1988) and through sphere packs (Hill *et al.* 2001). There have been some research works that proposed a cubic relationship for the velocity and pressure gradient (Mei & Auriault 1991; Balhoff & Wheeler 2009). However, the range of the applicability of the cubic relationship is not wide.

Ruth and Ma (Ruth & Ma 1992) proposed an alternative form of representing the inertial effects on the permeability as:

$$\frac{1}{k} = \frac{1}{k_{abs}} \left(1 + \frac{\beta k_{abs} \rho u}{\mu} \right) \quad (2.1)$$

where k is the permeability, k_{abs} is the absolute permeability (permeability when inertial effects are minimal), β is the Forchheimer coefficient, ρ is the density of the fluid, and μ is the dynamic viscosity. Equation 2.1 could be simplified by defining a scaled permeability k_s as:

$$k_s = \frac{k}{K_{abs}} = \frac{1}{1 + F\dot{m}} \quad (2.2)$$

where F is a positive constant. One of the characteristics of equation 2.2 that will be shown later in this thesis to be problematic is that the second derivative of k_s with \dot{m} is always positive. Historically, the Forchheimer coefficient has been measured experimentally for each type of fluid and porous medium by multi-rate flow tests and there is no generally accepted theory to predict its value. However, there are empirical correlations relating the Forchheimer coefficient to permeability, porosity, and tortuosity.

Considering a porous medium to be a bead pack, Ergun (1952) derived a correlation for the Forchheimer coefficient as:

$$\beta = ab^{-0.5}(10^{-8}k)^{-0.5}\phi^{-3/2} \quad (2.3)$$

where a and b are constants depending on the porous structure surface, k is the permeability and ϕ is the porosity. Macdonald *et al.* (1979) tested Ergun's correlation by

experimentation and defined ranges for a and b . There are also other correlations obtained for natural porous media. Table 2-2 presents the correlations in the literature.

All the equations presented in table 2-2 relate the Forchheimer coefficient to permeability k , porosity ϕ , and tortuosity τ . These correlations are not universal because they are obtained for different types of porous materials.

Flow experiments on regular shaped sphere packs have shown the applicable ranges of the Forchheimer equation (Seguin *et al.* 1998; Dybbs & Edwards 1984; Fand *et al.* 1987). These ranges differ for each type of packing. That means the Forchheimer equation is not applicable in all ranges of Re .

Table 2-2: Correlations relating the Forchheimer coefficient (β) to porous medium properties.

Empirical Correlation	Reference
$\beta = 1.82 \times 10^8 k^{-5/4} \phi^{-3/4}$	(Janicek & Katz 1995)
$\beta = 0.005 k^{-1/2} \phi^{-1/2}$	(Geertsma 1974)
$\beta = 2.94 \times 10^7 k^{-1} \phi^{-1} \tau$	(Liu <i>et al.</i> 1995)
$\beta = bk^{-a}, \quad a \& b \text{ constants}$	(Cooke 1973)
$\beta = 3.1 \times 10^4 k^{-1} \tau^3$	(Thauvin & Mohanty 1998)

Fourar *et al.* (2004) solved Navier-Stokes equations by a finite element scheme in 2D and 3D sphere packs and introduced distinct non-Darcy flow regimes. They investigated the validity of the Forchheimer equation and found that the Forchheimer equation is valid in

3D flow in the sphere packs that were considered. Lee and Yang (1997) simulated the flow process through a bank of cylinders by direct numerical solution of the Navier-Stokes equations. They found that below Re of unity, the Darcy effect is dominant, and when the Re exceeds unity, the inertial effects account for the major part of the pressure drop. Rojas and Koplik (1998) simulated the same process as Lee and Yang (1997) in 2D mode and found that Re of unity is the critical point where the Darcy flow changes to Forchheimer flow.

Newman and Yin (2013) utilized the LBM to investigate the possible link between the porosity and permeability of 2D artificial porous structure and the Forchheimer coefficient. They stated that the change in the flow path is the dominant factor on the flow characteristics. Koch and Ladd (1997) applied the LBM to simulate low Re flow in arrays of aligned cylinders and studied the pressure gradient and flow rate. They found that a quadratic relationship similar to the Forchheimer equation exists between the flow rate and the pressure gradient. They also found that the flow rate and the pressure gradient have a linear relationship at vanishing Re , quadratic at finite Re , and cubic in the transitional zone where Re is much greater than unity.

Thauvin and Mohanty (1998) developed numerical pore network models with different geometrical properties (porosity, tortuosity and permeability) and ran flow tests on the networks to study the inertial effects. They provided a relationship between the Forchheimer coefficient, permeability and porosity based on the network flow results. Wang *et al.* (1999) developed numerical network models for an anisotropic porous medium

and tested the non-Darcy effects. They verified that a tensorial form of the Forchheimer equation is valid for anisotropic porous media in a limited range of Re .

Advancement of technology has made it possible to image a micro porous medium. The full structure of the flow paths in a small sample of a porous body can be determined by CT scanning. Researchers have tried to simulate the flow process in the imaged porous structure using numerical methods. Muljadi *et al.* (2016) investigated the effect of porous medium heterogeneity on the onset of non-Darcy flow by utilizing such direct flow simulations. They found that the critical Re that determines the onset of non-Darcy flow could differ a few orders of magnitudes for different rocks. Chukwudozie *et al.* (2012) used the LBM to simulate high velocity flow in the imaged porous medium of a sandstone sample and to predict Forchheimer coefficient, permeability and tortuosity. Their results were in good agreement with the experimentation data of Arns *et al.* (2004). Sukop *et al.* (2013) implemented the LBM to simulate high velocity flow in high permeability vuggy limestone. They found disagreements between the LBM and experimental results and linked those disagreements with the incapability of the current standard laboratory instruments to conduct flow tests on high permeability rocks.

To summarize, the research works presented in the literature suggests that the critical point where the Forchheimer effect becomes dominant strongly depends on the porous structure and is a value in the order of unity. The flow regimes for inertial flows are divided into three sub-regimes based on the critical Reynolds number (Re_c) and the transitional Reynolds number (Re_t) as shown in table 2-3. Re_c is the Reynolds number associated to the

point where inertial effects begin to cause a noticeable decrease of apparent permeability. Re_t is the point where the flow regime changes to turbulent.

Table 2-3: Flow regimes classified by the critical and transitional Reynolds number.

<i>Sub-Regime</i>	<i>Reynolds range</i>
Creeping (Darcy)	$Re < Re_c$
Forchheimer	$Re_c < Re < Re_t$
Transitional to turbulence	$Re > Re_t$

It is obvious in the literature that the Forchheimer coefficient is not determined by a universal equation and is generally accepted to depend on the porosity, permeability and the tortuosity of the porous medium. Also, the literature contains conflicting evidence that the pressure gradient and velocity could have a quadratic (Wang *et al.* 1999), cubic (Mei & Auriault 1991; Balhoff & Wheeler 2009) or linear relationship (Darcy). Different relationships are proposed in the literature because the ranges of mass flow rate or Reynolds number were limited. One purpose of the current research was to investigate the relationship between the mass flow rate and apparent permeability reduction caused by inertial effects by studying fluid flow in various 3D porous structures in a wide range of mass flow rate.

2.3 The Pulse-Decay Method

The characterization and measurement of intrinsic properties of porous rock samples are performed by laboratory experimentation. The porous rock samples that are cut in cylindrical pieces are called “core samples”. The permeability of a core sample can be

measured by one of two methods: the steady-state and the unsteady-state. The steady-state method is performed by flowing a fluid with known density and viscosity through the core sample and determining the flow rate and pressure drop (Takeuchi *et al.* 2008). Before measuring the flow rate and pressure drop, enough time must be allowed so that the flow rate becomes fully developed and steady through the sample. For tight rocks such as shales, the time needed to reach the steady state condition might be several days. Furthermore, the slip effects in tight rocks need to be studied in a wide range of pressure, while in a single steady-state flow test only a narrow range of pressure can be studied.

The unsteady-state method is performed by connecting the core sample to a vessel pressurized with gas and allowing a known volume of the gas to discharge through the core sample. The gas flow through the sample is a transient process, because the pressure inside the vessel will fall as a result of discharging. The pressure change inside the vessel is recorded with time and a numerical simulator is then used to “history match” the pressure record by determining appropriate permeability and Klinkenberg and Forchheimer coefficients. New correlations can also be used in this history match. The unsteady state process takes less time compared to the steady state process but still might take a long time for tight rock samples. There are a number of unsteady-state test designs based on methods to control the pressures at the upstream and downstream ends of the core sample.

Basically there are four types of unsteady-state core flow test methods with four different set-ups. In the first set-up the core sample is connected to two chambers of known finite size (Brace *et al.* 1968). The process is controlled by the volume of the chambers. In the second set-up the volume of the downstream chamber is very small comparing to the

volume of the upstream chamber so that the assumption of constant upstream pressure is valid (Bourbie & Walls 1982). In the third method the downstream pressure is kept constant by using a very big chamber as compared to the upstream chamber or by connecting the downstream flow line to the atmosphere (Jones 1997). In the fourth set-up both upstream and downstream pressure are kept constant so that the process becomes steady after an initial transient period. The most well-known unsteady state core flow test is the “pulse-decay” method which uses a chamber of known volume upstream of the core sample and a known, constant pressure downstream of the sample.

Comparing the four unsteady-state methods mentioned above, none of them has a clear advantage over the others. The application of each of the above methods depends on the available laboratory instruments and also the availability of a numerical simulator to history match the experimental results.

In the present research an unsteady state pulse-decay set-up was designed and a series of porous samples were tested to study permeability and inertial effects. The designed set-up can be adjusted to perform any of the four unsteady-state methods. The constant volume at upstream and constant pressure at downstream was set so that the flow process could be approximated by the steady state Darcy equation.

CHAPTER 3: NUMERICAL METHOD AND EXPERIMENTAL SET-UP

In this chapter the Lattice Boltzmann Method and the kinetic theory behind it are briefly introduced in the first section. In the second section, the experimental set-up and procedure used to validate the theoretical results is explained. In the following text, vectors are indicated by an arrow above the letters and tensors are indicated by bold letters, \vec{c} is the velocity vector, \vec{v} is the momentum vector, \vec{x} is the spatial location and the subscripts I and J represent the I^{th} and J^{th} particles.

3.1 The Kinetic Theory and the Lattice Boltzmann Method

A fluid system can be studied at different levels corresponding to different length scales. The three well known scales are nano-scale, meso-scale and macro-scale. In this chapter the kinetic theory and the Boltzmann Equation, which operate at the nano-scale and the Lattice Boltzmann Method, which operates at the meso-scale, are explained.

3.1.1 The Kinetic Theory and the Boltzmann Equation

At the nano-scale, the motion and interaction of the molecules are modeled individually based on the basic laws of physics and kinetic theory. Kinetic theory provides the link between the individual molecular dynamics and thermodynamic properties of dilute gases (Jakobsen 2014). Kinetic theory is a sub-division of statistical mechanics dealing with non-equilibrium systems based on averaging theory (Ferziger & Kaper 1972). Considering an isolated fluid system with N particles in a 3D Cartesian space and a corresponding velocity

space, the system at a certain time can be represented by a point in the S-dimensional ($S=6N$) phase space:

$$S \equiv S(\vec{x}_I, \vec{c}_I), \quad I = 1, \dots, N$$

The canonical equations provide the time evolution of a system of particles in S-dimensional space (Struchtrup 2005).

$$\frac{\partial \vec{x}_I}{\partial t} = \frac{\partial H}{\partial \vec{p}_I} \tag{3.1}$$

$$\frac{\partial \vec{p}_I}{\partial t} = -\frac{\partial H}{\partial \vec{x}_I}$$

Here $H(\vec{x}, \vec{p})$ is the Hamiltonian defining the total energy of the system in the coordinates $(\vec{x}_1, \vec{x}_2, \dots, \vec{x}_N)$ corresponding to location co-ordinates and momenta co-ordinates $(\vec{p}_1, \vec{p}_2, \dots, \vec{p}_N)$. The subscript I represents the I^{th} particle. The simplest Hamiltonian describing the energy of a weakly interacting dilute gas is presented in classical kinetic theory as (Kardar 2007):

$$H(\vec{x}, \vec{p}) = \sum_{i=1}^N \left[\frac{\vec{p}_i \cdot \vec{p}_i}{2m} + U(\vec{x}_i) \right] + \frac{1}{2} \sum_{(i,j)=1}^N V_{(2)}(\vec{x}_i - \vec{x}_j) \tag{3.2}$$

where U provides the potential energy from the external force and $V_{(2)}$ provides the so called two-body interaction force function. In the above representation of the Hamiltonian, multi-body interaction effects are ignored.

The dynamic behavior of the fluid particles follow Newton's laws of motion (Bird 1994):

$$\vec{F}_I = m_I \vec{a}_I = m_I \frac{d\vec{x}_I^2}{dt^2} \quad (3.3)$$

where \vec{x}_I is the position of particle I , m_I is the mass of particle I , t is the time and \vec{F}_I is the net force acting on particle I . The net force consists of external body forces and molecular interaction forces. In principle, it is possible to use equation 3.3 with any given molecular interaction model to track all the fluid particles in a finite space. However, due to the huge number of molecules in large systems, the computational expenses limit the applicability of this method to nano-scale problems.

To study the thermodynamic properties of fluids, it is not necessary to use all the information in the phase space. Introducing particle probability distribution functions in the phase space can allow description of a fluid system. Applying the particle probability function coarsens the fluid description to the meso-scale. A one particle distribution function $f_1(\vec{x}, \vec{c}, t)$ defines the probability of a single particle happening to be at the location \vec{x} with velocity vector \vec{c} at time t .

Following the Liouville's theorem and the Bogoliubov-Born-Green-Kirkwood-Yvon hierarchy, and implementing the assumption of molecular chaos, Boltzmann derived the following closed form equation for the time evolution of the one-particle distribution function due to binary molecular interactions for dilute gases (Kardar 2007):

$$\begin{aligned}
& \left[\frac{\partial}{\partial t} + \frac{\vec{p}_1}{m} \cdot \frac{\partial}{\partial \vec{x}_1} - \frac{\partial U}{\partial \vec{x}_1} \cdot \frac{\partial}{\partial \vec{p}_1} \right] f_1 \\
& = - \int d^3 \vec{x}_j d^2 \vec{b} |\vec{p}_j - \vec{p}_1| [f_1(\vec{x}_1, \vec{p}_1, t) f_1(\vec{x}_1, \vec{p}_j, t) \\
& \quad - f_1(\vec{p}_1, \vec{p}'_1, t) f_1(\vec{x}_1, \vec{p}'_j, t)]
\end{aligned} \tag{3.4}$$

where \vec{p}_1 and \vec{p}_j are the momenta of two particles before a collision, \vec{p}'_1 and \vec{p}'_j are the post collision momenta, and \vec{b} is the impact parameter which is related to the size of particles and the relative direction of their velocity vectors.

Equation 3.4 is written in abstract form as (Kardar 2007):

$$\frac{\partial f}{\partial t} + \vec{c} \cdot \nabla_{\vec{x}} f + \vec{g} \cdot \nabla_{\vec{c}} f = C(f) \tag{3.5}$$

where f represents the one particle distribution function, \vec{g} is the acceleration from the external body force component and $C(f)$ is the “collision function” that accounts for interactions between particles. The collision function is used to represent the whole integral on the right side of equation 3.4. Equation 3.5 is derived based on the assumption that the potential energy depends only on the external body force so that:

$$\frac{\partial U}{\partial \vec{x}_1} = -m\vec{g} \tag{3.6}$$

Bhatnagar *et al.* (1954) presented a model, generally referred to as the “BGK approximation”, to simplify the collision function resulting in the equation:

$$\frac{\partial f}{\partial t} + \vec{c} \cdot \nabla_{\vec{x}} f + \vec{g} \cdot \nabla_{\vec{c}} f = -\frac{1}{\tau} (f - f^{eq}) \quad (3.7)$$

where f^{eq} is the local equilibrium state of the particles and τ is a relaxation time which determines the rate of transformation of the local distribution towards the equilibrium distribution. Assuming unity molecular mass for a particle, the probability distribution function f provides the mass density distribution of the fluid particles in velocity and location spaces. The ultimate goal of kinetic theory is to find this distribution, because the most important thermodynamic and hydrodynamic properties (*i.e.* the fluid density $\rho(\vec{x}, t)$, the momentum density $\vec{u}(\vec{x}, t)$, the internal energy density $e(\vec{x}, t)$ and the stress tensor $\sigma(\vec{x}, t)$) can be calculated once f is known. The first four moments of the distribution function provide these entities.

$$\rho(\vec{x}, t) = \int f(\vec{x}, \vec{c}, t) d\vec{c} \quad (3.8)$$

$$\rho \vec{u}(\vec{x}, t) = \int \vec{c} f(\vec{x}, \vec{c}, t) d\vec{c} \quad (3.9)$$

$$\rho e(\vec{x}, t) = \frac{1}{2} \int (\vec{c}_0 \cdot \vec{c}_0) f(\vec{x}, \vec{c}, t) d\vec{c} \quad (3.10)$$

$$\sigma(\vec{x}, t) = - \int (\vec{c}_0 \otimes \vec{c}_0) f(\vec{x}, \vec{c}, t) d\vec{c} \quad (3.11)$$

where the ‘‘peculiar velocity’’ \vec{c}_0 , is defined as the particle velocity \vec{c} , with respect to the bulk velocity \vec{u} as:

$$\vec{c}_0 = \vec{c} - \vec{u} \quad (3.12)$$

The hydrostatic pressure P , is defined as the average of the diagonal components of the stress tensor $\boldsymbol{\sigma}$ (Shan *et al.* 2006):

$$P = \frac{\sigma_{ii}}{D} = \frac{2\rho e}{D} \quad (3.13)$$

where D is number of space dimensions. The Einstein summation convention is used in the above equation. The internal energy and the temperature T , are related as (Rao 2015):

$$e = \frac{D}{2}RT = \frac{D}{2m}k_B T \quad (3.14)$$

where R is the gas constant and k_B is the Boltzmann constant ($k_B=1.38064852 \times 10^{-23} \text{ m}^2\text{Kgs}^{-2}\text{K}^{-1}$). Combining Equations 3.13 and 3.14, the ideal gas law can be derived as:

$$p = \frac{\rho}{m}k_B T \quad (3.15)$$

$$p = \rho RT \quad (3.16)$$

3.1.2 The Lattice Boltzmann Method

In order to solve equation 3.7, $f(\vec{x}, \vec{c}, t)$ must be represented by a mathematical formulation. For the present application of the LBM, this is done by expanding the distribution function $f(\vec{x}, \vec{c}, t)$, on Hermite polynomial bases (Shan *et al.* 2006). Hermite polynomials are classic orthogonal sequences well suited to represent complex functions (see Appendix A for a description of Hermite polynomials). The notation for the distribution function will be:

$$f(\vec{x}, \vec{c}, t) = \omega(\vec{c}) \sum_{n=0}^{\infty} \frac{1}{n!} \mathbf{a}^{(n)}(\vec{x}, t) \mathbf{H}^n(\vec{c}) \quad (3.17)$$

where $\mathbf{H}^{(n)}$ is the rank- n Hermite polynomial, $\mathbf{a}^{(n)}$ is the corresponding expansion coefficient and $\omega(\vec{c})$ is a weight function. In the above equation \mathbf{H}^n and $\mathbf{a}^{(n)}$ are both rank- n tensors and the product on the right side of the equation denotes the full contraction of these tensors. Because of the orthogonal nature of the Hermite polynomials, the coefficients $\mathbf{a}^{(n)}$ can be calculated as:

$$\mathbf{a}^{(n)}(\vec{x}, t) = \int f(\vec{x}, \vec{c}, t) \mathbf{H}^n(\vec{c}) d\vec{c} \quad (3.18)$$

Expanding the distribution function using equation 3.17, the expansion coefficients can be obtained as a combination of the moments of the distribution function. The first four coefficients are:

$$\mathbf{a}^{(0)} = \int f d\vec{c} = \rho \quad (3.19)$$

$$\mathbf{a}^{(1)} = \int \vec{c} f d\vec{c} = \rho \vec{u} \quad (3.20)$$

$$\mathbf{a}^{(2)} = \int (\vec{c} \otimes \vec{c} - \delta) f d\vec{c} = \boldsymbol{\sigma} + \rho(\vec{u} \otimes \vec{u} - \delta) \quad (3.21)$$

$$\mathbf{a}^{(3)} = \int (\vec{c} \otimes \vec{c} \otimes \vec{c} - \vec{c} \delta) f d\vec{c} \quad (3.22)$$

$$= \mathbf{Q} + \vec{u} \mathbf{a}^{(2)} - (D - 1) \rho (\vec{u} \otimes \vec{u} \otimes \vec{u})$$

where δ is the Kronecker delta tensor and $\boldsymbol{\sigma}$ and \mathbf{Q} are given by

$$\boldsymbol{\sigma} = \mathbf{a}^{(2)} - \rho(\vec{u} \otimes \vec{u} - \boldsymbol{\delta}) \quad (3.23)$$

$$\mathbf{Q} = \mathbf{a}^{(3)} - \vec{u}\mathbf{a}^{(2)} + (D - 1)\rho(\vec{u} \otimes \vec{u} \otimes \vec{u}) \quad (3.24)$$

In the above notations $\vec{u}\mathbf{a}^{(2)}$ means the sum of all possible permutations of tensor product ($\vec{u}\mathbf{a}^{(2)} \equiv u_i a_{jk}^{(2)} + u_j a_{ik}^{(2)} + u_k a_{ij}^{(2)}$). The equilibrium distribution function in equation 3.7 can also be expanded in terms of Hermite polynomials bases:

$$f^{eq}(\vec{x}, \vec{c}, t) = \omega(\vec{c}) \sum_{n=0}^{\infty} \frac{1}{n!} \mathbf{a}_{eq}^{(n)}(\vec{x}, t) \mathbf{H}^n(\vec{c}) \quad (3.25)$$

In applying the LBM, f^{eq} is approximated by preserving only the first few expansion polynomials after truncating the above expansion.

$$f^{eq}(\vec{x}, \vec{c}, t) \approx \omega(\vec{c}) \sum_{n=0}^N \frac{1}{n!} \mathbf{a}_{eq}^{(n)}(\vec{x}, t) \mathbf{H}^n(\vec{c}) \quad (3.26)$$

The truncation of the expansion at any order has been shown to not affect the lower order moments (Shan *et al.* 2006).

Discretization of the velocity space in lattice units is performed by the Gauss-Hermite quadrature method. Based on the Gaussian quadrature, integral of a polynomial $\mathbf{p}(\vec{x})$ can be evaluated by the sum of the function value multiplied by some weights as:

$$\int_a^b \omega(\vec{x}) \mathbf{p}(\vec{x}) d\vec{x} \cong \sum_{i=1}^n \omega_i \mathbf{p}(\vec{x}_i) \quad (3.27)$$

Here $\omega(\vec{x})$ is an arbitrary weighting function and ω_i are a set of weighting constants to be calculated. The above numerical approximation is said to have an algebraic degree of precision m if it is an exact equivalency for any polynomial $p(\vec{x})$ up to the degree m . Equation 3.27 is used to discretize the velocity space and to calculate the weights by some mathematical manipulations which is out of the scope of this thesis (see Chen & Shan (2008) and Shan (2010) for more details). The location space is discretized by equidistant nodes which are also called voxels. For example, Figure 3-1 depicts a 2D space with nine discrete velocity directions at each space point.

The scheme used to denote different solution implementations is based on the number of space dimensions and the number of velocity directions. This velocity set in Figure 3-1 would be referred to as $D2Q9$ where $D\#$ is the number of space dimensions (two in this case) and $Q\#$ is the number of velocity directions (nine in this case). The $D2Q9$, $D2Q21$, $D2Q37$, $D3Q15$ velocity sets, associated weights and their algebraic precision are obtained by the integral quadrature method.

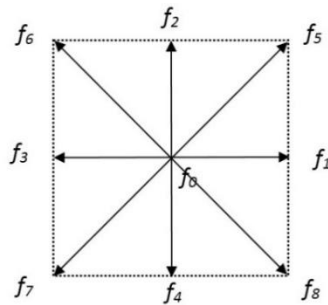


Figure 3-1: Schematic of $D2Q9$ velocity set.

The discretized form of equilibrium distribution function truncated at the 2^{nd} order Hermite polynomials reads:

$$f_i^{eq}(\vec{x}, t) = w_i \rho \left[1 + \frac{\vec{c}_i \cdot \vec{u}^{eq}}{c_s^2} + \frac{1}{2} \left(\frac{(\vec{c}_i \cdot \vec{u}^{eq})^2}{c_s^4} - \frac{\vec{u}^{eq} \cdot \vec{u}^{eq}}{c_s^2} \right) \right] \quad (3.28)$$

In the above equation, c_s has the same units as speed. It is used to non-dimensionalize the equilibrium distribution function and is called the “speed of sound in lattice space”. In the above equation \vec{u}^{eq} is the bulk velocity of the equilibrium state, ρ is the bulk density, \vec{c}_i ’s are the discretized velocities and w_i ’s are the “weights” associated with different lattice velocities. The bulk velocity and density are calculated as the moments of distribution function as:

$$\rho(\vec{x}, t) = \sum_i f_i(\vec{x}, t) \quad (3.29)$$

$$\rho \vec{u}(\vec{x}, t) = \sum_i \vec{c}_i f_i(\vec{x}, t) \quad (3.30)$$

and similarly \vec{u}^{eq} is calculated using

$$\rho \vec{u}^{eq}(x, t) = \sum_i \vec{c}_i f_i^{eq}(\vec{x}, t) \quad (3.31)$$

Schemes that are commonly used are *D1Q2*, *D1Q3*, *D2Q9*, *D3Q15* and *D3Q19*. The number of discrete points used in the quadrature technique determines the precision of numerical evaluation of the integral. In this study the following schemes were used: *D2Q9* and *D3Q15* (with precision of 5, that is, five terms in the quadrature technique) using a 2nd order Hermite polynomial expansion; *D2Q21* (with precision of 7) using a 3rd order Hermite polynomial expansion; and *D2Q37* (with precision of 9) using a 4th order Hermite polynomials expansion. Using the notation of Shan *et al.* (2006), the discretized velocity and weight sets of *D2Q9*, *D2Q21*, *D2Q37* and *D3Q15* are listed in tables 3-1, 3-2, 3-3 and

3-4. Here FS means “full symmetry set”. The full symmetry set of $(a,0)$, with a being a constant, is $(\pm a,0)$ and $(0,\pm a)$. The value given in the tables therefore applies to all the points $(a,0)$, $(-a,0)$, $(0,a)$ and $(0,-a)$. The values for c_s for $D2Q9$, $D2Q21$, $D2Q37$ and $D3Q15$ are $1/\sqrt{3}$, $\sqrt{2/3}$, 0.8354 and $1/\sqrt{3}$ respectively.

Table 3-1: Velocity and weight sets for $D2Q9$.

Speed Set	w_i
$(0,0)$	$4/9$
$(1,0)_{FS}$	$1/9$
$(\pm 1, \pm 1)$	$1/36$

Table 3-2: Velocity and weight sets for $D2Q21$.

Speed Set	w_i
$(0,0)$	$91/324$
$(1,0)_{FS}$	$1/12$
$(\pm 1, \pm 1)$	$2/27$
$(2,0)_{FS}$	$7/360$
$(\pm 2, \pm 2)$	$1/432$
$(3,0)_{FS}$	$1/1620$

Table 3-3: Velocity and weight sets for $D2Q37$.

Velocity Set	w_i
$(0,0)$	$0.23315066913235250228650$
$(1,0)_{FS}$	$0.10730609154221900241246$
$(\pm 1, \pm 1)$	$0.05766785988879488203006$
$(2,0)_{FS}$	$0.01420821615845075026469$
$(\pm 2, \pm 2)$	$0.00101193759267357547541$
$(\pm 2, \pm 1), (\pm 1, \pm 2)$	$0.00535304900051377523273$
$(\pm 3, \pm 1), (\pm 1, \pm 3)$	$0.00028341425299419821740$
$(3,0)_{FS}$	$0.00024530102775771734547$

Table 3-4: Velocity and weight sets for D3Q15.

<i>Speed Set</i>	w_i
$(0,0,0)$	$2/9$
$(\sqrt{3},0,0)_{FS}$	$1/9$
$(\mp\sqrt{3}, \mp\sqrt{3}, \mp\sqrt{3})$	$1/72$

In figure 3-1, each velocity vector in the D2Q9 model starts at a node and ends at a neighbor node. This is termed an “on-lattice velocity set”. If the velocity vectors start at a node and end at the space between some other nodes the set would be termed an “off-lattice velocity set”. All the velocity sets used in this study were on-lattice sets. Figure 3-2 shows the difference between on-lattice and off-lattice velocity vector.

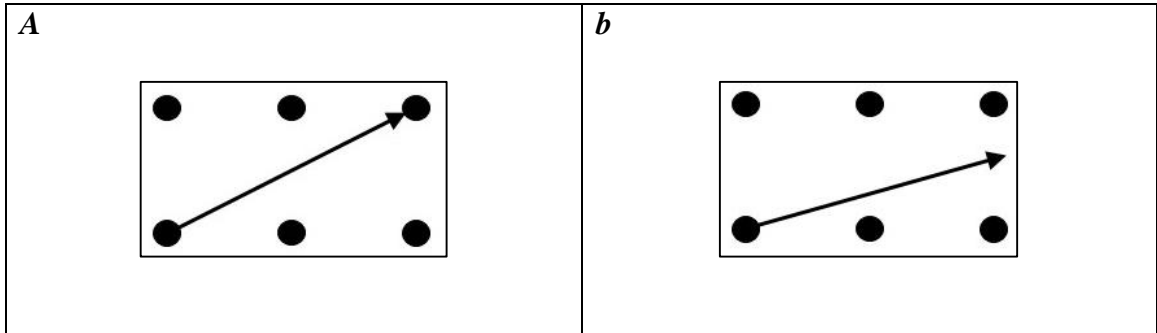


Figure 3-2: a) The on-lattice velocity component and b) the off-lattice velocity component. Here the black dots show the lattice nodes and the arrows show a discrete velocity vectors.

The solution to a thermodynamic process by the Lattice Boltzmann method is conducted by the algorithm shown by figure 3-3.

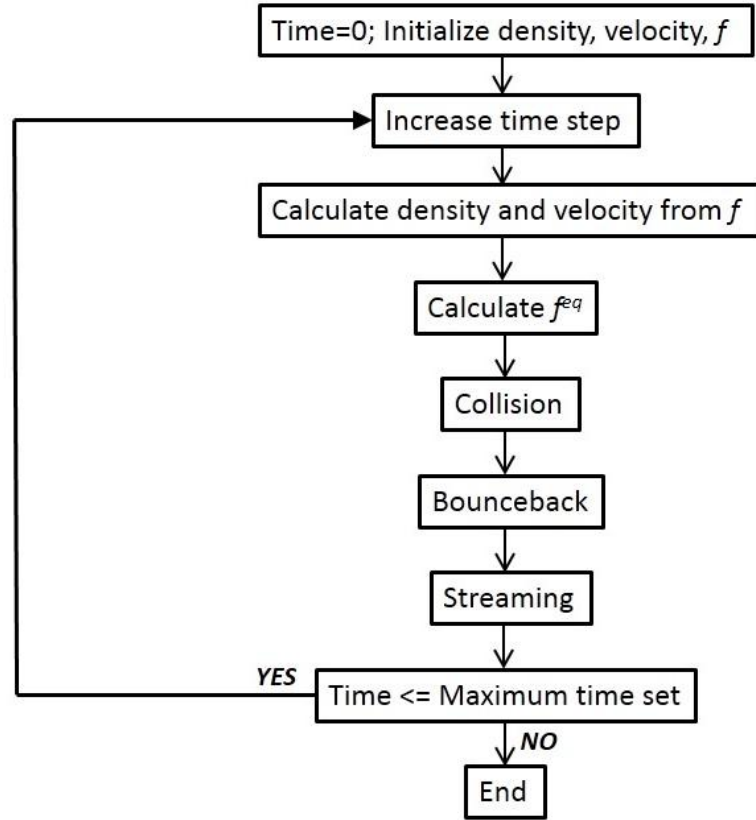


Figure 3-3: Flowchart showing the algorithm for applying the Lattice Boltzmann method.

This algorithm could be modified for various boundary and inlet-outlet conditions.

Figure 3-3 shows that Equation 3.7 is applied in two discrete steps; “collision” and “streaming”. In the collision step, a temporary value for the distribution function of the discretized velocities is calculated as:

$$\bar{f}_i(\vec{x}, t) = f_i(\vec{x}, t) - \frac{f_i(\vec{x}, t) - f_i^{eq}(\vec{x}, t)}{\tau} + \bar{F}_i \quad (3.32)$$

and in the streaming step, the temporary value is streamed in time and space as :

$$f_i(\vec{x} + \vec{c}_i \Delta t, t + \Delta t) = \bar{f}_i(\vec{x}, t) \quad (3.33)$$

One of the most important aspects of modeling flow in narrow channels is the treatment of the interaction between molecules and a wall. In this study two methods were used to model these interactions: “bounceback” and “specular reflection”. The bounceback scheme is illustrated in Figure 3-4.

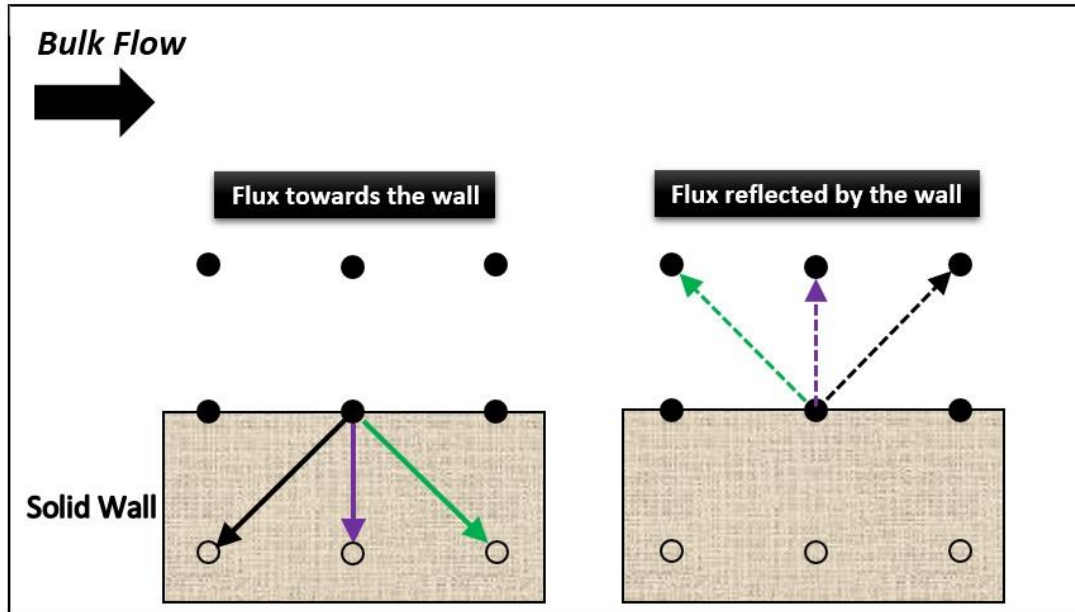


Figure 3-4: The bounceback boundary condition. The incoming flux from the lattice nodes (black filled circles) towards the wall are reflected in the opposite direction in one time step. The fictitious nodes in the solid wall (shown by circles) are placed just for clarification. Here the discrete velocities are color coded, the solid lines are the incoming flux and the dashed lines are the reflected flux.

In this scheme the wall reflects the streamwise velocity in the opposite direction to the incoming direction while reversing the normal velocity. By applying this scheme the incoming flux is reflected in the opposite direction so that the velocity at the wall would be zero for dense fluids. This would be a reasonable condition for the case of no-slip at the wall. An alternative scheme is the “half-way bounceback”, which is very similar to the

bounceback method. In the half-way bounceback scheme the wall is placed half way between two nodes. Figure 3-5 demonstrates the half-way bounceback scheme.

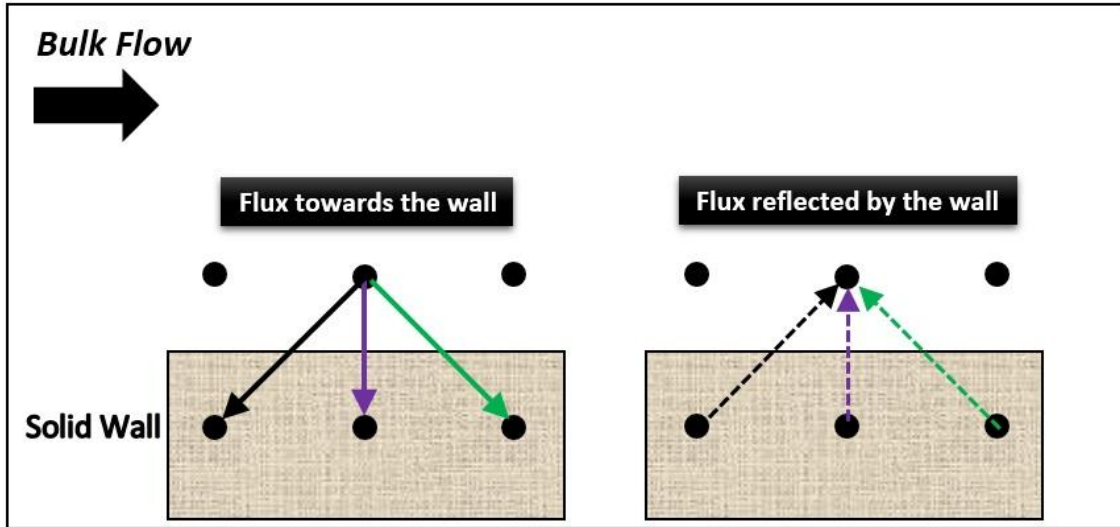


Figure 3-5: The half-way bounceback boundary condition. The incoming flux from the lattice nodes (black filled circles) towards the wall are reflected in the opposite direction in one time step. The fictitious nodes in the solid wall (shown by circles) are placed just for clarification. Here the discrete velocities are color coded, the solid lines are the incoming flux and the dashed lines are the reflected flux.

The specular reflection method is illustrated in Figure 3-6. In this scheme the wall reflects the incoming flux like a mirror and therefore conserves the streamwise velocity while it reverses the normal velocity.

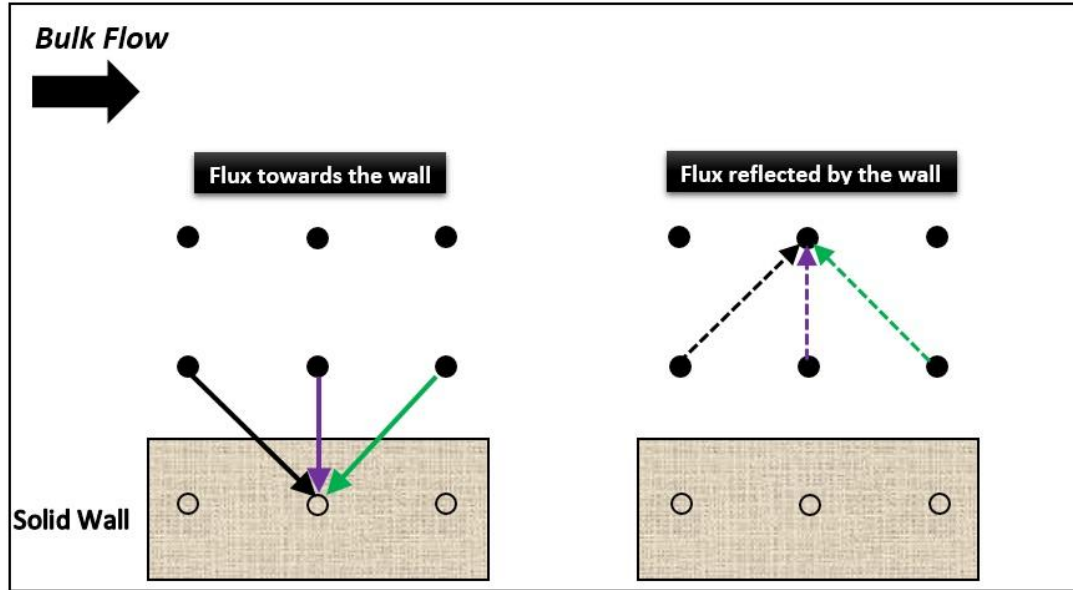


Figure 3-6: The specular boundary condition. The incoming flux from the lattice nodes (black circles) towards the wall are reflected like a mirror surface. The fictitious nodes in the solid wall are placed just for clarification. Here the discrete velocities are color coded, the solid lines are the incoming flux and the dashed lines are the reflected flux.

This would result in a fully-slip condition at the wall and would cause a plug flow type similar to what occurs in molecular diffusion. The collisions of the molecules with the wall in both cases are assumed to be fully elastic. The no-slip and fully-slip conditions happen at the lower and higher limits of Kn respectively.

The distribution function at the inlet and outlet of the model should be calculated based on the mass, momentum and energy conservation criteria. In this study velocity and pressure boundaries were imposed based on the He & Doolen (2002) method. To elaborate on this method, figure 3-7 shows a simple schematic of a 2D channel and the discrete velocity vectors at one of the inlet nodes and one of the outlet nodes. In this channel, an ideal gas enters as a constant velocity stream from the west (left) side of channel and exits from the

east (right) side into a constant pressure medium. In the model presented by figure 3-7, the discrete velocity vectors in the boundary nodes (inlet and outlet) that are pointed towards the outside of the channel and the ones pointed towards the walls are calculated at the streaming step while the rest of the velocity vectors are unknown.

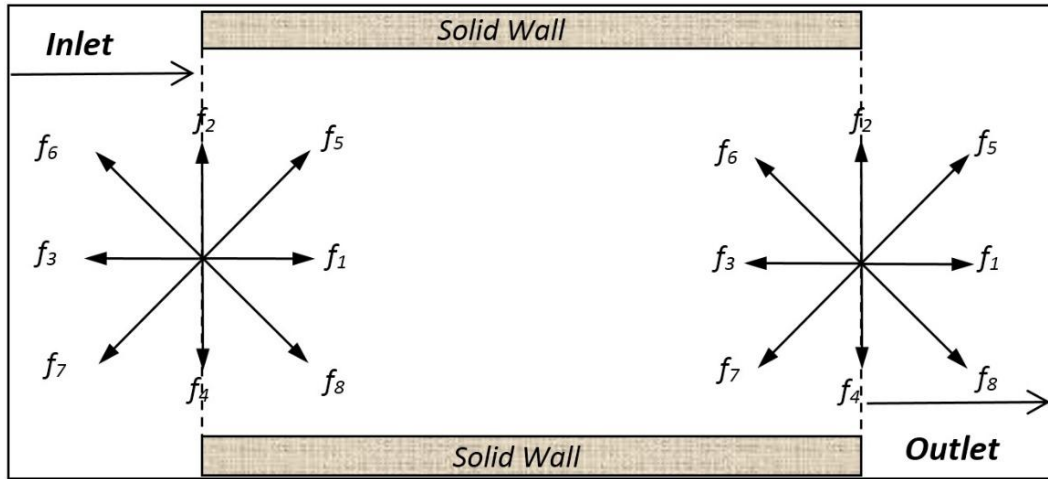


Figure 3-7: Schematic of the velocity set at the inlet and the outlet of the channel.

In the He and Doolen method the difference of the streamwise distribution functions is assumed to be the same as the difference of the streamwise equilibrium distribution functions and by using equations 3.29 and 3.30 all the components of the distribution function can then be calculated.

In figure 3-7, f_3 , f_6 and f_7 at the inlet and f_1 , f_5 and f_8 at the outlet are calculated during the streaming step, and f_1 , f_5 and f_8 at the inlet and f_3 , f_6 and f_7 are calculated by the He and Doolen method. Assuming known constant velocity at the inlet, the He and Doolen method utilizes the following equations:

$$\rho_W = \frac{1}{1 - u_W} [f_0 + f_2 + f_4 + 2(f_3 + f_6 + f_7)] \quad (3.34)$$

$$f_1 = f_3 + \frac{2}{3} \rho_W u_W \quad (3.35)$$

$$f_5 = f_7 - \frac{1}{2} (f_2 - f_4) + \frac{1}{6} \rho_W u_W + \frac{1}{2} \rho_W v_W \quad (3.36)$$

$$f_8 = f_6 + \frac{1}{2} (f_2 - f_4) + \frac{1}{6} \rho_W u_W - \frac{1}{2} \rho_W v_W \quad (3.37)$$

where the index W stands for the west (left) side, u_w is the velocity component parallel to the channel walls, v_w is the velocity component perpendicular to the channel walls and ρ_w is the density at the inlet. For the outlet, by the assumption of constant density (pressure), the unknown distribution function components are calculated using:

$$u_E = -1 + \frac{f_0 + f_2 + f_4 + 2(f_3 + f_6 + f_7)}{\rho_E} \quad (3.38)$$

$$f_3 = f_1 - \frac{2}{3} \rho_E u_E \quad (3.39)$$

$$f_7 = f_5 + \frac{1}{2} (f_2 - f_4) - \frac{1}{6} \rho_E u_E \quad (3.40)$$

$$f_6 = f_8 - \frac{1}{2} (f_2 - f_4) - \frac{1}{6} \rho_E u_E \quad (3.41)$$

where the index E stands for the east (right) side.

3.2 LBM Model Validation

In this study a 2D LBM simulator was developed to study rarefied gas flow in the high Kn range and 3D LBM simulators were developed to study inertial flow effects. In this section the procedures used to test the developed simulators against the analytical solutions are

described. As an additional validation method, the results for the 3D LBM simulator were compared with experimental results.

3.2.1 2D LBM Model Validation

In the first step towards studying rarefied gas flow in porous media, a second order LBM simulator was developed to model gas flow in a 2D thin, uniform, long channel at low Re .

A schematic of the channel is represented by figure 3-8.

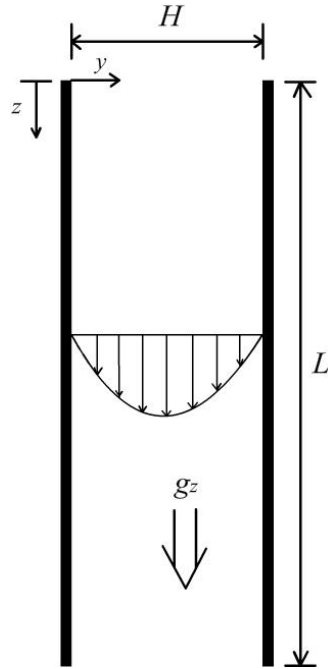


Figure 3-8: Schematic of the 2D channel. The parabolic curve and arrows are used to display the fully developed velocity profile.

Before trying to simulate the high Kn flow regimes, it is essential to validate the LBM simulator. In the developed simulator, a 2nd order Hermite polynomial expansion of the equilibrium distribution function was implemented with D2Q9 scheme. The case studied was the flow of an ideal gas in a long 2D channel at low Kn . The inlet condition was set to

constant velocity and the outlet condition was set to constant pressure. A mesh size of 41×1000 voxels was used to represent the channel. The velocity profile generated by the LBM model was compared with the analytical solution corresponding to the no-slip condition which may be written as (Arkilic *et al.* 1997):

$$u(y) = -\frac{H^2}{2\mu} \left(\frac{dP}{dz} + \rho g_z \right) \left(\frac{y}{H} - \frac{y^2}{H^2} \right) \quad (3.42)$$

Where $u(y)$ is the velocity at distance y from one of the walls, H is the channel width, μ is the dynamic viscosity, ρ is the fluid density, $\frac{dP}{dz}$ is the hydrostatic pressure gradient along the channel, and g_z is the body force acceleration along the channel all in SI units.

Conversion to LBM dimensions from any physical dimensions can be done using the characteristic length (L_0), time (T_0) and mass (M_0). Table 3-5 summarizes the needed dimension conversions.

Table 3-5: Physical and LBM dimension conversion relationships.

<i>Properties</i>	<i>Physical</i>	<i>LBM</i>	<i>Relationship</i>
<i>Distance</i>	Δx	$\Delta \hat{x}$	$L_0 = \frac{\Delta x}{\Delta \hat{x}}$
<i>time</i>	Δt	$\Delta \hat{t}$	$T_0 = \frac{\Delta t}{\Delta \hat{t}}$
<i>velocity</i>	u	\hat{u}	$L_0 T_0^{-1} = \frac{u}{\hat{u}}$
<i>density</i>	ρ	$\hat{\rho}$	$M_0 L_0^{-3} = \frac{\rho}{\hat{\rho}}$
<i>viscosity</i>	ν	$\hat{\nu}$	$L_0^2 T_0^{-1} = \frac{\nu}{\hat{\nu}}$

The relationship between the LBM viscosity and relaxation time is well accepted as (Mohamad 2011):

$$\vartheta = c_s^2(\tau - 0.5)\delta t \quad (3.43)$$

where δt is the lattice time step which is set to 1 for convenience.

The non-dimensionalized profiles generated by the LBM simulator and calculated by equation 3.42 are shown in figure 3-9. The case for this comparison is incompressible flow with $Kn \approx 0$ for the continuum equations, and the half-way bounceback wall condition is used in the LBM model.

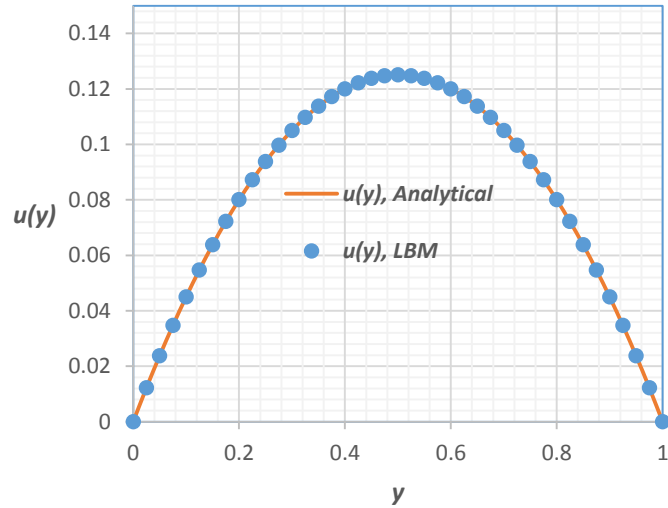


Figure 3-9: Velocity profiles obtained by LBM and analytical solution of NSE.

As it is observed in figure 3-9, there exists a very close match between the data predicted by the NSE and the LBM.

3.2.2 3D LBM Model Validation

A simulator code was developed that solves LBM governing equations in a 3D lattice space using the *D3Q15* scheme. The velocity set of the *D3Q15* model is given in table 3-4. The bounceback condition was applied at the contact of fluid and wall to assure a no-slip condition and zero velocity at the wall.

As the first test to verify the developed simulator, the simple process of body force driven flow in a 3D straight pipe was simulated and the steady state fully developed velocity profile was compared with the analytical solution of the Navier-Stokes equations. The analytical solution of the NSE for the body force driven flow of incompressible fluid in a long thin pipe at vanishing *Re* is (Arabjamaloei & Ruth 2016):

$$u(r) = \frac{g_z}{4\nu} (R^2 - r^2) \quad (3-44)$$

where $u(r)$ is the streamwise velocity component at a distance r from the center of the pipe ($r=0$ to R), R is the pipe radius, g_z is the streamwise body force acceleration and ν is the kinematic viscosity ,all in SI units.

The LBM model of the pipe utilized a $82 \times 82 \times 82$ voxels mesh and the body force driven flow in the channel was simulated by applying streamwise periodic boundary condition at the open faces and the bounceback condition at the wall. The streamwise periodic boundary condition causes the pipe to act like an infinitely long medium. The LBM and physical properties of the fluid and pipe are included in table 3-6.

Table 3-6: Physical and lattice properties used to test the developed LBM simulator.

<i>Properties</i>	<i>Physical value (SI units)</i>	<i>LBM value</i>
<i>pipe radius</i>	<i>0.1 (m)</i>	<i>40</i>
<i>body force acceleration (g)</i>	<i>1 (m/s²)</i>	<i>1.95e-11</i>
<i>fluid density</i>	<i>1 (kg/m³)</i>	<i>1</i>
<i>dynamic viscosity</i>	<i>0.25 (m²/s)</i>	<i>0.025</i>

The simulation was performed for a body force driven incompressible flow in the assumed circular tube. LBM is generally discretized in a Cartesian coordinate system. Modifications to the boundary conditions have been proposed to apply LBM to curved boundaries (Mei *et al.* 2000; Guo *et al.* 2002). To reduce the complexity of computation while preserving the original method, the circular tube was programmed with fine mesh size and the boundary was placed exactly on the selected nodes. Figure 3-10 compares the analytical and LBM predicted velocity for the fully developed velocity profile on the plane parallel to the pipe, cutting the pipe into two halves.

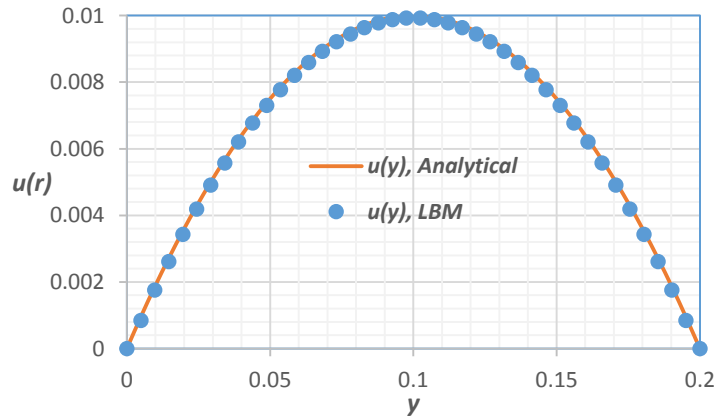


Figure 3-10: Streamwise velocity predicted by LBM and solution of NSE for the body force driven flow in circular pipe. Here $u(y)$ shows the velocity at distant y from one of the walls towards the center of the pipe.

It is seen in figure 3-10 that the LBM simulator output matches the analytical solution results very well.

As the second step, to test the capability of the LBM simulator to model fluid flow in non-regular porous structures, a simple structure of three connected pipes as shown in figure 3-11 was designed and built. The diameter of the small and large pipes was set to 0.276cm and 0.7493cm respectively and the lengths to 1.27cm and 2.0cm respectively.



Figure 3-11: Schematic of varying diameter circular pipe designed to test the LBM simulator.

The permeability of the structure in figure 3-11 could be estimated by the resistance method. The classical solution for laminar flow in a circular pipe combined with the Darcy equation reads:

$$q = -\frac{\pi R^4 \Delta P}{8\mu L} \approx -\frac{kA \Delta P}{\mu L} \quad (3.45)$$

where q is the volumetric flow rate, L and R are the total length of the pipe and radius respectively, ΔP is the pressure difference of inlet and outlet, k is permeability, A is area perpendicular to bulk flow, and μ is the viscosity, all in SI units.

The equality of the total pressure drop with the sum of the pressure difference of the three sections of the pipe will lead to an average permeability for the system as:

$$\Delta P = \sum_{i=1}^3 \Delta P_i \Rightarrow \frac{L}{K_{abs}A} = \sum_{i=1}^3 \frac{L_i}{k_i A_i} \quad (3.46)$$

where L_i 's, A_i 's and k_i 's represent the length, cross sectional area and absolute permeability of each section of the pipe respectively. For the designed porous sample the resistance method predicts a permeability of $5.69 \times 10^{-8} m^2$.

To test the permeability, the structure in figure 3-11 was built by drilling holes in two pieces of a polyvinyl chloride (PVC) rod and gluing the pieces together. To test the permeability of the designed structure a simple gravity drainage test was performed using the set-up shown by figure 3-12. This method is the classical falling head permeameter that Darcy used in the 1800s. The falling head permeameter was first used to test the permeability of soil and gravel for agriculture related purposes. Also this method is used in today's oil and gas industry for on-site permeability analysis of loose sands.

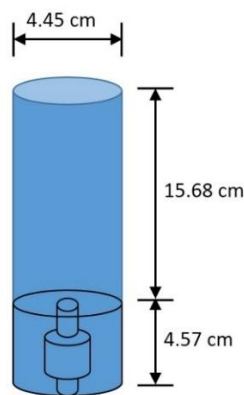


Figure 3-12: Gravity drainage test set-up designed to find the permeability of the sample.

The tank at the top of the sample in the cylinder was filled with water that was allowed to drain through the porous sample. By mathematical modeling (Appendix B), an equation can be derived to find the permeability of the sample as a function of drainage time as:

$$K_{abs} = -\frac{A_t \mu z \ln(V + 19.77 * 10^{-6})}{A \rho t \ln(294 * 10^{-6})} \quad (3.47)$$

where k is the permeability, A_t is the area of the cylinder containing initial water, A is the area of the wider hole in the porous sample, V is the volume of the drained water, μ is the dynamic viscosity of water, ρ is the density of water, z is the length of the porous sample and t is the draining time, all in SI units. The constants in equation 3.47 come from the geometry of the cylinder and sample. The drainage test was done 5 times and an average time of 55 seconds was recorded for the water on the top to drain through the hole, which results in a permeability of $5.52 \times 10^{-8} m^2$.

To test the LBM simulator, the body force driven flow in the geometry in figure 3-11 was simulated in a $200 \times 37 \times 37$ voxel mesh by applying a range of body force acceleration (g). Streamwise periodic boundary condition at the open faces and bounceback at the solid-fluid contact were applied in a D3Q15 scheme with viscosity of 0.015 in lattice units. Figure 3-13 represents the mass flow rate and permeability plot for the LBM results.

As it is seen in figure 3-13, the absolute permeability at very low mass flow rate predicted by LBM is $5.67 \times 10^{-8} m^2$ which is very close to the resistance method and experimental results. This shows that the body force driven flow simulated by LBM predicts the permeability of a non-regular geometry very well. These results also show the dependence

of the permeability on the mass flow rate, the phenomena that will be explored at length in Chapter 5 of the present thesis.

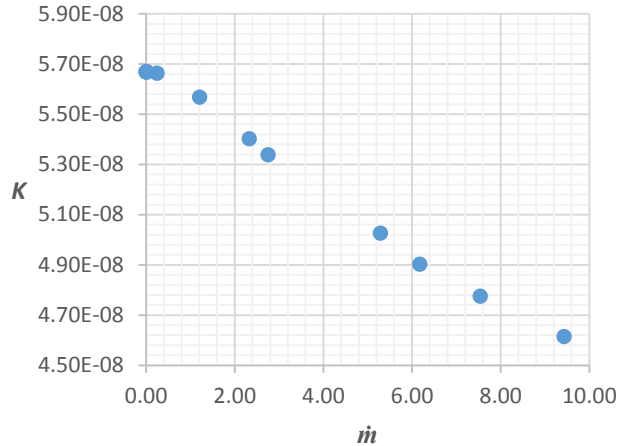


Figure 3-13: LBM predicted scaled permeability and mass flow rate in SI units.

3.3 Experiment Set-Up

An experimental apparatus was designed and built for the purpose of performing a modified unsteady-state flow test. For this application, chambers were connected to both sides of a core holder. Pressure transmitters were set near each side of the core holder. The core holder was pressurized to impose an overburden pressure of 120 *psi* for each test run. Connections were built in the system to enable evacuation of the two chambers and the pore space in the sample. Pressure readings were recorded by a data acquisition system (DAQ) at a maximum frequency of 250 readings per second. To check the temperature change, temperature transducers were installed in the connecting tubing of two chambers; however, no changes in temperature were observed in any of the experiments. The set-up designed for this study is represented by figure 3-14.



Figure 3-14: The modified pulse-decay experimentation apparatus.

For a better understanding of the experimental set-up, figure 3-15 represents the detailed diagram of the experimentation system with all the components.

The difference between the set-up in figure 3-14 and the common pulse-decay instruments is that in this set-up the upstream and downstream sections of the core holder could be either pressure controlled or volume controlled. To run the experiment, after the cylindrical rock is placed in the core holder, the gas flow test is performed in 5 steps.

1. The system is disconnected from the nitrogen supply, and all the lines including the sample are evacuated.
2. The upstream chamber is isolated from the pore volume by closing valve V1 and pressurized by nitrogen gas coming from the supply.
3. The DAQ records pressure and temperature at 4 spots starting when the ball valve V1 is opened.

4. When the pressures in the two chambers equalize, the experiment is stopped and V1 is closed.
5. CH1 is charged to a higher pressure and steps 3 and 4 are repeated.

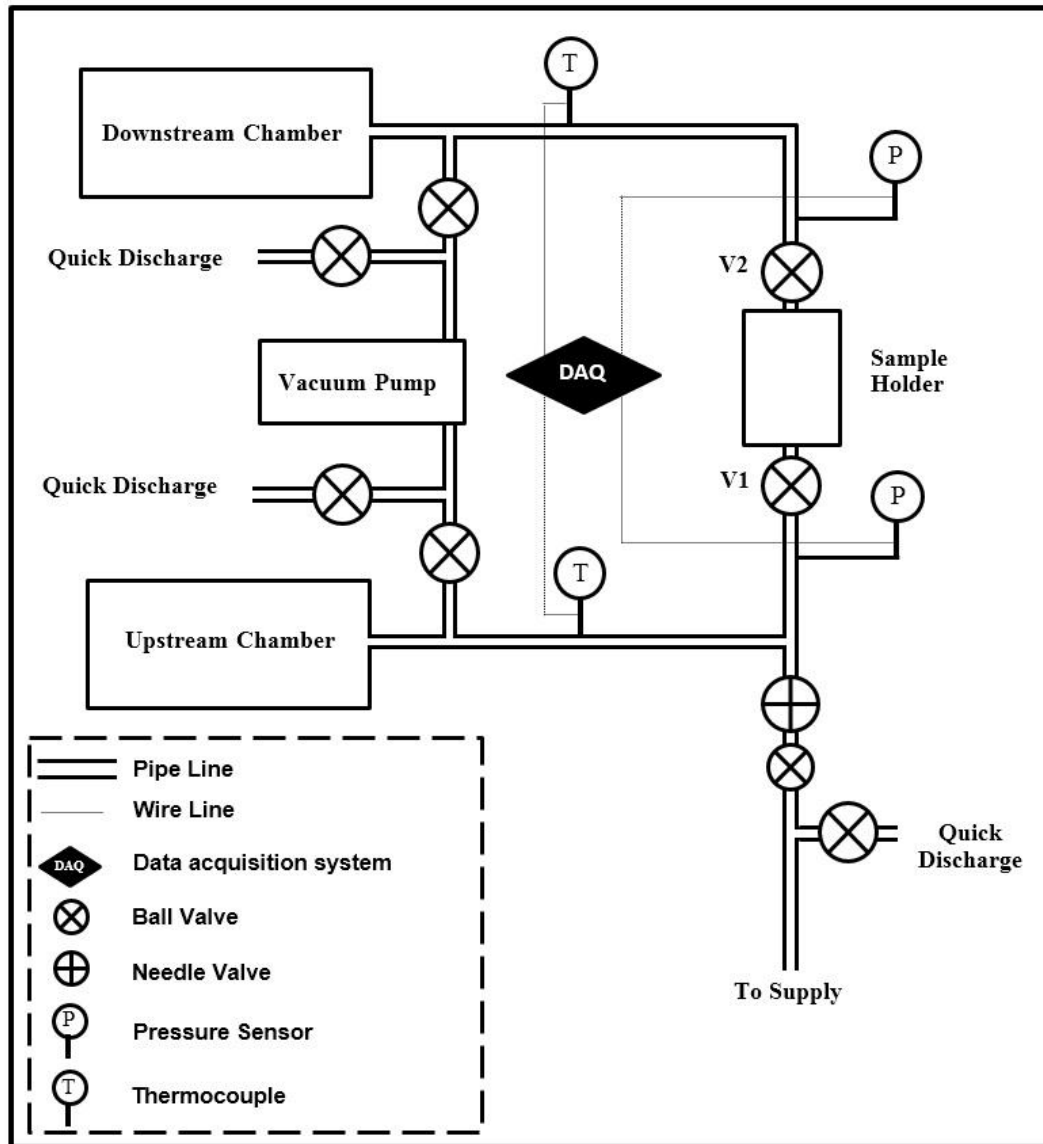


Figure 3-15: A schematic of the proposed set-up for the modified step-decay gas flow test.

For a complete pulse-decay test, the gas flow regime can fall in the diffusion, transitional, slip flow, Darcy and inertial dominant regions sequentially. In that case the test would be an unsteady state process and the results have to be analyzed by numerical history matching. An alternative way of performing permeability tests with the designed set-up is to set constant ambient pressure in the downstream chamber. This modification will shift the test more towards a steady-state process. For this purpose the downstream chamber is disconnected from the system and the gas is vented to the ambient through the quick discharge line.

Before running the experiments, the characteristics of the system including volume of different parts of the system must be measured and calibration of pressure and temperature transmitters must be performed. The calibration of pressure and temperature transmitter's readings which are in the range of 0-5 millivolts is performed by measuring the ambient conditions by manual barometers and thermometers with an error band of less than 0.025%. The calibration of the transducers was performed by the manufacturing company.

The volume of the chambers and the line sections from the upstream and downstream chambers up to the sample holder was measured by a simple expansion test. The two sides of the sample holder were isolated by replacing the sample with an impermeable rigid plastic rod and a confining pressure of 120 *psi* was applied. Two pressure generators with a 60 *ml* volume per stroke were used in the system as CH1 and CH2. The isolated parts of the line were evacuated and then pressurized with nitrogen gas. The initial volume of the pressure generator was zero. Gradually adding the pressure generator volume to the system, pressure was recorded at all stages. The ideal gas law was then used to calculate the initial

volume, which is the volume of the connecting line section from chambers to the face of the sample. Figure 3-16 shows the experimental readings and fitted ideal gas law equation.

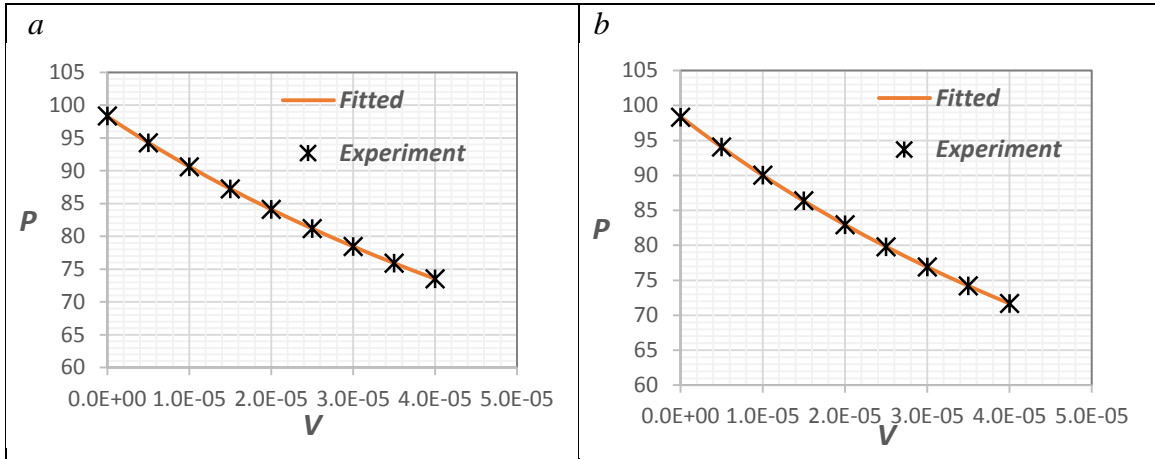


Figure 3-16: the upstream (a) and downstream (b) pressure change vs. the incremental volume (kPa vs. m^3).

As it is seen in figure 3-16, the ideal gas law matches the readings very well. The mean squared errors for both plots were in the scale of 10^{-5} . The volume of the flow line section from the upstream chamber (CH1) up to the valve V1 was measured using the same procedure. Figure 3-17 shows a sample of pressure measurements for a complete three-stage flow test.

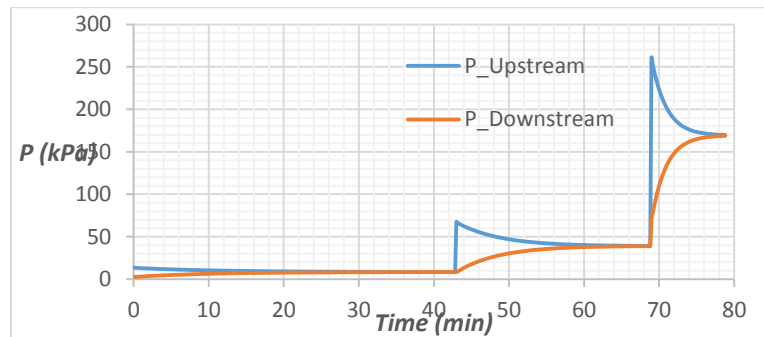


Figure 3-17: A sample of pressure recordings for a 3-stage flow test.

For this test the upstream was discharged through the sample 3 consecutive times. As it is seen in figure 3-17, after completion of each step the gas pressure in the downstream chamber was increased. The pressure recordings can be used for history matching using a numerical simulator and the characteristics of the porous rock sample can be calculated.

CHAPTER 4: SLIP EFFECTS AND THE KLINKENBERG MODEL

In this chapter the importance of applying models with higher accuracy for permeability modeling of rarefied gas flow in low permeability porous media is presented in the first section. In the second section the results of rarefied gas flow simulation in 2D channels is presented. Both the Klinkenberg model and higher order models are studied.

4.1 Theoretical Study

For a 2D channel with high aspect ratio (length divided by height) such as the channel shown in figure 4-1, when Re is low, the Navier-Stokes momentum equation can be simplified by ignoring the inertial terms and the following equation is obtained (Arkilic *et al.* 1997):

$$\frac{\partial^2 u}{\partial y^2} = \frac{1}{\mu} \left(\frac{dP}{dz} + \rho g_z \right) \quad (4.1)$$

where u is the streamwise velocity (the bulk velocity parallel to the driving force) component, y is the distance from the lower wall ($y=0$ to H), μ is the dynamic viscosity, g_z is the external body force acceleration along the channel direction and $\frac{dP}{dz}$ is the pressure gradient along the channel ($z=0$ to L).

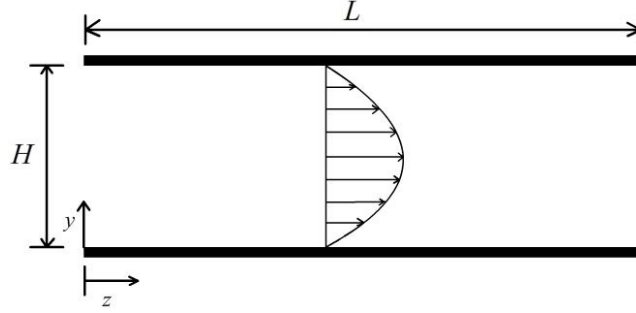


Figure 4-1: Schematic of the flow channel. The arrows and the parabolic curve represent the parabolic velocity profile.

If the confining walls are stationary, the common assumption is that there is zero velocity (“no-slip”) at the wall. In the present section, the case of rarefied gases will be considered. If kinetic theory considerations are included, the velocity boundary condition at the walls up to second order accuracy is (Hadjiconstantinou 2003):

$$u_w = \mp C_1 \lambda \left. \frac{\partial u}{\partial y} \right|_{wall} - C_2 \lambda^2 \left. \frac{\partial^2 u}{\partial y^2} \right|_{wall} \quad (4.2)$$

where λ is the mean free path of the fluid molecules, u_w is the fluid velocity at the wall and C_1 and C_2 are positive constants. It is stated in the literature that C_1 is the streamwise momentum accommodation at the wall as (Arkilic *et al.* 2001):

$$C_1 = \frac{2 - \sigma_m}{\sigma_m} \quad (4.3)$$

where σ_m is the tangential momentum accommodation σ_m Could have a value between zero and unity depending on the flow characteristics. Historically a value of 1 is used for C_1 in all engineering applications (Arkilic *et al.* 2001). Ohwada *et al.* (1989) obtained a value of 1.11 for C_1 by numerical solutions of the Boltzmann equation. The value of C_2

can be measured experimentally (Hadjiconstantinou 2003). Furthermore, as the fluid becomes denser, the mean free path goes to zero and the “zero velocity at the wall” condition is recovered. Integrating equation 4.1 in the y direction and applying the wall velocity boundary conditions (equation 4.2) results in:

$$u(y) = -\frac{H^2}{2\mu} \left(\frac{dP}{dz} + \rho g_z \right) \left(\frac{y}{H} - \frac{y^2}{H^2} + C_1 Kn + 2C_2 Kn^2 \right) \quad (4.4)$$

The average streamwise velocity at location z is then:

$$\bar{u} = \frac{1}{H} \int_0^H u dy = -\frac{H^2}{12\mu} \left(\frac{dP}{dz} + \rho g_z \right) (1 + 6C_1 Kn + 12C_2 Kn^2) \quad (4.5)$$

The Darcy equation for a one dimensional channel flow in a 2D channel reads:

Comparing equation 4.4 with the Darcy equation (equation 4.5) yields a Kn dependent permeability as:

$$K = K_{abs} (1 + 6C_1 Kn + 12C_2 Kn^2), \quad K_{abs} = \frac{H^2}{12} \quad (4.6)$$

where K_{abs} is the absolute permeability of the channel derived using the no-slip wall condition and low Re , which is recovered by letting Kn go to zero. The dimensionless Kn represents the ratio of the mean free path of the gas molecules to the width of the flow path.

$$Kn = \frac{\lambda}{W} = \frac{k_B T}{\sqrt{2} \pi d^2 P D} \quad (4.7)$$

where λ is the mean free path of the molecules, W is the width of the flow path, k_B is the Boltzmann constant, T is the absolute temperature, d is the effective diameter of the molecules and P is the static pressure. For a uniform channel the absolute permeability is related to the channel width ($K_{abs} = \frac{H^2}{12}$). Therefore, for a 2D channel, Kn is related to permeability and mean pressure as:

$$Kn = \frac{\lambda}{D} = \frac{k_B T}{\sqrt{2}\pi d^2 P \sqrt{12K_{abs}}} \quad (4.8)$$

Combining equations 4.6 and 4.8, the permeability can be written as a function of local pressure as:

$$\begin{aligned} K &= K_{abs} \left(1 + \frac{k_1}{P} + \frac{k_2}{P^2} \right), \quad k_1 = \frac{6C_1 k_B T}{\sqrt{2}\pi d^2 \sqrt{12K_{abs}}}, \quad k_2 \\ &= 12C_2 \left(\frac{k_B T}{\sqrt{2}\pi d^2 \sqrt{12K_{abs}}} \right)^2 \end{aligned} \quad (4.9)$$

where k_1 and k_2 are constants for a specific flow test, independent of pressure (P). If the first order wall velocity boundary conditions ($u_w = \mp C_1 \lambda \frac{\partial u}{\partial y} \Big|_{wall}$) is used instead of second order, the Klinkenberg equation will be recovered.

$$K = K_{abs} \left(1 + \frac{k_1}{P} \right), \quad k_1 = \frac{6C_1 k_B T}{\sqrt{2}\pi d^2 \sqrt{12K_{abs}}} \quad (4.10)$$

It is seen in equation 4.9 that the permeability is related to the local pressure and wall characteristics. Equation 4.9 was derived for a straight uniform channel and its extension to natural porous media needs special treatments for complex geometry and tortuosity.

Although the above derivation is mathematically consistent, applying the second order Kn related boundary condition to the NSE could be considered to be unreasonable because the NSE are inherently only accurate up to the first order Kn (Shan *et al.* 2006). This means that the NES are only applicable if Kn is less than approximately 0.1.

The hydrostatic pressure in underground gas reservoirs is relatively high, and this leads to small Kn that suggest that Kn related effects could be typically neglected. However if the mean pore radius, and therefore the absolute permeability, of the reservoir rocks is very small, such as is the case in shale gas reservoirs, that can lead to relatively high Kn .

To understand the variation of Kn in natural gas reservoirs and laboratory conditions, Kn was calculated for different pressures in the range of natural gas reservoirs and laboratory pressure for a typical average size of natural gas molecule diameters ($d=3.988 \text{ \AA}$) and a temperature of 300 K . Figure 4-2 shows the range of Kn for a few sample pressure values.

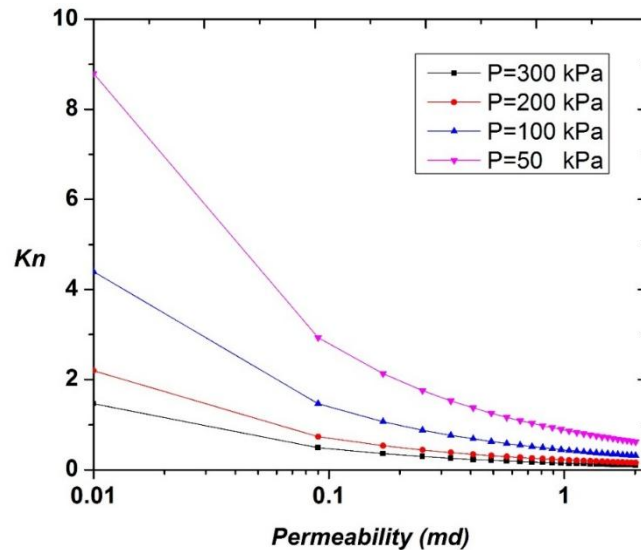


Figure 4-2: Kn range for low permeability and different mean hydrostatic pressure.

It is seen in figure 4-2 that Kn could reach to high values in the transitional zone ($0.1 < Kn < 10$) in low permeable reservoirs. This raises the necessity of applying a permeability correction method with an accuracy higher than the Klinkenberg model.

In this research a LBM simulator with 2nd order expansion of Hermite polynomials was used to simulate rarefied gas flow in 2D channels and estimate the constants in equation 4.6. In the present work the 2D Cartesian channel flow was studied for the sake of simplicity and in order to reduce the computational cost. Application of the LBM to 3D cases is straightforward but computationally expensive.

4.2 Numerical Study

A combination of half-way bounceback and specular reflection velocity can be used to set a limit for the slip behavior of the wall surface at any range of Kn . To check this idea, the developed 2D LBM simulator was used and five different ratios (0, 0.6, 0.9, 0.95 and 0.99) of the incoming flux towards the wall was set to reflect at the wall based on the specular reflection model and the remainder of the flux was set to bounce back in the opposite direction based on the half-way bounceback model. The ratios will be referred to as the “reflection coefficients (rf)”. The fully developed constant velocity entrance and constant density at the outlet was set based on the He & Doolen (2002) method. The velocity profiles at a distance $z=0.75 \times L$ from the entrance was studied for different reflection ratios. The channel flow was simulated by a 42×1000 voxels mesh. The study was done for four different dimensionless kinematic viscosity (ϑ) numbers corresponding to four different Kn and the results are shown by figures 4-3 to 4-6.

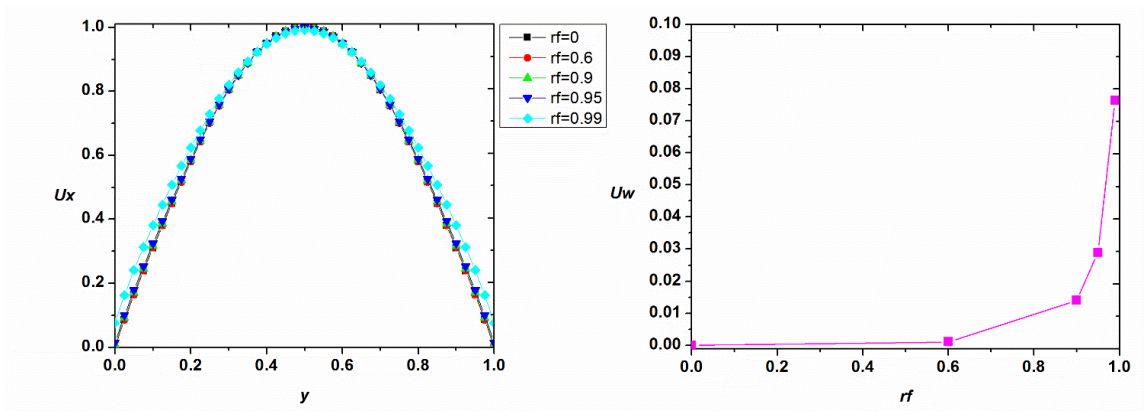


Figure 4-3: Velocity profiles and velocity at the wall for different rf and $\vartheta=0.0025$.

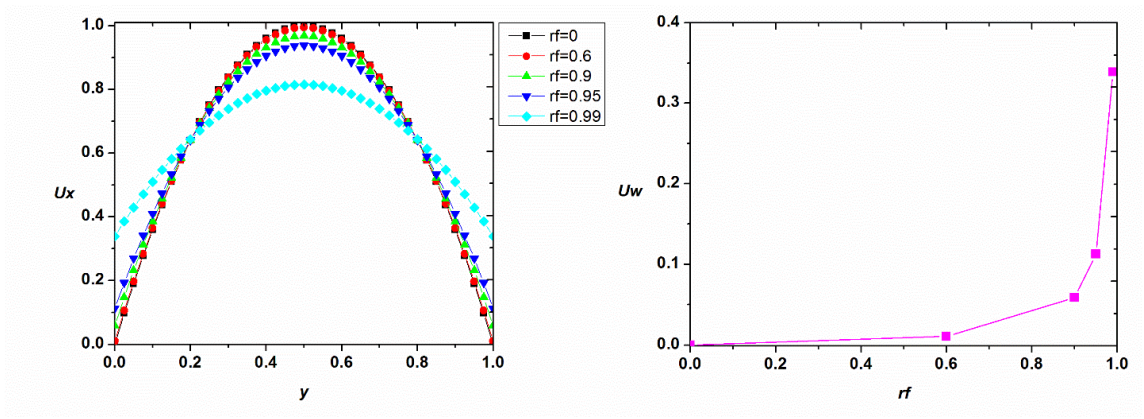


Figure 4-4: Velocity profiles and velocity at the wall for different rf and $\vartheta=0.025$.

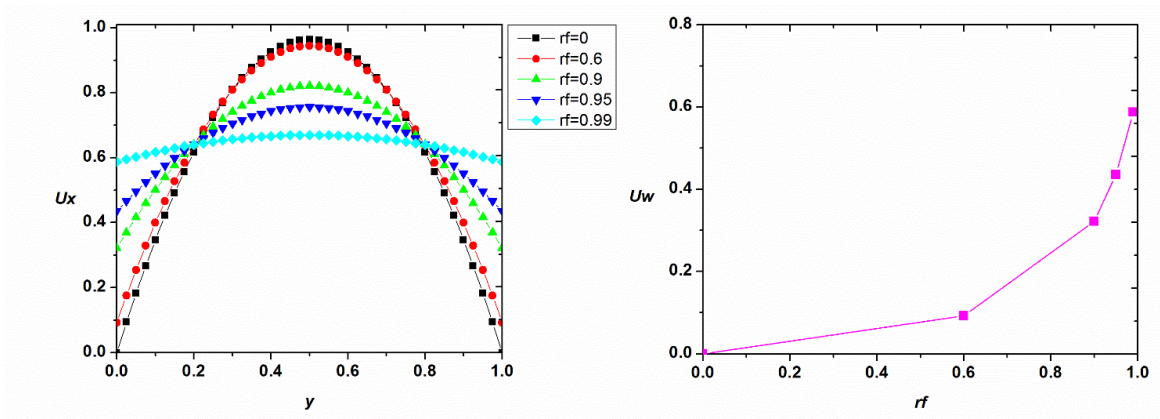


Figure 4-5: Velocity profiles and velocity at the wall for different rf and $\vartheta = 0.25$.

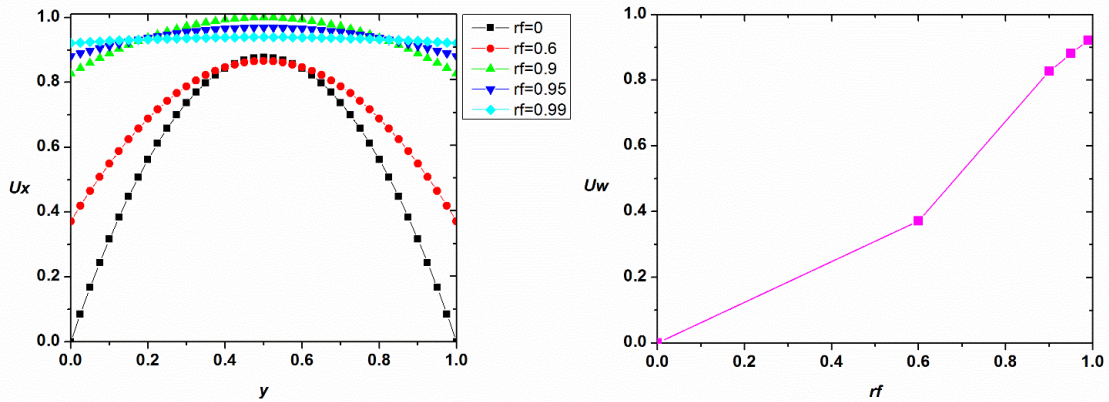


Figure 4-6: Velocity profiles and velocity at the wall for different rf and $\vartheta=2.5$.

It is seen in the above figures that the velocity profile shifts towards the plug flow type as the reflection coefficient increases. It is also observed that the reflection coefficient increment causes the wall velocity to increase more when the viscosity is higher. However, all the velocity profiles are actually parabolic curves with different velocities at the wall. This is similar to the behavior predicted in the slip flow regime by the Klinkenberg equation. All the velocity profiles could be scaled by parabolic profiles predicted by the NSE. However, an inconsistent behavior is observed in figure 4-6 (corresponding to the highest relative ϑ). In figure 4-6 the profiles shift upward for the higher reflection ratios, which is inconsistent with the figures for the lower relative viscosity. This raises a concern about the validity of implementing the second order Hermite polynomial expansion of the distribution function combined with specular condition at the wall. That is, these results suggest that a higher order accurate method should be tested for higher Kn flow regimes. Related to this concern, one of the key characteristics of rarefied gas flow in microchannels is the experimentally observed “Knudsen minimum”, that is, for the condition of constant driving force (pressure gradient or external body force), the flow rate in the channel

decreases with increasing specific Kn of the flow up to a minimum point and then starts to increase monotonically (Beskok & Karniadakis 1999; Kandlikar *et al.* 2016). Experimental data from the literature shows that this minimum happens around $Kn \approx 0.7$ (Dadzie & Brenner 2012). This key property of the process must be predicted by any proposed method of simulation of high Kn flow regimes for the method to be valid. The flow rate in a 2D wall bounded channel with constant external body force as the driving force and constant kinematic viscosity and relaxation time was calculated for a range of reflection coefficient with D2Q9 and kinematic viscosity of 2.5. The results are shown by figure 4-7.

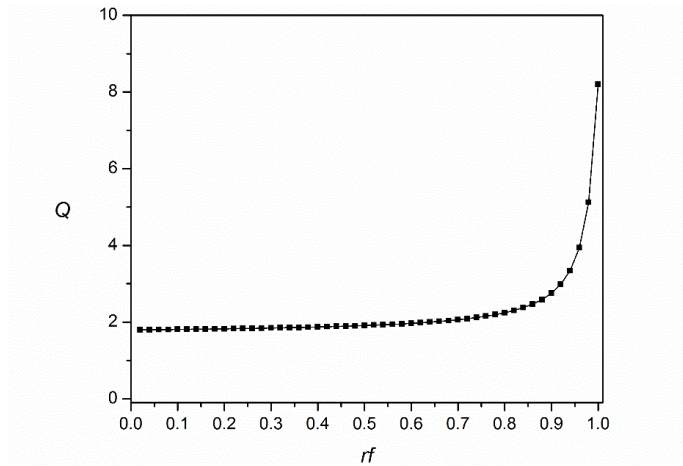


Figure 4-7: Non-dimensional flow rate (Q) for a wide range of reflection coefficient (rf).

Obviously, the Knudsen minimum is not observed in figure 4-7. Therefore, it can be concluded that including specular reflection in the D2Q9 model does not make the model capable of simulation of a wide range of Kn flow regimes.

4.2.1 Higher than Navier-Stokes Level Knudsen Accuracy

The gas flow regime in shale gas reservoirs are beyond the slip flow regime ($0.01 < Kn < 0.1$) and fall into higher Kn ranges (Zhang *et al.*, 2015). To capture the more accurate

behaviour of the gas flow in higher orders of Kn in the transitional regime, higher velocity moments must be implemented. By the analogy of Shan *et al.* (2006), which is based on the Chapman Enskog expansion, to include the effects of Kn^2 , fourth order Hermite polynomials should be involved and to go beyond that we need to add even higher moments. To investigate the transition flow regime, 3rd and 4th order hermite polynomials were included in the equilibrium distribution function expansion. As the polynomial rank increases, higher order accurate Gauss-Hermite quadrature is needed to discretize the velocity space. Higher order velocity sets are calculated by many researchers (Chen & Shan 2008; Kim *et al.* 2008; Chikatamarla & Karlin 2009; Shan 2010a). In this study the D2Q21 (with precision of 7) scheme along with the 3rd order Hermite polynomial expansion and the D2Q37 (with precision of 9) scheme with the 4th order herimite polynomials expansion were implemented.

The equilibrium distribution function truncated at the 4th order hermite polynomials expansion reads:

$$\begin{aligned}
f_i^{eq}(\vec{x}, t) = w_i \rho & \left[1 + \frac{\vec{c}_i \cdot \vec{u}^{eq}}{c_s^2} + \frac{1}{2} \left(\frac{(\vec{c}_i \cdot \vec{u}^{eq})^2}{c_s^4} - \frac{\vec{u}^{eq} \cdot \vec{u}^{eq}}{c_s^2} \right) \right. \\
& + \frac{c_i \cdot u^{eq}}{6c_s^2} \left(\frac{(c_i \cdot \vec{u}^{eq})^2}{c_s^4} - 3 \frac{\vec{u}^{eq} \cdot \vec{u}^{eq}}{c_s^2} \right) \\
& + \frac{1}{24} \left(\frac{(\vec{c}_i \cdot \vec{u}^{eq})^4}{c_s^8} - 6 \frac{(\vec{c}_i \cdot \vec{u}^{eq})^2 (\vec{u}^{eq} \cdot \vec{u}^{eq})}{c_s^6} \right. \\
& \left. \left. + 3 \frac{(\vec{u}^{eq} \cdot \vec{u}^{eq}) (\vec{u}^{eq} \cdot \vec{u}^{eq})}{c_s^4} \right) \right]
\end{aligned} \tag{4.11}$$

The discretized velocity and weight sets of D2Q21 and D2Q37 by the Shan *et al.* (2006) notation are listed in tables 3-2 and 3-3. The speed of sound (c_s) for D2Q21 and D2Q37 are 0.8165 and 0.8354 respectively.

Applying the higher order velocity sets (D2Q21 and D2Q37) is associated with complexities at the inlet, outlet and solid-fluid boundaries. In the inlet and outlet, the application of Dirichlet and Von-Neumann boundary conditions for higher order lattices is still not well understood; therefore in this research the body force was used instead of the pressure difference as the driving force for the gas flow. This was done to lessen the complexity of the model. The body force was inserted in the Boltzmann equation as an external body force and the periodic boundary condition was applied at the inlet and the outlet to reduce the complexity of the system. It has been shown that the external force can be inserted directly into the equilibrium distribution function by a correction to the equilibrium velocity as, $u^{eq}=u^{eq}+g\tau$, with g being the dimensionless body force acceleration (Zhang *et al.* 2006). In the solid-fluid contact wall, application of the half-way bounceback method at the wall is not understood yet. In the common half-way bounceback method the molecules with different velocities are accommodated on the wall and then released all at the same time. The time that the molecules are kept on the wall is termed “accommodation time”. The D2Q21 and D2Q37 lattices with 21 and 37 velocity sets include higher speeds (2 and 3 lattice nodes per unit time step). Applying the common half-way bounceback condition on these velocities at the wall results in different accommodation times based on the distance of the nodes from the wall. As a common routine, the half-way bounceback condition with varying accommodation time is applied at the wall boundaries, so that all the particles colliding at the wall would bounce back in

the opposite direction at the next time step. This is equivalent to having layers of fictitious nodes inside the wall. This is the most common method in coding the half-way bounceback wall condition. However, this method might not be reasonable because it implies the inelastic collision in an un-adjustable way. To provide a fully elastic half-way bounceback condition at the wall a new algorithm was used. In this algorithm the wall instantaneously bounces back all the incoming flux in the opposite direction with the same speed as the incoming flux. Therefore, the particles collide with the wall and bounce back without accommodating on the wall. Figure 4-8 shows how this process takes place.

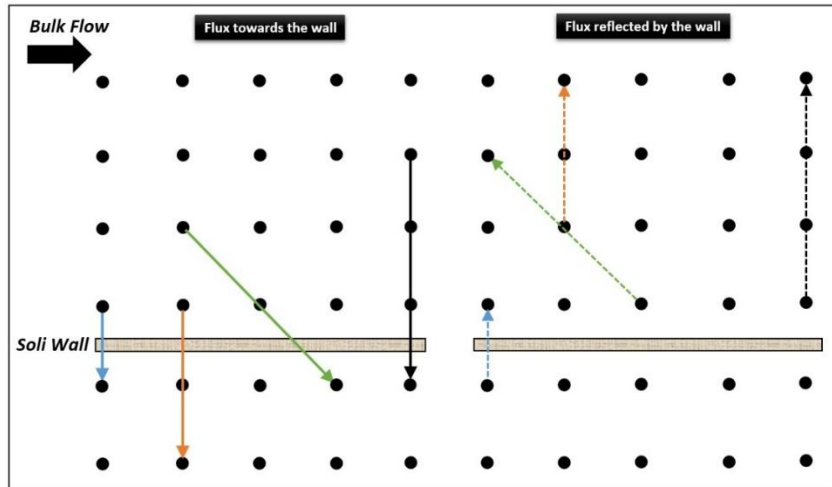


Figure 4-8: The half-way bounceback process in D2Q21. The velocity vectors are color coded. The solid arrows show the incoming flux towards the wall and the dashed arrows show the reflected flux.

The only imperfection of this algorithm is for the case of higher order velocity sets where the bounced-back particle would not sit on a lattice node and off-lattice interpolation methods must be applied. This happens in the D2Q37 model. In the present study the new algorithm was not implemented in the D2Q37 model.

The relationship between the Kn and the relaxation time (and consequently the LBM viscosity) is not considered unique by all researchers. Many different relationships have been implemented based on different reasoning. These relationships between the relaxation time, viscosity and Kn number (found by reviewing the literature) are listed in table 4-1.

Table 4-1: Different relationships between the relaxation time, viscosity and Kn .

Equation	Reference
$\tau = N_y Kn / \partial x$	(Lim <i>et al.</i> 2002)
$\tau = \frac{N_y Kn}{\partial x} + 0.5$	(Lee & Lin 2005)
$\tau = \frac{N_y Kn}{(\partial x \sqrt{\frac{8}{3}} \pi)} + 0.5$	(Tang <i>et al.</i> 2005a)
$Kn = \frac{\vartheta}{c_s N_y}$	(Zhang <i>et al.</i> 2005)
$Kn = \frac{2\tau c_s}{N_y}$	(Zhang <i>et al.</i> 2006)
$\tau = Kn$	(Meng <i>et al.</i> 2011)

In the above table, τ is the relaxation time, N_y is the number of nodes at the channel width, ∂x is the lattice spacing, c_s is the sound speed in lattice units, ϑ is the kinematic viscosity in lattice units, R is the gas constant and T is the temperature in lattice units. In all cases in table 4-1, there is a linear relationships between the relaxation time, viscosity and Kn .

The kinematic viscosity is defined as the ratio of the dynamic viscosity over the density as:

$$\vartheta = \frac{\mu}{\rho} \quad (4.12)$$

The kinematic viscosity of the gas is related to its thermodynamic properties. Empirical correlations has been developed to correlate these properties of natural gas (Chung *et al.* 1984; Chen & Ruth 1993; Sanaei *et al.* 2015). The mean free path is related to kinematic viscosity as:

$$\lambda = \vartheta \sqrt{\frac{\pi}{2RT}} \quad (4.13)$$

Therefore, by a simple analogy, Kn is related to viscosity in lattice units as:

$$Kn = \frac{\vartheta}{N_y c_s} \sqrt{\frac{\pi}{2}} \quad , c_s = \sqrt{\hat{R}\hat{T}} \quad (4.14)$$

Here \hat{R} and \hat{T} are gas constant and temperature in lattice units. Using three velocity sets D2Q9, D2Q21 and D2Q37 (with precision of order 5, 7 and 9 respectively), expanding the equilibrium distribution on Hermite bases of the orders of 2, 3 and 4, and applying external body force as the driving force, the streamwise velocity profiles in a 2D channel were calculated. Figures 4-9 to 4-11 show the results.

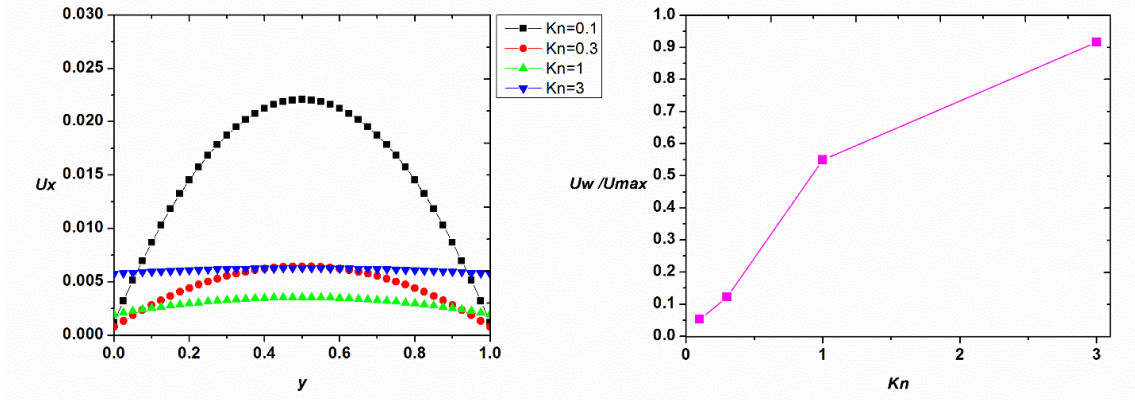


Figure 4-9: Velocity profiles and velocity ratio at the wall for different Knudsen numbers using D2Q9 model. Here U_w is the bulk velocity at the wall and U_{max} is the maximum bulk velocity which happens at the center of the channel.

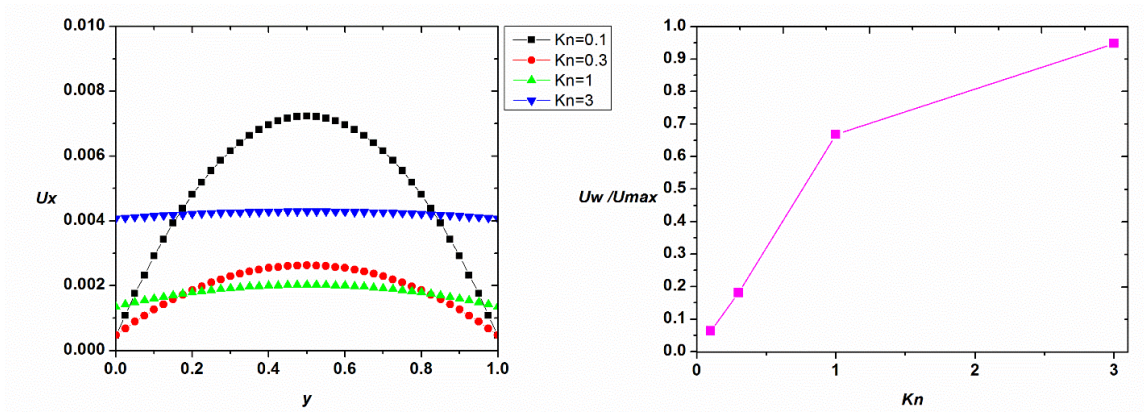


Figure 4-10: Velocity profiles and velocity ratio at the wall for different Knudsen numbers using D2Q21 model. Here U_w is the bulk velocity at the wall and U_{max} is the maximum bulk velocity which happens at the center of the channel.

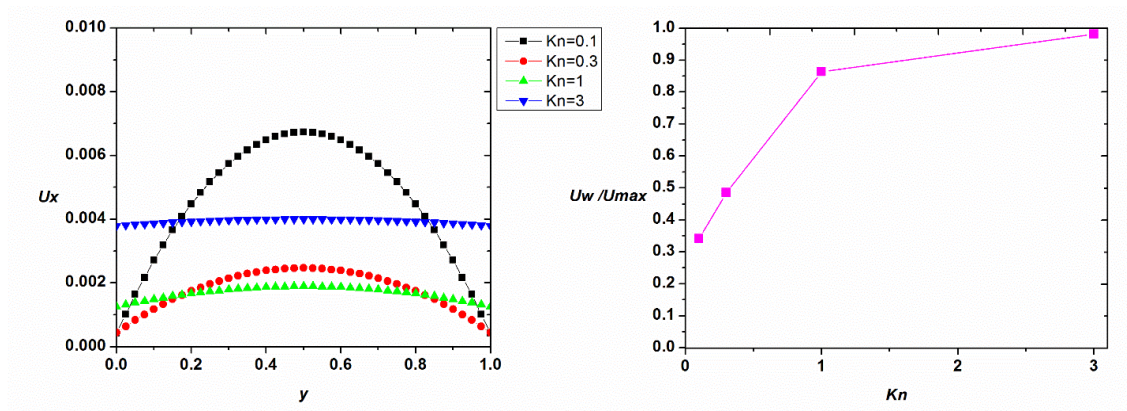


Figure 4-11: Velocity profiles and velocity ratio at the wall for different Knudsen numbers using D2Q37 model. Here U_w is the bulk velocity at the wall and U_{max} is the maximum bulk velocity which happens at the center of the channel.

As seen in figures 4-9 to 4-11, the higher Kn results in higher slip flow velocity at the wall. As Kn reaches 1, the velocity profile starts to look like plug flow. It is seen also that by including higher moments in the model, the slip velocity at the wall increases as Kn increases. To investigate if the LBM models satisfy the Knudsen's minimum characteristic, a set of simulations was performed with varying Kn . Results are shown in figure 4-12.

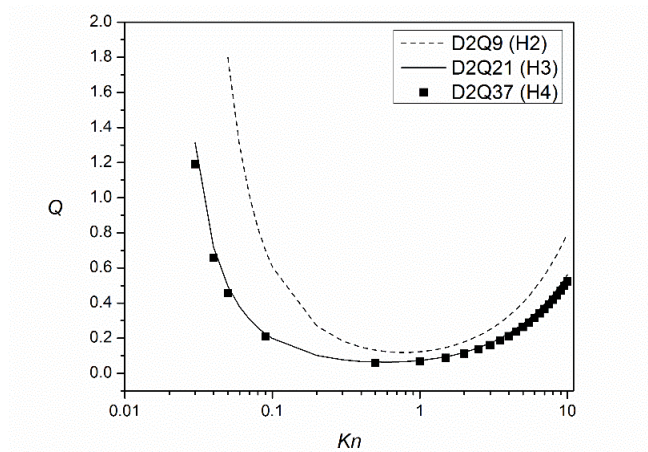


Figure 4-12: Prediction of mass flow rate (Q) with different orders of Hermite polynomials and velocity sets.

While third and fourth order models show very close results, the second order model dramatically over predicts the flow rate. However, all the three curves fall to their minimum value at $Kn \approx 0.7$ which agrees with experimental observations.

Another observation from figure 4-12 is that the D2Q9 model over-estimates the flow rate for Kn in the range of 0 to 10. As shown by figure 4-7, adding a specular reflection coefficient to the D2Q9 model causes an increase in the predicted flow rate. Therefore, it is obvious that adding specular reflection combined with the half-way bounceback method to the low order model actually leads to greater disagreement at the high Kn flow regimes.

Considering a natural porous medium as a bundle of parallel tubes (or channels in 2D space) with constant diameter, the results of figure 4-12 could be used to find the Knudsen related permeability. The permeability was calculated by the Darcy law using the results from figure 4-12. Figure 4-13 represents the scaled permeability versus Kn for the three different LBM models.

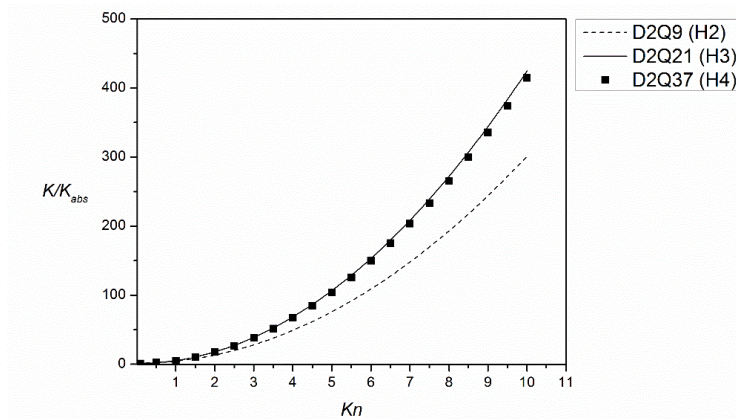


Figure 4-13: Prediction of the ratio of apparent permeability (K) and absolute permeability (K_{abs}) with different orders of Hermite polynomials and velocity sets. H2 in the legend shows the 2nd order expansion on Hermite polynomials.

As seen in figure 4-13, the permeability of the channel increases by increasing Kn . While the D2Q9 model predicts higher flow rate for a specific Kn , it shows lower permeability for the channel. That comes from the difference in viscosities for a specific Kn , as calculated by equation 4.14.

To compare these results with analytical models, equation 4.6 and some proposed C_1 and C_2 values reported in the literature were used. Tang *et al.* (2007) collected the reported values of C_1 and C_2 in the literature and performed an investigation on consistency of these proposed values with kinetic methods. These constants are given in table 4-2.

Table 4-2: Reported values in the literature for the constants in equation 4.6.

Source	C_1	C_2
Kennard (1938)	1.0	0
Schamberg (1947)	1.0	$5\pi/12$
Cercignani (1964)	1.1466	0.9756
Deissler (1964)	1.0	9/8
Sreekanth (1969)	1.1466	0.14
Hsia & Domoto (1983)	1.0	0.5
Mitsuya (1993)	1.0	2/9
Beskok & Karniadakis (1999)	1.0	-0.5
Hadjiconstantinou (2003)	1.11	0.31

The constant values from table 4-2 were used together with equation 4.6 to compute the ratio of the gas permeability to the absolute value of permeability for a 2D channel and the results are displayed by figure 4-14.

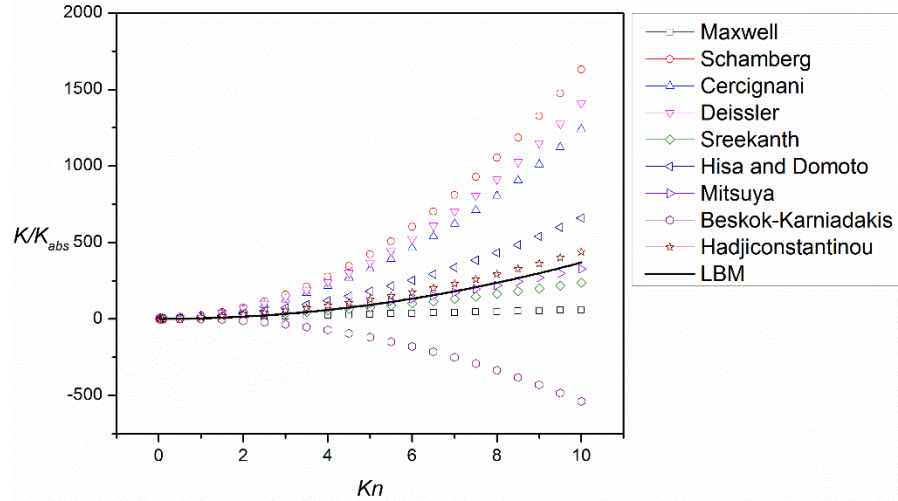


Figure 4-14: The ratio of the gas permeability (K) to the absolute value of permeability (K_{abs}) for a range of Kn

As it is seen in figure 4-14, most of the models over-predict the permeability. The constants presented by Mitsuya (1993) show the closest match with the LBM predicted permeability. It is also seen that the Beskok and Karniadakis' model leads to negative permeability for Kn values higher than 1.1. That arises from the negative value of the C_2 constant. Setting C_2 to a negative value is the same as setting the k_2 value in equation 4.9 to be negative. It is seen in some research works that negative values of k_2 were suggested for the corrected Klinkenberg model (e.g. Ashrafi Moghadam & Chalaturnyk (2014)). That obviously leads to false negative values of permeability for high Kn . The permeability ratio results presented by figure 4-14 were used to obtain C_1 and C_2 values by a curve fitting method and the best match was obtained by using -0.01585 and 0.3085 respectively. Figure 4-15 compares the results of LBM versus the developed correlation constants.

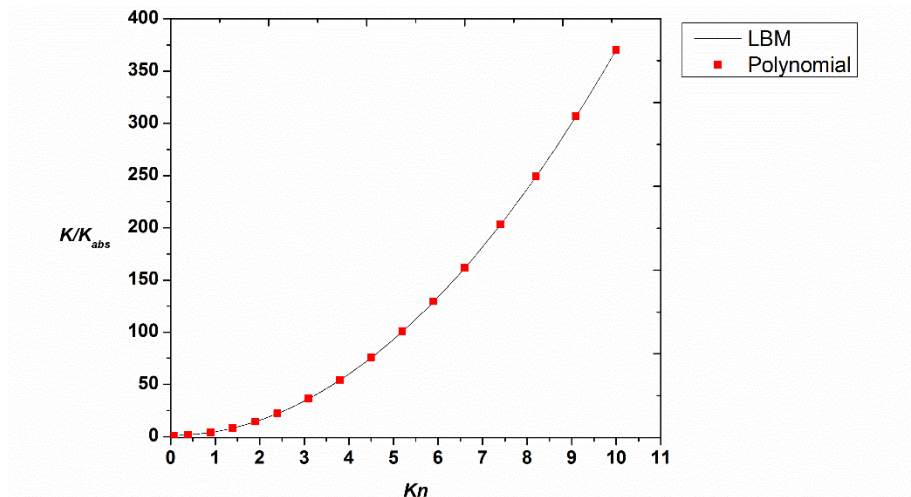


Figure 4-15: The permeability prediction by the LBM model and equation 4.6.

Because Kn in natural gas reservoirs mostly falls into the lower range of Kn , it is essential that the permeability correlation be accurate in that range. It was observed that for different ranges of Kn , different constants should be calculated or a higher order polynomial should be used. Table 4-3 summarizes the correlated C_1 and C_2 values for different ranges of Knudsen number.

Table 4-3: Correlated values of C_1 and C_2 for different ranges of Kn .

Set Number	Kn range	C_1	C_2
1 st Set	$0 < Kn < 0.1$	0.1375	-0.01613
2 nd Set	$0 < Kn < 1$	0.07797	0.274
3 rd Set	$0 < Kn < 10$	-0.01585	0.3085

Figure 4-16 shows the difference caused when the permeability ratio is calculated in the Knudsen range ($0 < Kn < 0.1$) using constants obtained for the three different ranges of Kn .

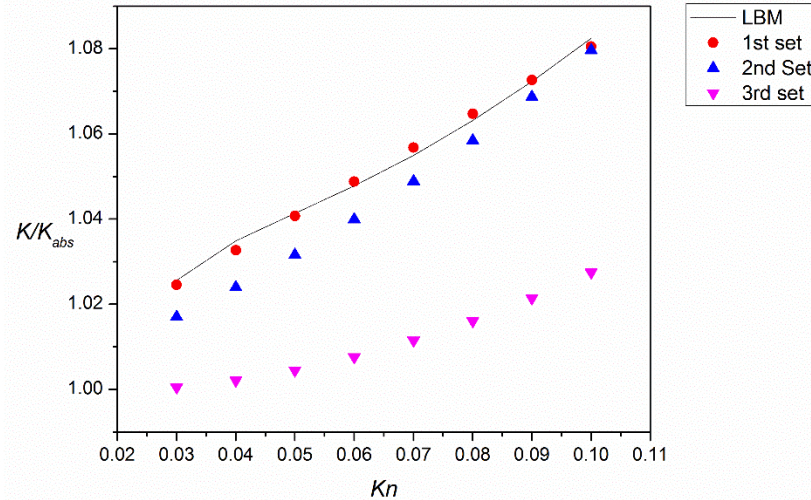


Figure 4-16: The permeability ratio prediction by LBM and equation 4.6 with three different sets of constants from table 4-3.

As seen in figure 4-16, the set of constants that results in the best prediction for Kn range of 0 to 10, leads to poor predictions for the lower range of Kn . That is because the relationship between the permeability ratio and Kn cannot be exactly predicted by a second order polynomial. New sets of constants were calculated for the three ranges of Kn . Table 4-4 shows the constants.

Table 4-4: Correlated values of C_1 and C_2 for different ranges of Kn .

Set Number	Kn range	C_1	C_2
<i>1st Set</i>	$0 < Kn < 0.1$	<i>0.1375</i>	<i>-0.01613</i>
<i>2nd Set</i>	$0.1 < Kn < 1$	<i>0.06797</i>	<i>0.2778</i>
<i>3rd Set</i>	$1 < Kn < 10$	<i>-0.0153</i>	<i>0.3076</i>

Using the constants of table 4-4, the Kn related permeability ratio was calculated and compared to the LBM results. Figure 4-17 illustrates the comparison.

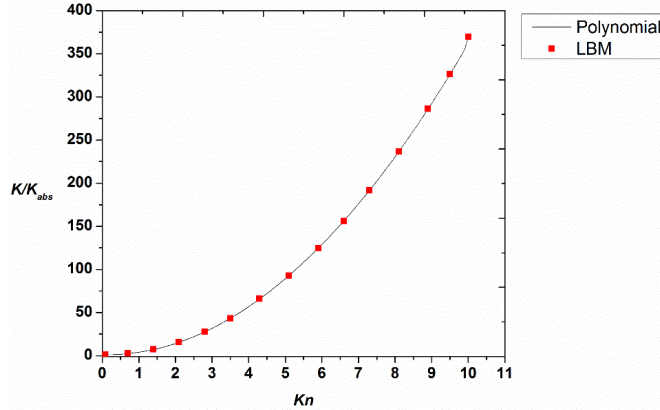


Figure 4-17: The permeability ratio prediction by LBM and equation 4.6 with different sets of constants for different Kn ranges from table 4-4.

The new sets of constants predict the permeability-Knudsen curve more accurately in all ranges of Kn . The values of constant in tables 4-3 and 4-4 are very small, specifically the value of C_1 is considerably smaller than the reported values in table 4-2 which are all close to unity. Using unity value for C_1 , the constant C_2 was found for the Knudsen range up to 10 based minimum mean squared error method. It was found that a value of 0.2444 for C_2 led to best fitting. Figure 4-18 shows the LBM results and the fitted curve.

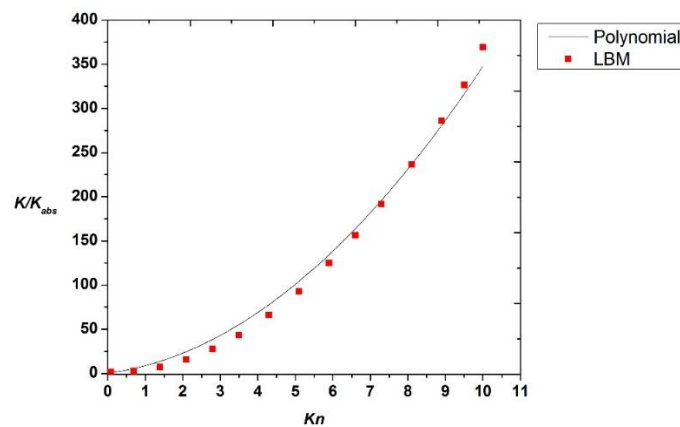


Figure 4-18: The permeability ratio prediction by LBM and equation 4.6 with C_1 set to 1 for Kn range of 0-10.

To check the importance of the constant C_1 , it was set to zero and the LBM results were fitted with equation 4.15.

$$K = K_{abs}(1 + 12C_2Kn^2) \quad (4.15)$$

It was found that a value of 0.3066 for C_2 leads to great match between the LBM results and equation 4.15. This value is very close to 0.31 that Hadjiconstantinou (2003) proposed.

Figure 4-19 represents the comparison of LBM results equation 4.15.

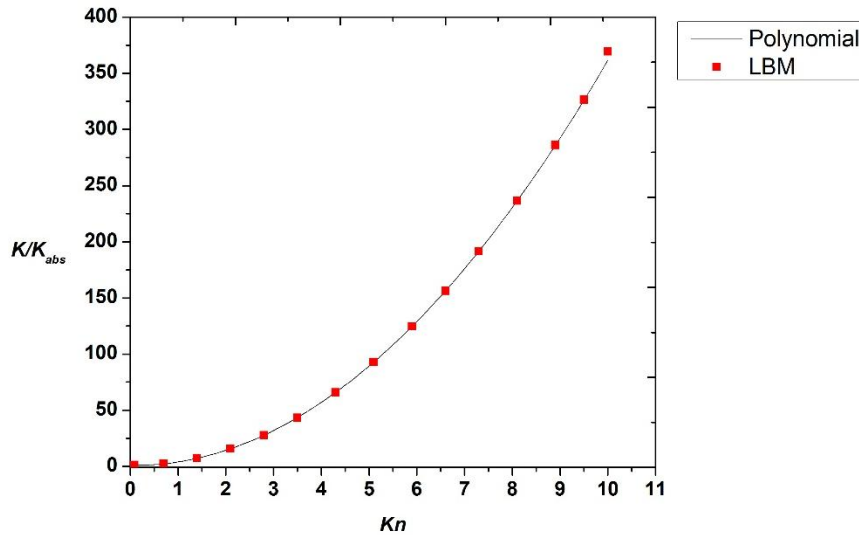


Figure 4-19: The permeability ratio prediction by LBM and equation 4.6 with C_1 set to zero for Kn range of 0-10.

The mean squared difference of the two sets compared in figure 4-19 was calculated to be 0.0194. The results of the comparison in figure 4-19 implies that the first order Knudsen term in equation 4-6 has relatively very low importance comparing the second order Knudsen term and it could be ignored. This finding is not reported in the literature and that makes it unique. This result could be interpreted based on the two terms of the boundary

condition (equation 4.2). The first term in equation 4.2 is a first order differential term similar to the viscous shear stress and the second term is the second order differential term that is placed in the diffusion equation. Zero C_I could be interpreted as; the importance of the viscous shear stress is way lower than the diffusion term in high Kn range and that's why a negligible C_I results in a good fit with LBM results.

CHAPTER 5: LAMINAR INERTIAL EFFECTS AND THE FORCHHEIMER MODEL

In this chapter an LBM study of laminar flow dominated by inertial effects is presented. The Forchheimer equation is tested to model the LBM results. A new correlation equation is proposed to replace the Forchheimer equation. Experimental flow test results, that provide a validation of the LBM, are also presented and discussed in the last section.

5.1 Numerical Study

As a preliminary test of the Forchheimer equation, the results shown in figure 3-13 were fitted to equation 2.2 and the constant F was found by a minimum mean squared error analysis. Figure 5-1 compares the LBM results and the Forchheimer prediction.

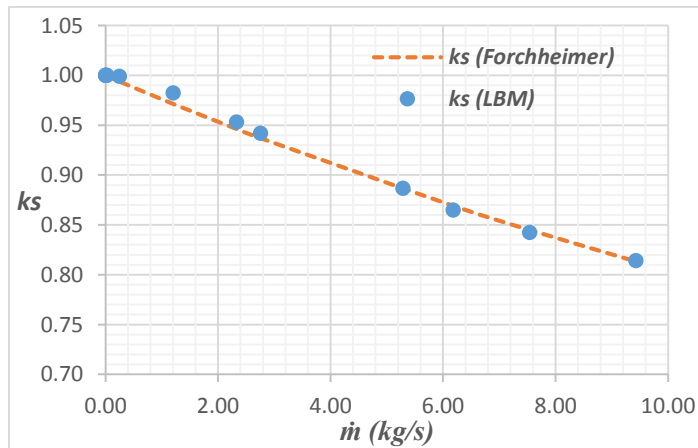


Figure 5-1: The LBM predicted scaled permeability (k_s) and mass flow rate relationship with the Forchheimer equation prediction.

The trend of k_s predicted by LBM in figure 5-1 shows a negative second derivative of scaled permeability with mass flow rate (k_s'') up to an inflection point and a positive k_s'' for

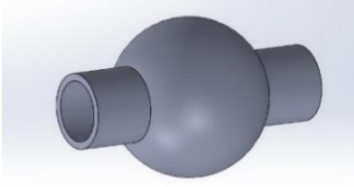
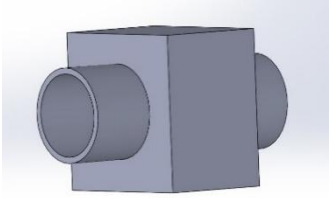
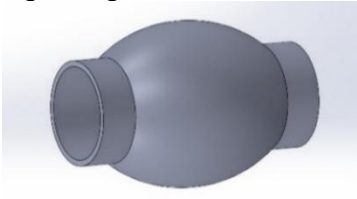
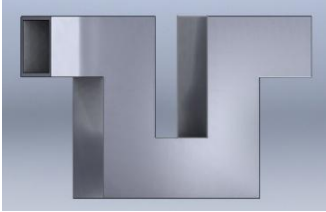
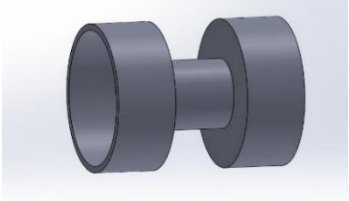
the rest of the graph. However, as discussed before, in the Forchheimer equation, the scaled permeability has always a positive k_s'' with mass flow rate. This results in a noticeable error in k_s predictions at low mass flow rates.

Laminar inertial effects are caused by sudden changes in the geometry of the flow path. These sudden changes cause a change in fluid velocity direction. As long as these changes in velocity direction do not lead to recirculation, they are not a significant source of inertial effects. For example a tortuous flow path would cause a change in flow direction but if it doesn't cause recirculation of the fluid, then it does not significantly affect the permeability.

The main geometry changes that cause recirculation of the fluid are expansion, contraction and bends. When the flow path is expanded suddenly, the fluid will recirculate right after the expansion point if it has high velocity. If the flow path is contracted at a point, the flow would recirculate right before entering the contraction point, if it has high velocity. In the tortuous flow paths, depending on the extent of tortuosity and the velocity of the fluid, the fluid might recirculate at the sharp corners of the bents. The recirculation of the fluid at a point would decrease the streamwise bulk flow velocity and therefore would lead to permeability reduction. This phenomenon happens in highly porous and permeable media.

To test the mass flow rate and scaled permeability relationship, several irregular 3D porous structures were designed and the body force driven flow with a wide range of accelerations was simulated in them. Table 5-1 represents the characteristics and geometry of the designed structures and simulations.

Table 5-1: The schematics and characteristics of the different porous structures used to study the inertial effects in body force driven flow.

Structure	Characteristics
<p>Pipe-sphere</p> 	<p>mesh size: $80 \times 44 \times 44$ voxels pipe diameter: 20 voxels sphere diameter: 40 voxels g range: $10^{-10} - 5 \times 10^{-4}$ LBM viscosity: 0.025 Re range: 0-10</p>
<p>Pipe-cube</p> 	<p>mesh size: $80 \times 44 \times 44$ voxels pipe diameter: 20 voxels cube length: 40 voxels pipe length: 20 voxels g range: $10^{-10} - 5 \times 10^{-4}$ LBM viscosity: 0.025 Re range: 0-10</p>
<p>Pipe-ellipsoid</p> 	<p>mesh size: $120 \times 56 \times 56$ voxels pipe diameter: 20 voxels ellipsoid dimensions: 50 & 100 g range: $10^{-10} - 5 \times 10^{-4}$ LBM viscosity: 0.025 Re range: 0-10</p>
<p>Bent channel</p> 	<p>mesh size: $100 \times 64 \times 24$ voxels channel width: 20 voxels length of each pipe section: 20 voxels g range: $10^{-10} - 5 \times 10^{-4}$ LBM viscosity: 0.025 Re range: 0-10</p>
<p>Throat</p> 	<p>mesh size: $120 \times 64 \times 64$ voxels pipe diameter: 20 & 60 voxels length of each pipe section 40 voxels g range: $10^{-10} - 5 \times 10^{-4}$ LBM viscosity: 0.025 Re range: 0-10</p>

Each of the porous structures in table 5-1 represent a unique flow path with different characteristics. The objective of this part of the research was to simulate the full hydrodynamics of body force driven flow processes in these structures and investigate the inertial flow effects on scaled permeability.

The 3D LBM simulator with the half-way bounceback method applied at the wall and periodic boundary condition at the open faces was used to simulate external body force driven flow in the geometries in table 5-1. Before applying the developed LBM simulator, mesh size and viscosity validations were performed. The pipe-cube structure was selected for performing these validations. The pipe diameter was selected as the representative of the mesh size; 4 different sets of mesh with different sizes were programmed, and body force driven flow was simulated. Table 5-2 presents the parameters used for the simulation.

Table 5-2: List of parameters applied in mesh size effect analysis

	Case No. 1	Case No. 2	Case No. 3	Case No. 4
Pipe Diameter (Voxels)	10	20	30	40
Viscosity	0.025	0.025	0.025	0.025
Body force acceleration	5×10^{-4}	$(1/2)^3 \times 5 \times 10^{-4}$	$(1/3)^3 \times 5 \times 10^{-4}$	$(1/4)^3 \times 5 \times 10^{-4}$
Time step	500	500×2^2	500×3^2	500×4^2

To facilitate comparison of results, the simulations were stopped at the same time for all the geometries and this time was before the fully developed state was reached. This means that the comparison was done in the transitional period. The parameters of the simulation for 4 different mesh sizes were calculated considering the dimensional conversion factors represented in table 3-5. Figure 5-2 shows the streamwise velocity at the outlet of each

structure. The relative difference of each case with case number 4 was selected for comparison.

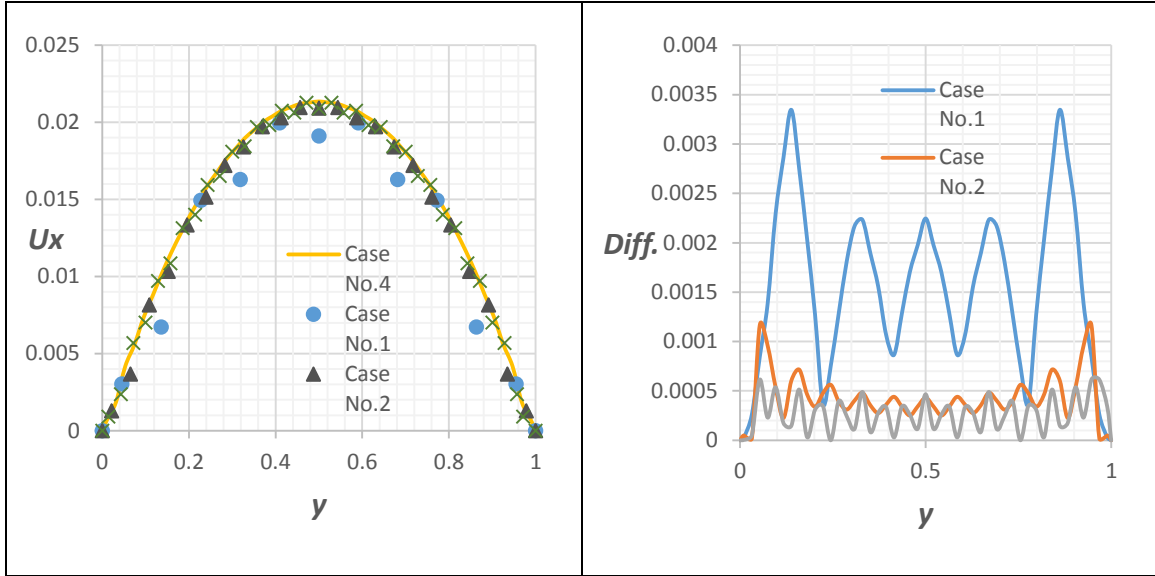


Figure 5-2: The streamwise velocity profile at the exit of the pipe-cube porous structure for 4 different mesh sizes and the relative difference(Diff.) velocity profile of each case with respect the highest resolution case.

As seen in figure 5-2 the velocity profiles for all the four cases are very similar except for case number 1. A part of the velocity difference between the four different cases comes from the fact that the surface of the tube has different relative roughness corresponding to mesh size. Because increasing the pipe size over 20 did not change the results considerably, the resolution of case number 2 was selected to be used for this study.

Viscosity is a major parameter in the stability of the LBM numerical simulation (He *et al.* 1997; Pan & Miller 2006). To investigate the effect of viscosity, a range of viscosity was selected and used in the numerical simulator. In order to keep the Knudsen number below 0.01 and a moderate mesh size, a value of 0.025 for viscosity was chosen. To test the sensitivity of the model, a viscosity range of 0.02-0.035 was used. Based on the

dimensional analysis of table 3-5, the simulation parameters were calculated and assigned.

Table 5-3 summarizes the parameters applied in this part of the study.

Table 5-3: List of parameters applied in viscosity effect analysis.

	Case No. 1	Case No. 2	Case No. 3	Case No. 4
Pipe Diameter (Voxels)	20	20	20	20
Viscosity	0.02	0.025	0.03	0.035
Body force acceleration	5×10^{-4}	$(1.25)^2 \times 5 \times 10^{-4}$	$(1.5)^2 \times 5 \times 10^{-4}$	$(1.75)^2 \times 5 \times 10^{-4}$
Time step	4000	4000/1.25	4000/1.5	4000/1.75

Figure 5-3 represents the streamwise velocity at the outlet for each case of simulation and also the relative error with respect to case number 2 which was selected as the base case.

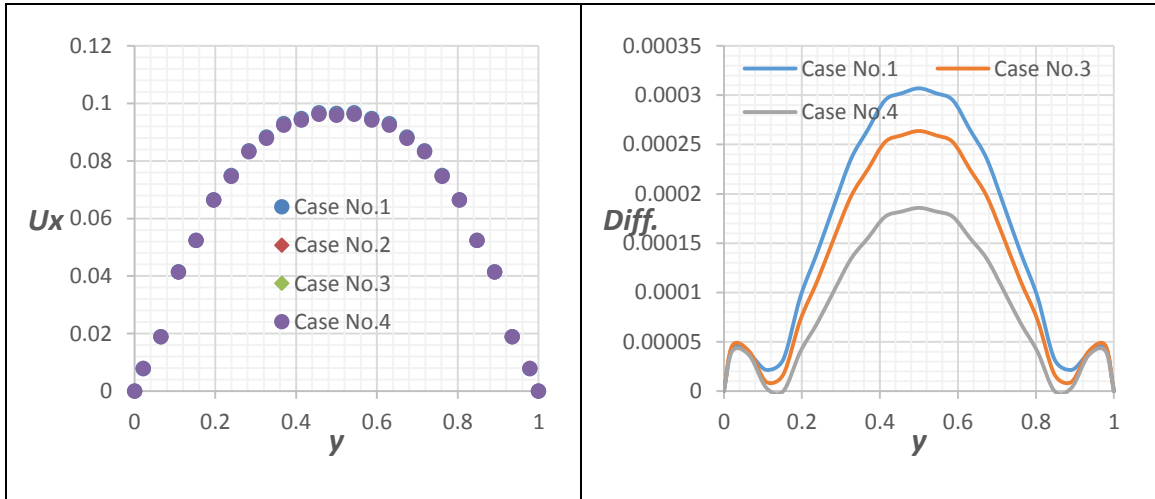


Figure 5-3: The streamwise velocity profiles at the exit of the pipe-cube structure for 4 different viscosity values and the relative difference (Diff.) of each case with respect to case#2.

It is observed in figure 5-3 that changing the viscosity in the selected range does not affect the streamwise velocity noticeably and therefore permeability is not viscosity dependent in the studied range. It has been shown in section 4.2 and some studies that viscosity causes

a slip condition at the solid boundary and has an effect on calculated permeability by LBM (He *et al.* 1997; Pan & Miller 2006; Chai *et al.* 2010). As discussed in chapter 4, the effect of viscosity is important when it causes Kn to increase to values of greater than 0.01. In the present cases the highest calculated Kn was less than 0.0054, and this is the reason that the viscosity effect on calculated permeability is negligible. It should be noted that when the actual model is converted to lattice units and the mesh is programmed, the viscosity and relaxation time must be chosen so that the Kn falls into very low ranges and rarefaction effect do not occur.

The developed LBM simulator was utilized to simulate body force driven flow in each structure in table 5-1 and mass flow rate and scaled permeability in each case were calculated. The same pattern as that illustrated in figure 5-1 was observed in all of the simulation cases in that the scaled permeability drops with increasing mass flow rate with negative second derivate. At an inflection point, k_s'' alters to be positive. The Forchheimer equation was fitted to the simulation results based on the least mean squared error scheme; once for the whole range of mass flow rate and once for the mass flow rate range after the onset of non-Darcy flow. The onset of non-Darcy flow was determined as the point where scaled permeability drops by one percent. Figures 5-4 to 5-8 shows the scaled permeability versus mass flow rate results and the Forchheimer fit.

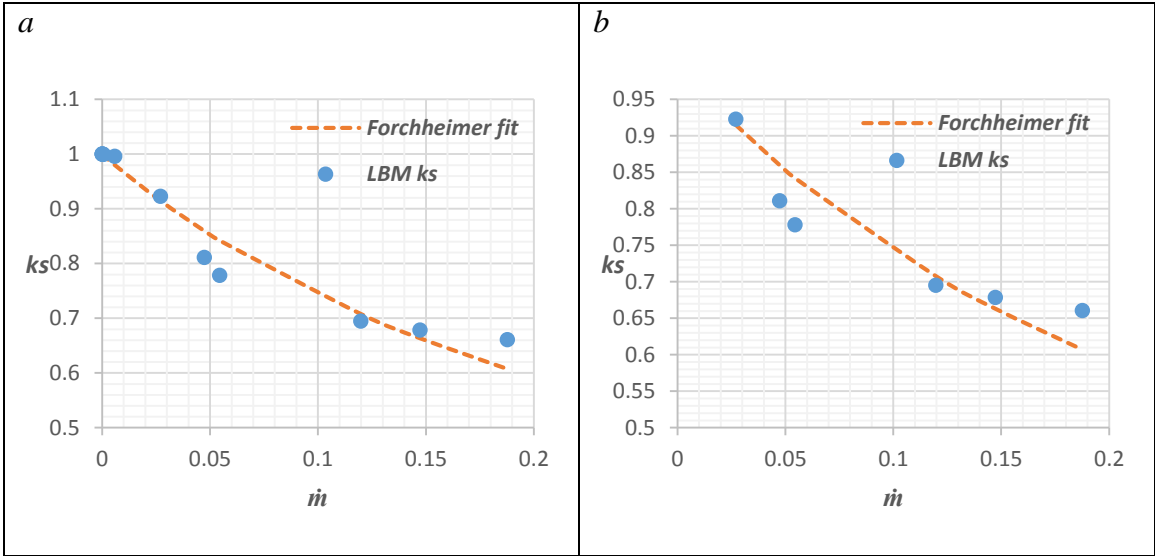


Figure 5-4: Scaled permeability vs. mass flow rate for a range of body force acceleration and the best Forchheimer equation fit for the pipe-sphere structure. a) Data fitted for the whole range of \dot{m} b) Data fitted after non-Darcy onset.

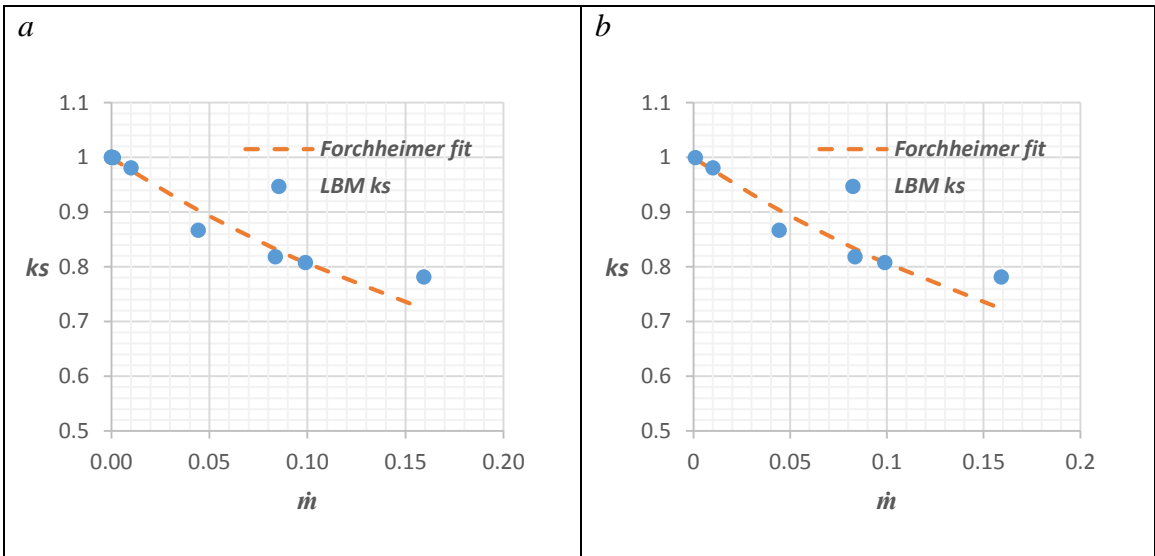


Figure 5-5: Scaled permeability vs. mass flow rate for a range of body force acceleration and the best Forchheimer equation fit for the pipe-cube structure. a) Data fitted for the whole range of \dot{m} b) Data fitted after non-Darcy onset.

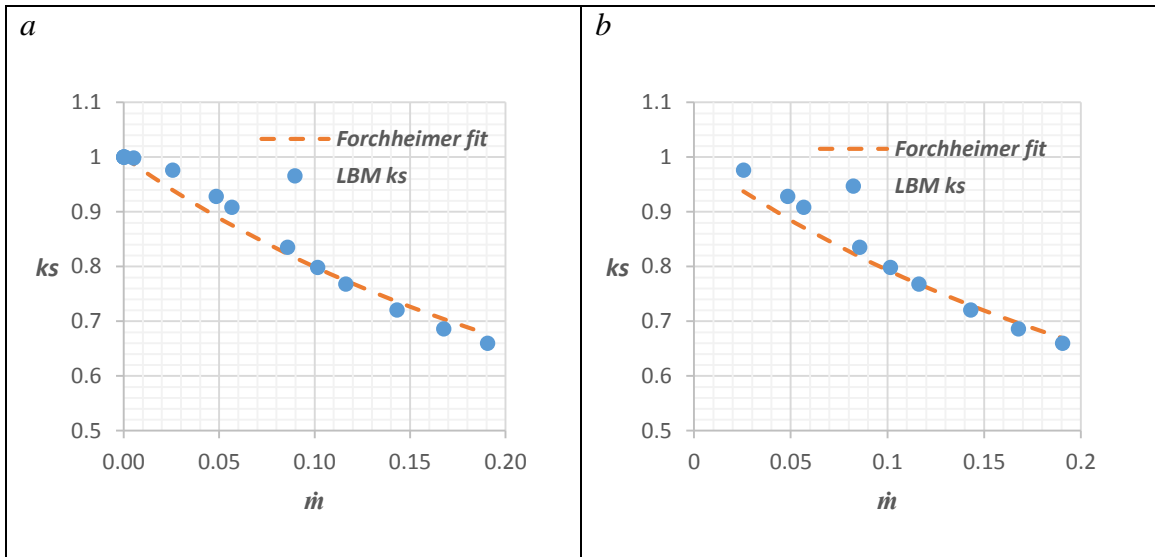


Figure 5-6: Scaled permeability vs. mass flow rate for a range of body force acceleration and the best Forchheimer equation fit for the pipe-ellipsoid structure. a) Data fitted for the whole range of \dot{m} b) Data fitted after non-Darcy onset.

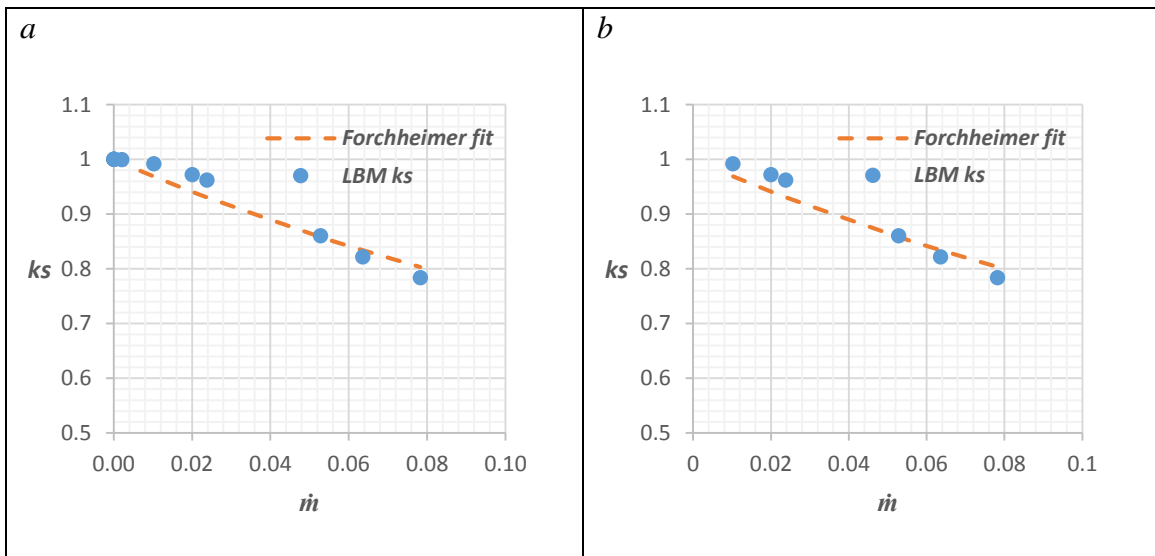


Figure 5-7: Scaled permeability vs. mass flow rate for a range of body force acceleration and the best Forchheimer equation fit for the bent channel structure. a) Data fitted for the whole range of \dot{m} b) Data fitted after non-Darcy flow onset.

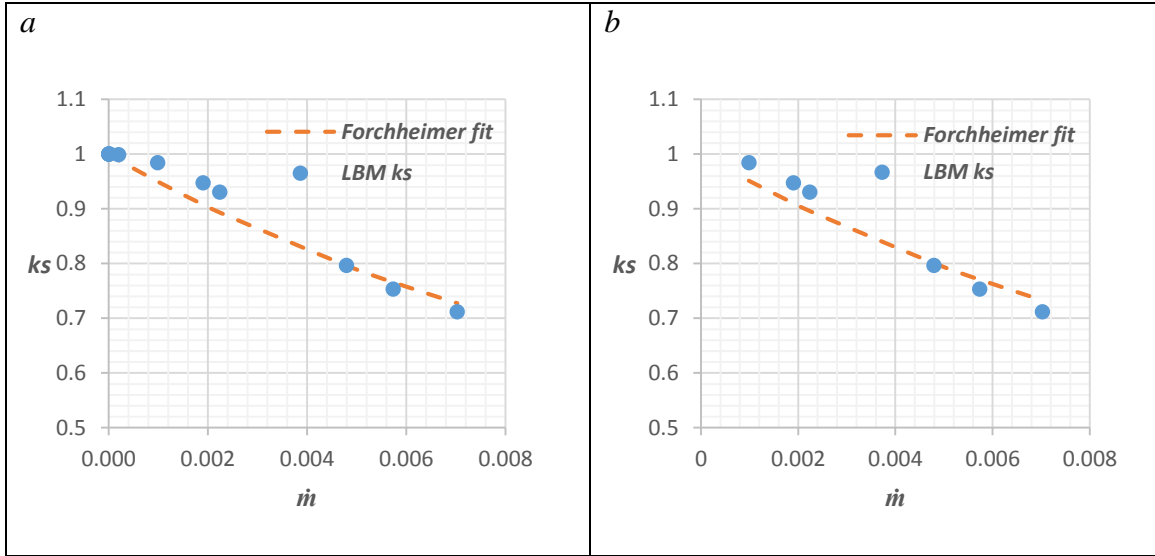


Figure 5-8: Scaled permeability vs. mass flow rate for a range of body force acceleration and the best Forchheimer equation fit for the pipe-throat structure. a) Data fitted for the whole range of \dot{m} b) Data fitted after non-Darcy onset.

As seen in figures 5-4 to 5-8 the Forchheimer equation does not fit the LBM results very well. That is mostly because of the nature of the Forchheimer equation which always has a positive k_s'' . The data points in figures 5-4 to 5-8 show similar patterns. The scaled permeability starts at one and drops by a quadratic trend with negative k_s'' , then at an inflection point the trend of data changes to represent positive k_s'' . However, it is highly unlikely that it would be possible to define a universal criteria to exactly predict these transition points for all types of porous structures. For each type of porous structure, these points can be visually observed in the $ks-\dot{m}$ plot.

For the pipe-ellipsoidal and pipe-cube structures finer simulations were performed. Figures 5-9 & 5-10 show the simulation results and the semi-log plots.

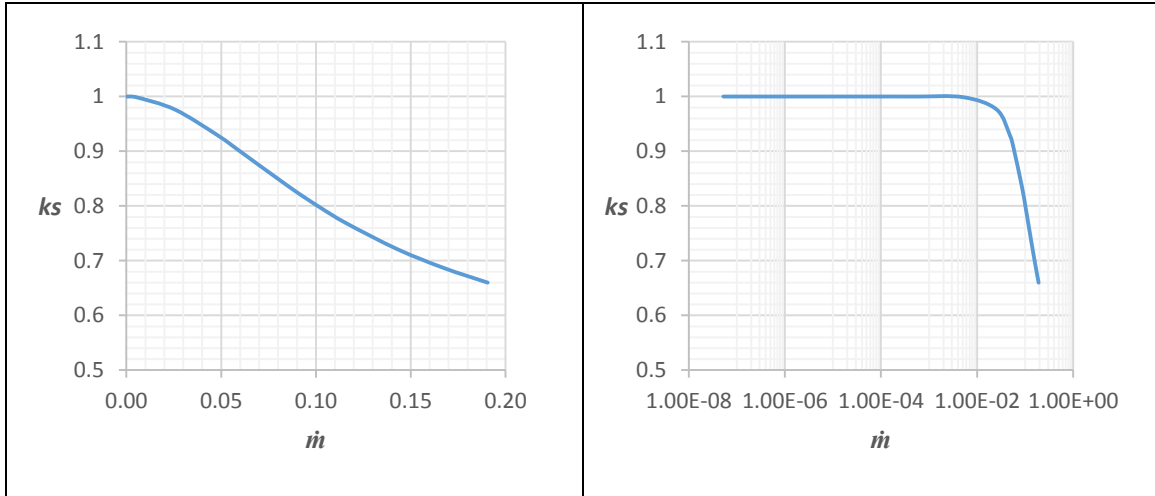


Figure 5-9: The linear and semi-log plots of mass flow rate in lattice units and scaled permeability for the pipe-ellipsoid structure in table 5-3.

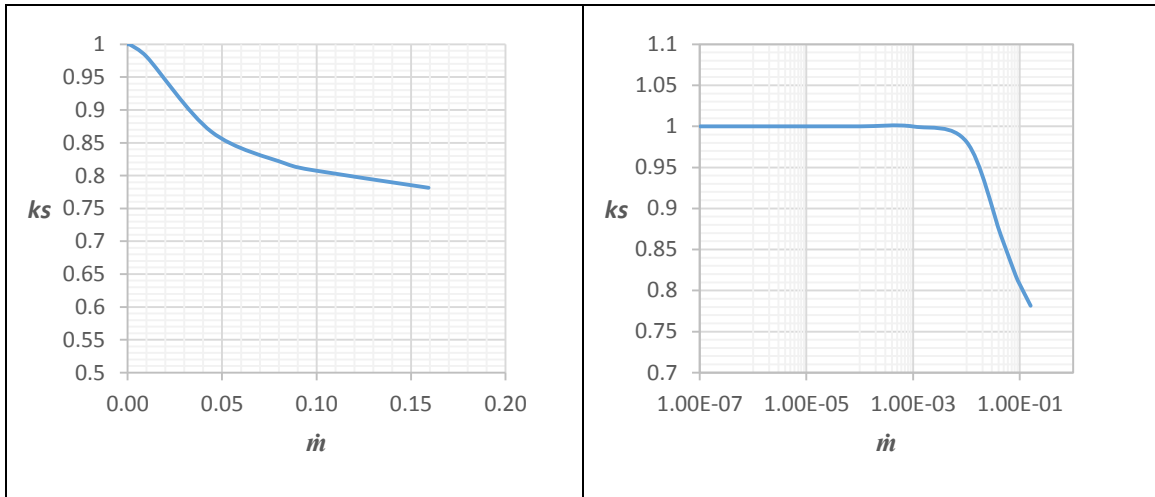


Figure 5-10: The linear and semi-log plots of mass flow rate in lattice units and scaled permeability for the pipe-cube structure in table 5-3.

In figures 5-9 & 5-10 the semi-log plots clearly show the transition point which is the onset of the non-Darcy flow regime where the inertial effects become important. The semi-log plots for the rest of the structures in table 5-1 are provided in Appendix C. Muljadi *et al.* (2016) found similar patterns to the semi-log plots in figures 5-9 & 5-10. The second derivative of scaled permeability with mass flow rate changes sign at the inflection point. The transition points for the pipe-ellipsoid and pipe-cube models were found to occur at

the mass flow rates of 0.00549 and 0.001026 and inflection points were found to be at 0.0566 and 0.01 respectively. To understand what happens at the transition and inflection points, the velocity contours at different mass flow rates were plotted for the two selected structures. Figures 5-11 & 5-12 represent the selected contour graphs. In figure 5-11, as the mass flow rate increases to $\dot{m}=0.00549$ the transition point happens and at the mass flow rate of 0.0566 large vortexes form and the inflection point happens. As the large vortexes start to form, they might act as a lubricating layer that decreases shear forces and friction for the middle part of the bulk flow. This could be the reason for decrease of the slope of the $k_s-\dot{m}$ plot. In other words, the vortexes tend to decrease the permeability because they lower the streamwise mass transport. On the other hand they tend to ease the mass transport at the middle part of the ellipsoid by acting as a lubricant for the high velocity flow at the middle of the channel. It is obvious in figure 5-11 that the flow tends to jet through the channel at high mass flow rate. It is expected that the lowest permeability of the pipe-ellipsoid is when all the fluid jets through the small channel by ignoring the ellipsoid part and that's the lowest permeability that could be reached in laminar flow.

In figure 5-12, the transition point happens right before $\dot{m}=0.001026$. At this point the flow around the corners start to get rounded. In other words, the flow at the transition point avoids the corners and passes through the middle part of the channel. It is possible that very small vortexes happen at the corners. As the flow confines itself more and more to the center of the channel, the scaled permeability reaches the inflection point where obvious large vortexes start to form and grow (around $\dot{m}=0.01$). It appears that the formation of large vortexes coincides with the inflection points in the scaled permeability curve.

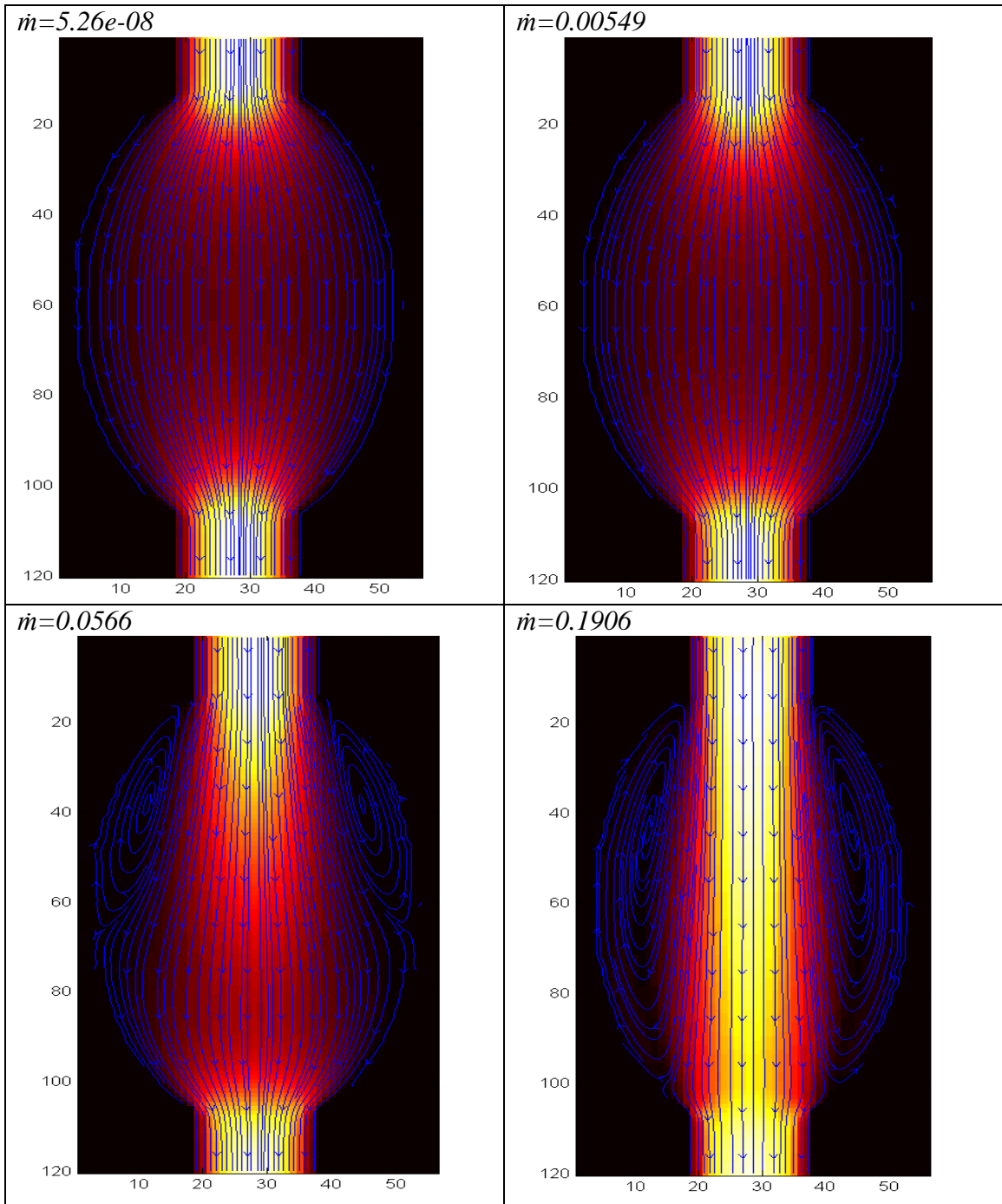


Figure 5-11: Velocity contours at a range of mass flow rate at the middle plane of the pipe-ellipsoid structure. The absolute black color shows the solid part and the brightness of the color inside the brown channel represents the flow velocity.

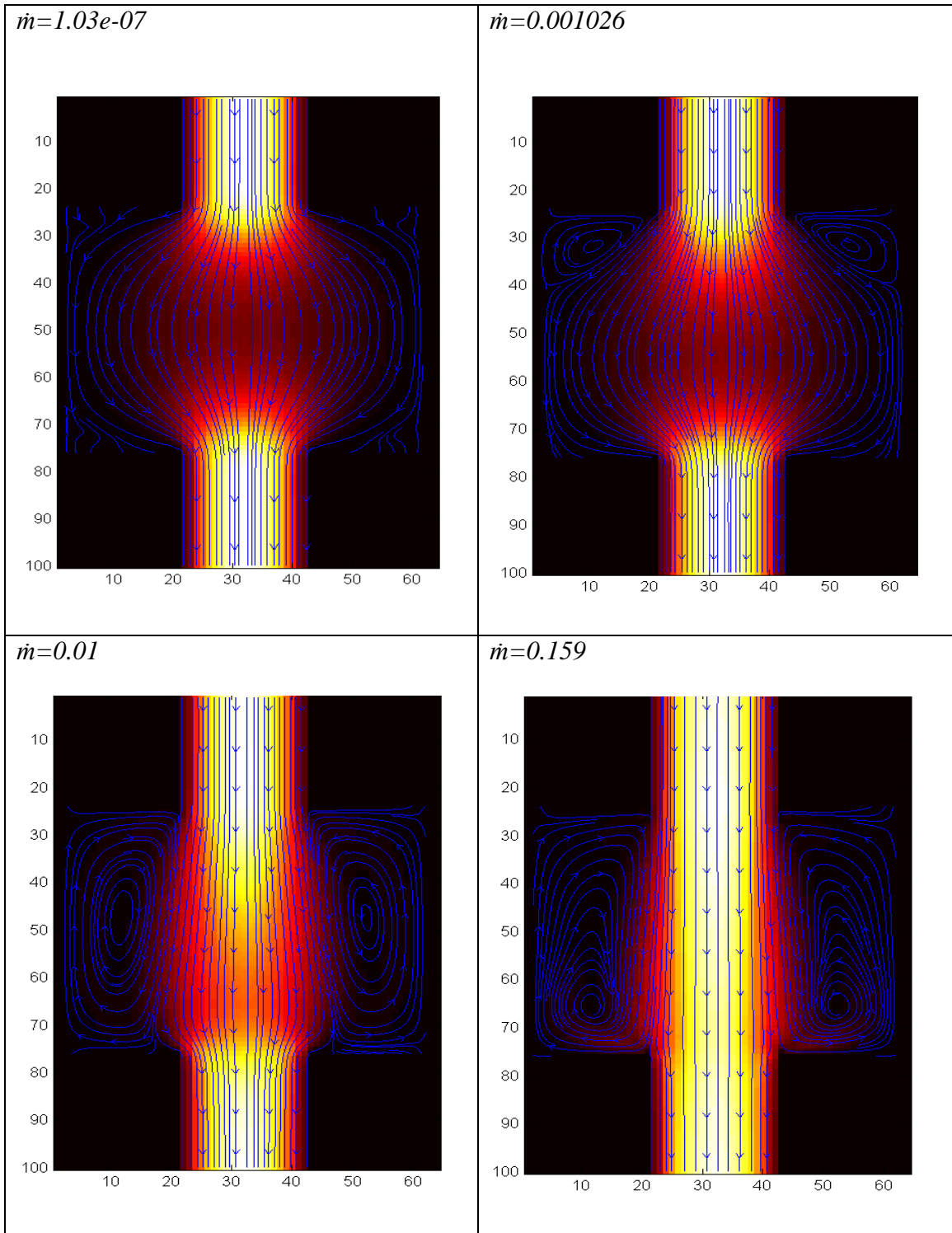


Figure 5-12: Velocity contours at a range of mass flow rate at the middle plane of the pipe-cube structure. The absolute black color shows the solid part and the brightness of the color inside the brown channel represents the flow velocity.

Based on the observations in figures 5-11 and 5-12, the inflection point happens when the large vortexes start to form and expand size quickly. As the vortexes expand, their effect on permeability drop decreases and that probably causes the inflection point in the mass flow rate-scaled permeability profile.

It is also seen in all of the figures that as the mass flow rate and the body force increase, the fluid tends to jet through the channel. In other words, a smaller portion of the porous medium is taken up by the major part of the flow. The sharp parabolic trend fall of scaled permeability at low mass flow rates is because the vortexes are forming and growing in size. The vortexes decrease the streamwise mass transfer and therefore reduce the apparent permeability. At the inflection point the vortexes has reached to their mature size and their growth becomes very slow. That is when the rate of scaled permeability fall decreases and therefore an inflection point happens.

Natural porous media that exists in underground hydrocarbon reservoirs can have very complex porous structures. However, the same phenomenon as the simple structures should happen in natural porous media as long as the flow is in the laminar regime. To investigate the flow process in a natural porous medium, body force driven flow was simulated in a porous structure generated by Micro-CT scanning of a Berea sandstone (Imperial College London Website, 2016). To get an idea of the complexity of this porous structure, figure 5-13 is a representation.

A $200 \times 200 \times 200$ voxels mesh was programmed to represent the structure in figure 5-13 and the LBM simulator was used to model the body force driven flow in the porous sample with viscosity of 0.025 and a g range of 10^{-10} to 10^{-14} in lattice units.

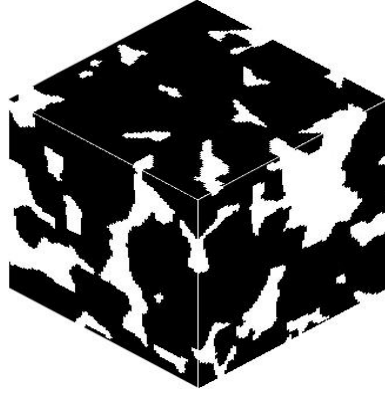


Figure 5-13: The schematic of the Berea sandstone porous structure. The black fill represents the solid part and the white fill is the void space. The length of each side of the cube is 1mm (Imperial College London Website, 2016).

Figure 5-14 represents the scaled permeability and mass flow rate dependency obtained by a series of driving forces performed on the Berea porous digital rock sample. In figure 5-14 the scaled permeability and mass flow rate results of numerical simulation for the range of mass flow rate up to the inflection point and the whole simulation range with the best Forchheimer fit are provided.

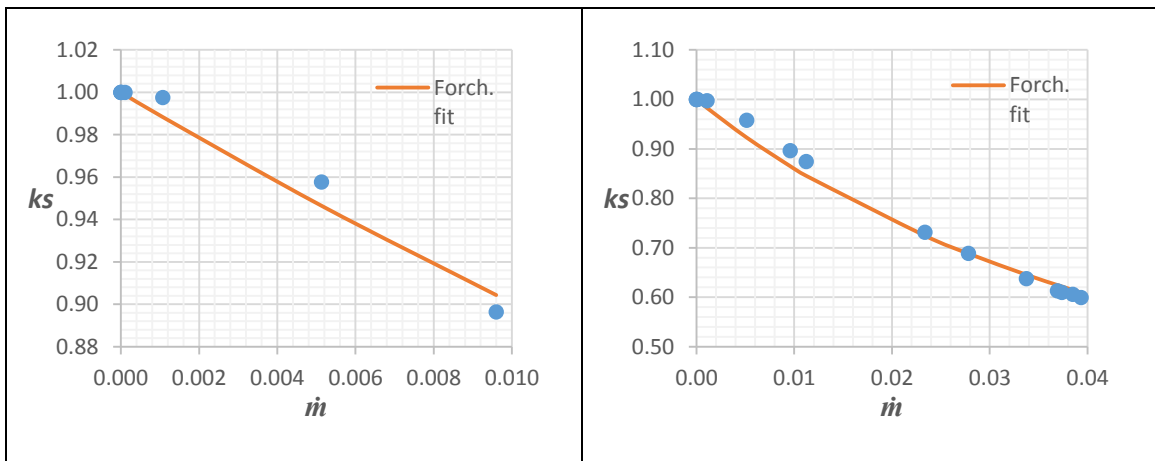


Figure 5-14: The mass flow rate in lattice units and scaled permeability relationship for the Berea porous rock sample. The two graphs are generated for two ranges of mass flow rates.

It is seen in figure 5-14 that for a natural porous medium the scaled permeability and mass flow rate relationship is very similar to that of the simple porous structures in table 5-1 in that they have transition and inflection points. It is also clear that the Forchheimer equation is not capable of matching the numerical simulation results very well, especially for the first few points where mass flow rate is low. It is also observed that the Forchheimer equation predicts the onset of non-Darcy flow to be at considerably lower mass flow rate than the LBM simulation results.

It was observed in all the different studied porous structures that the laminar inertial effects result in dropping permeability in similar patterns. At lower mass flow rates there exists a transition point where the non-Darcy flow begins and permeability starts to drop by a parabolic-type trend with negative k_s'' and then at an inflection point the rate of the permeability drop starts to decrease and k_s'' changes to positive. The Forchheimer equation fails to predict the change in permeability because of its nature – a positive k_s'' for all mass flow rate ranges.

A more suitable function to fit the data trend in figure 5-14 must have the following characteristics:

1. It should have a limit of 1 at low mass flow rates
2. It should have an inflection point
3. It should have negative k_s'' s before the inflection point and positive k_s'' s after the inflection point
4. It should approach zero as mass flow rate approaches infinity

A polynomial ratio function was proposed for this purpose. It was tested and verified that a polynomial ratio function of the form given by the equation:

$$k_s = \frac{1 + a\left(\frac{\dot{m}}{A}\right)^{b_1}}{1 + a\left(\frac{\dot{m}}{A}\right)^{b_2}} \quad (5.1)$$

fits the $k_s \cdot \dot{m}$ data very well. Here a , b_1 and b_2 are constants to be set by fitting techniques, \dot{m} is the mass flow rate and A is the flow area. Equation 5.1 was found by mathematical analysis to fit the characteristics listed above. Figure 5-15 represents the new correlation fit for the results of Berea sample flow simulation (area is assumed to be equal to 1).

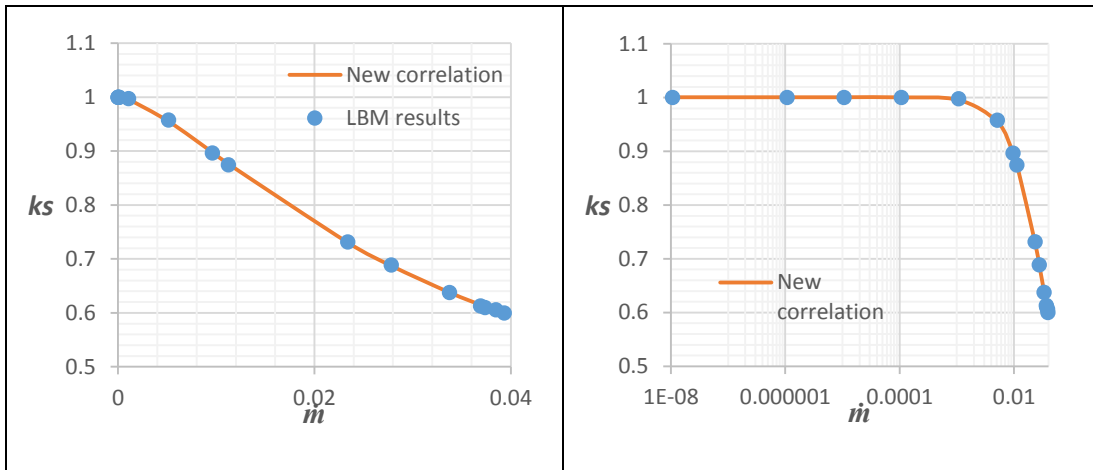


Figure 5-15: The linear and semi-log plot of mass flow rate in lattice units and scaled permeability for the Berea sandstone structure and the new proposed correlation fit.

The mean squared error for the fitted curves in figure 5-15 is in the order of 10^{-7} . However, it should be noted that the fitted empirical correlation of equation 5.15 is only valid in the range of fitted data and extrapolation might lead to invalid results. Also for the best fitting results, the mass flow rate input should be scaled to fall into low ranges.

5.2 Unsteady-State Core Flow Tests

To check the accuracy of equation 5.1, flow tests were performed by the experimental set-up described in section 3.3. In these tests the downstream section was connected to the ambient. Five different artificial porous samples each consisting of 5 connected pipes with different lengths and diameters were built by milling PVC plastic rods. The 5 pipe sections were connected to make flow lines similar to figure 3-11. Table 5-4 presents the specifications of the designed samples.

The structures in table 5-4 are not considered highly irregular when compared to natural porous media. Flow tests were conducted using the constructed porous samples. The upstream chamber with volume of *145 cc* was charged to a pressure of *320 kPa* and the chamber was then allowed to discharge to the ambient through the porous samples.

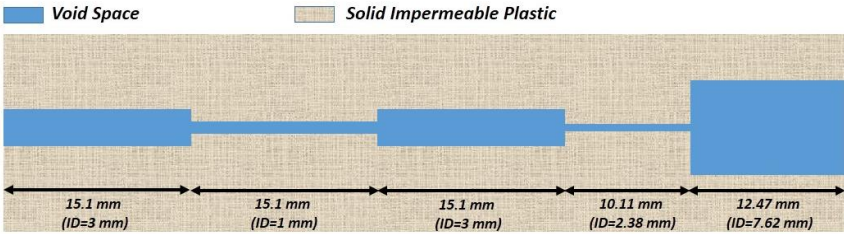
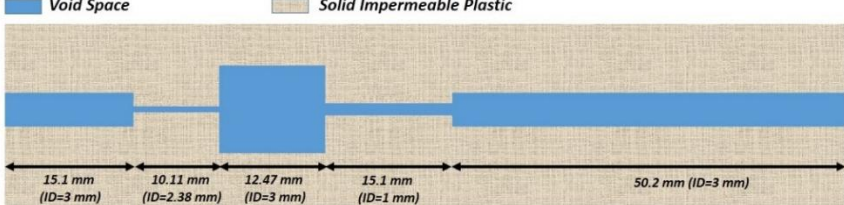
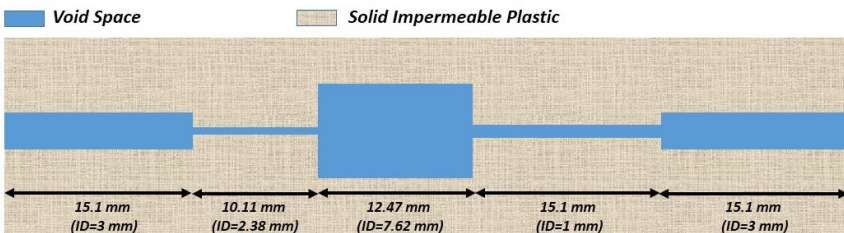
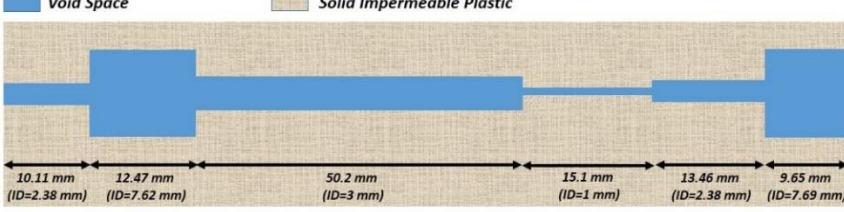
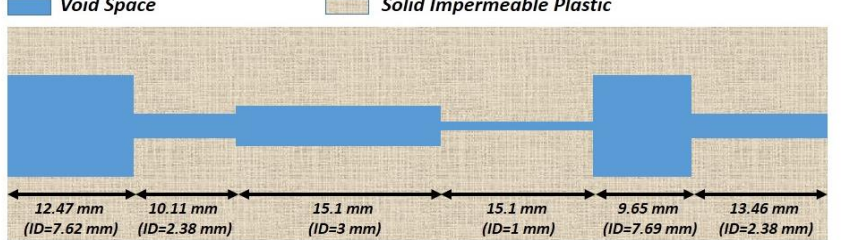
Because the pore volume of the samples was very small compared to the chamber volume, the gas accumulation in the pore volume was ignored and the unsteady state test was treated like a series of steady multi-flow tests. The basic assumption is that mass flow rate is constant through the whole length of the sample at a specific time, the same assumption that was used by Brace *et al.* (1968) in their design of a transient permeameter.

The Darcy equation with the ideal gas law was applied to obtain flow rate dependent permeability as:

$$k = -\frac{\dot{m}\mu RTL}{A\bar{P}\Delta P} \quad (5.2)$$

where \bar{P} is the arithmetic mean pressure in the sample, L is the length and A is the sample cross sectional area which is assumed to be 1 cm^2 for all of the structures for simplicity.

Table 5-4: The specifications of the tube combinations designed for flow tests.

Structure	Characteristics
 <p>Void Space Solid Impermeable Plastic</p>	<p>Combination#1 Pore Volume: 0.84 cc Length: 67.9 mm</p>
 <p>Void Space Solid Impermeable Plastic</p>	<p>Combination#2 Pore Volume: 0.61 cc Length: 103 mm</p>
 <p>Void Space Solid Impermeable Plastic</p>	<p>Combination#3 Pore Volume: 0.84 cc Length: 67.9 mm</p>
 <p>Void Space Solid Impermeable Plastic</p>	<p>Combination#4 Pore Volume: 1.49 cc Length: 111 mm</p>
 <p>Void Space Solid Impermeable Plastic</p>	<p>Combination#5 Pore Volume: 1.24 cc Length: 75.9 mm</p>

The mass flow rate was calculated by utilizing the upstream chamber pressure drop rate as:

$$\dot{m} = -\frac{V_{ch}}{RT} \frac{dP_{ch}}{dt} \quad (5.3)$$

where V_{ch} and P_{ch} are the chamber volume and pressure respectively. Therefore the apparent permeability is calculated as:

$$k = -\frac{dP_{ch}}{dt} \frac{V_{ch}\mu L}{A\bar{P}\Delta P} \quad (5.4)$$

Figure 5-16 to 5-20 show the pressure decline curve and scaled permeability-mass flow rate graph calculated for the flow test results.

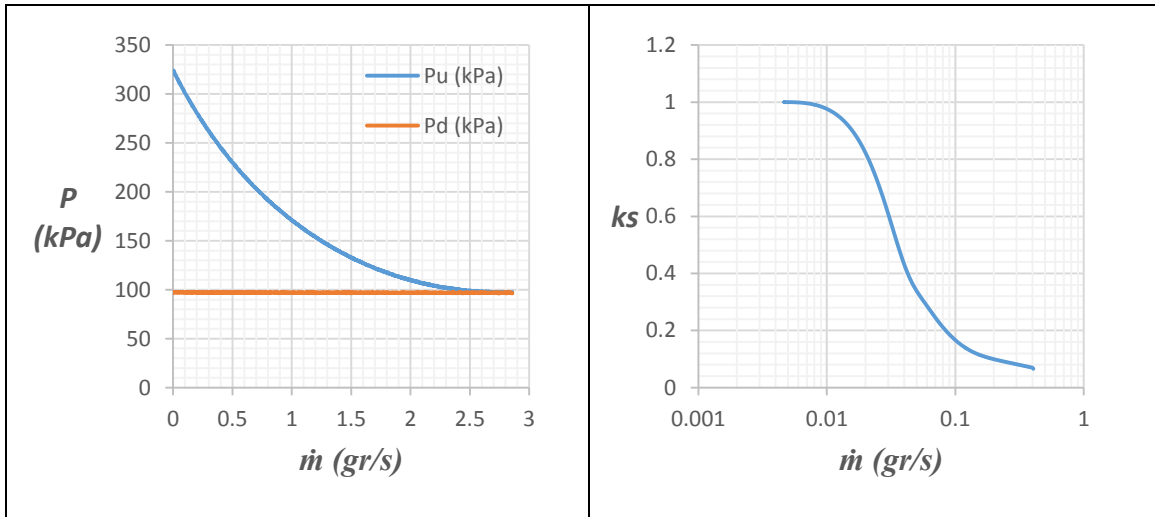


Figure 5-16: Left: The pressure decay profile of upstream chamber (Pu) and the downstream pressure profile (Pd). Right: The scaled permeability vs. mass flow rate in a semi-log plot for the structure#1.

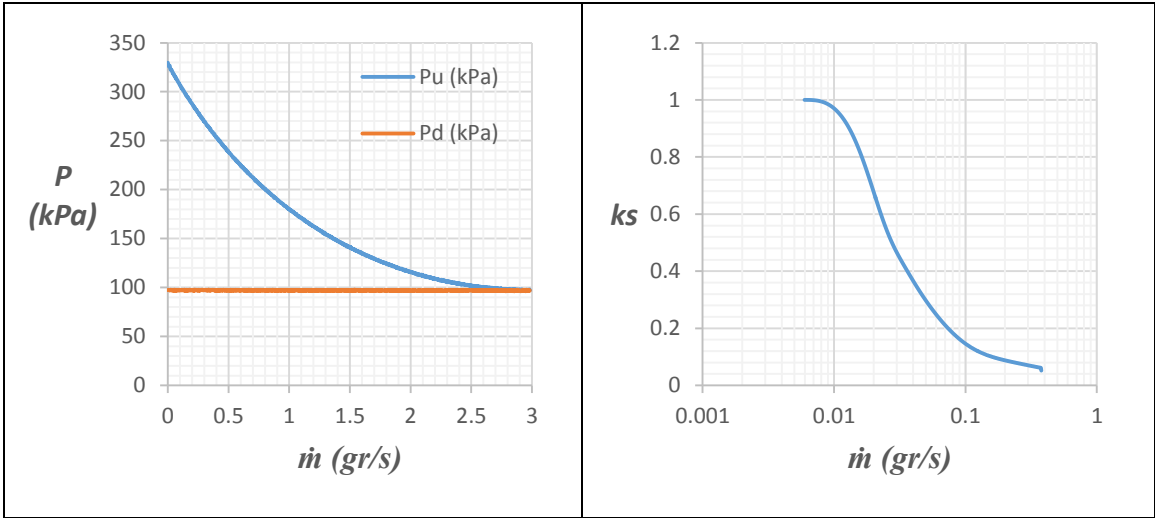


Figure 5-17: Left: The pressure decay profile of upstream chamber (P_u) and the downstream pressure profile (P_d). Right: The scaled permeability vs. mass flow rate in a semi-log plot for the structure#2.

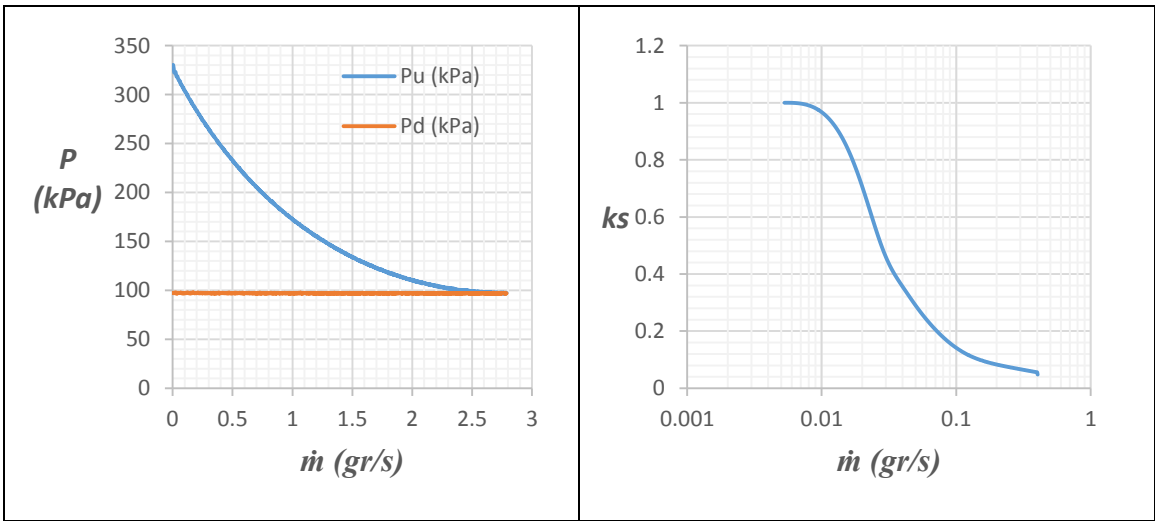


Figure 5-18: Left: The pressure decay profile of upstream chamber (P_u) and the downstream pressure profile (P_d). Right: The scaled permeability vs. mass flow rate in a semi-log plot for the structure#3.

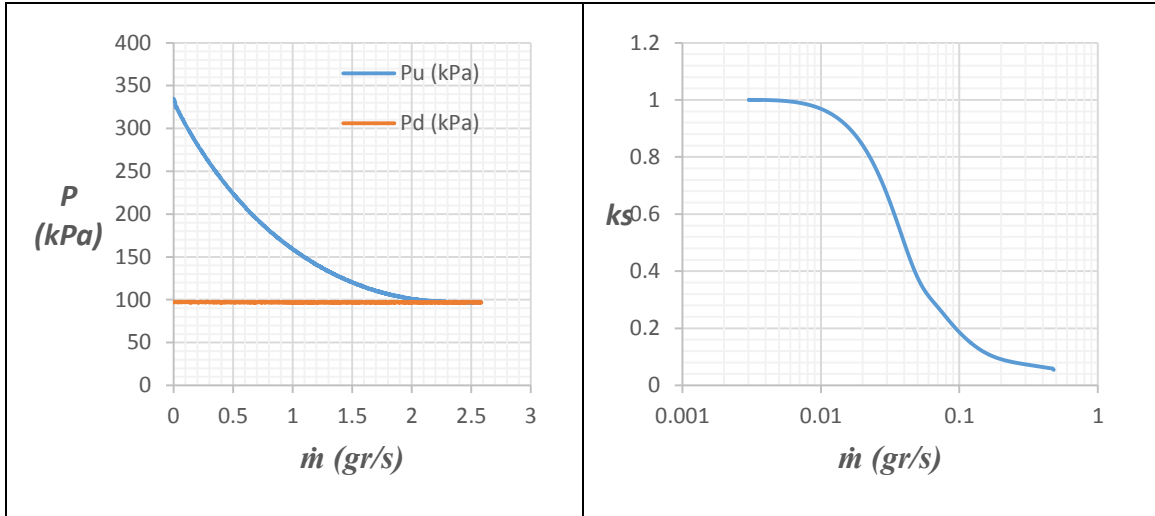


Figure 5-19: Left: The pressure decay profile of upstream chamber (P_u) and the downstream pressure profile (P_d). Right: The scaled permeability vs. mass flow rate in a semi-log plot for the structure#4.

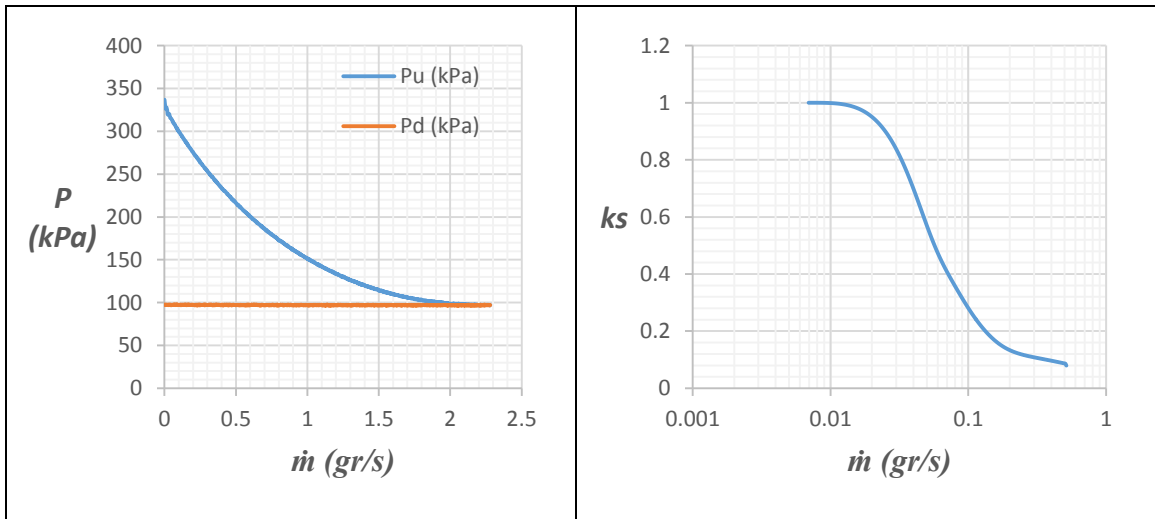


Figure 5-20: Left: The pressure decay profile of upstream chamber (P_u) and the downstream pressure profile (P_d). Right: The scaled permeability vs. mass flow rate in a semi-log plot for the structure#5.

The developed correlation (equation 5.1) and the Forchheimer equation (equation 2.3) were used to fit the simulation results in figures 5-16 to 5-20. For the purpose of performing generalized fitting, instead of mass flow rate, the mass flux ($\dot{m}_s = \dot{m}/A$) was used. The MATLAB curve fitting toolbox was implemented to calculate the fitting parameters.

Figures 5-21 to 5-25 show the simulation results compared to Forchheimer and the proposed model (equation 5.1) predictions.

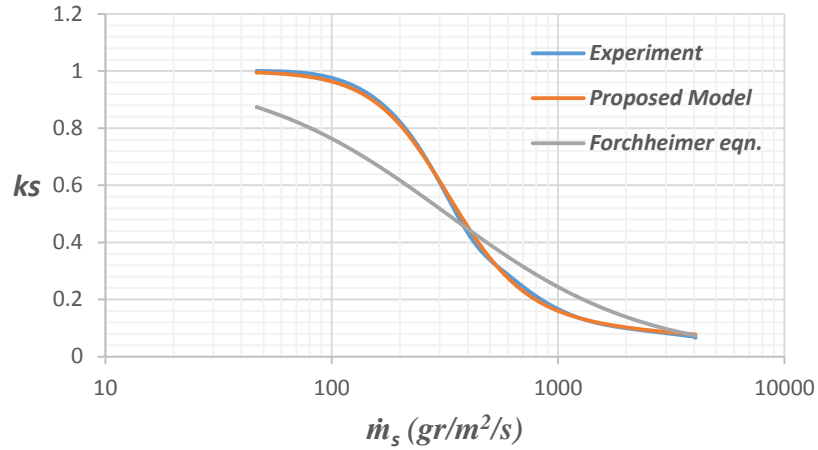


Figure 5-21: Comparison of scaled permeability fitting of the proposed model (equation 5.1) and the Forchheimer model (equation 2.3) by experimental results of structure#1.

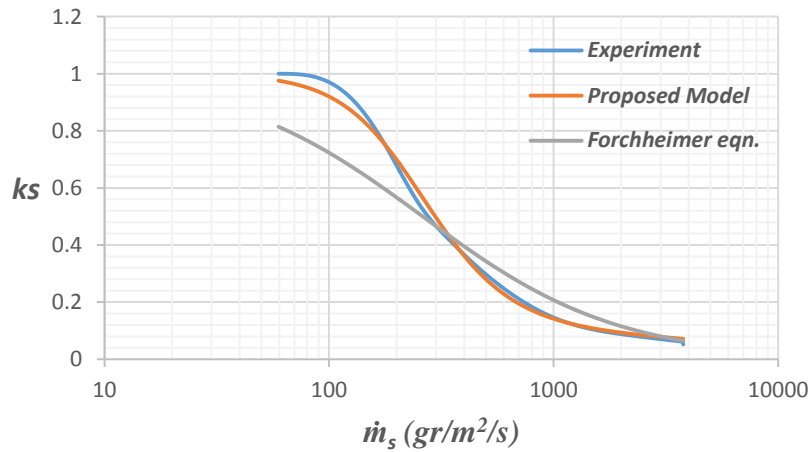


Figure 5-22: Comparison of scaled permeability fitting of the proposed model (equation 5.1) and the Forchheimer model (equation 2.3) by experimental results of structure#2.

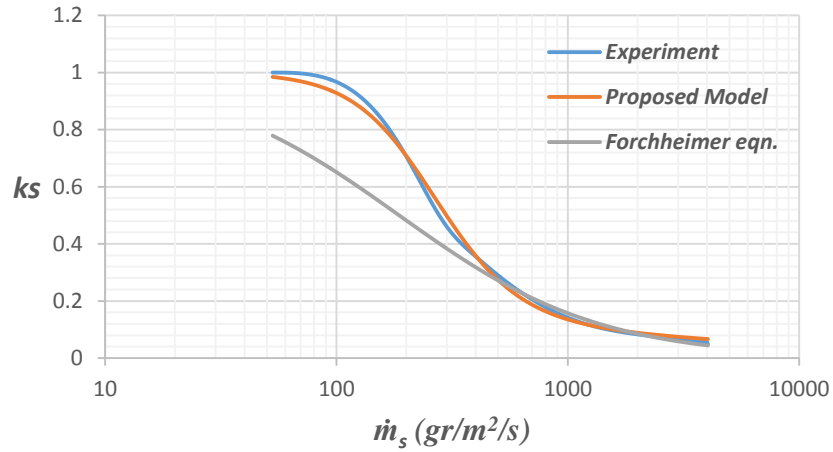


Figure 5-23: Comparison of scaled permeability fitting of the proposed model (equation 5.1) and the Forchheimer model (equation 2.3) by experimental results of structure#3.

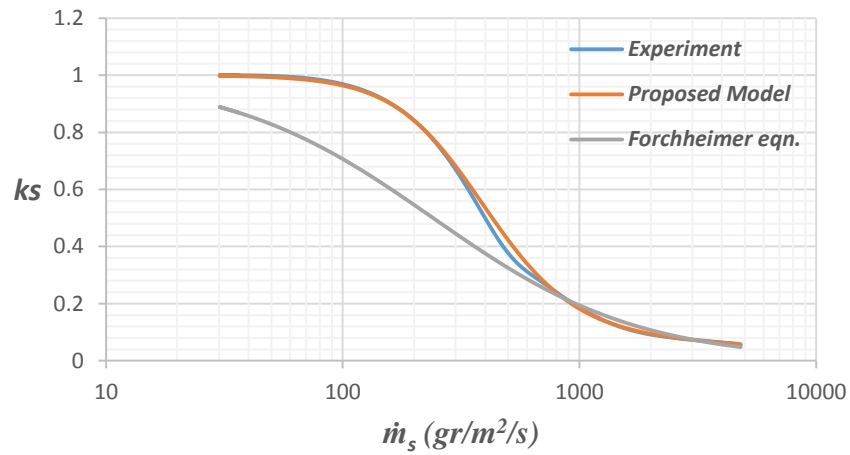


Figure 5-24: Comparison of scaled permeability fitting of the proposed model (equation 5.1) and the Forchheimer model (equation 2.3) by experimental results of structure#4.

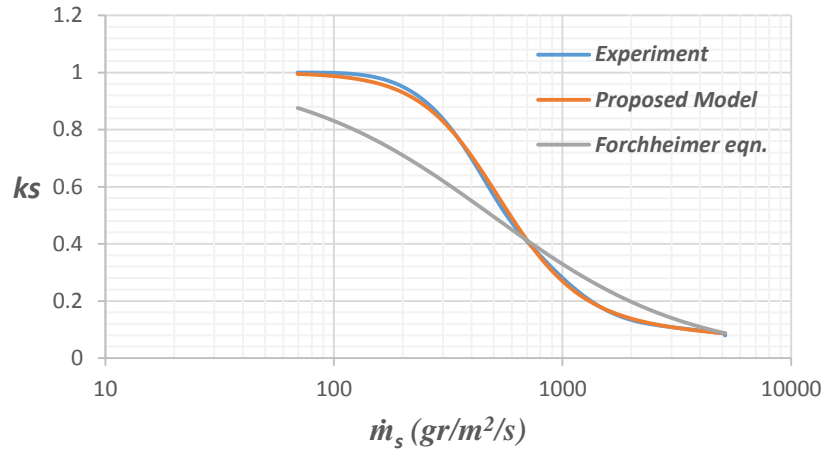


Figure 5-25: Comparison of scaled permeability fitting of the proposed model (equation 5.1) and the Forchheimer model (equation 2.3) by experimental results of structure#5.

As it is seen in figures 5-21 to 5-25, the proposed correlation matches the experimental flow results very well while the Forchheimer model is incapable of fitting the whole range of data.

CONCLUSIONS AND RECOMMENDATIONS FOR FUTURE WORKS

In this chapter the major contributions of the present study to the current literature is reported as the conclusions and some suggestions for future studies are listed.

6.1 Conclusions

In this research 2D and 3D Lattice Boltzmann Method based simulators were developed using orders of Gauss-hermite quadrature that were appropriate for the orders of the Hermite polynomials expansion of the equilibrium distribution function. Furthermore, body force driven flow was used to simplify the injection/production boundaries and the wall condition was set such that the accommodation time was zero. The developed 2D and 3D LBM simulators were validated by the analytical solution result of laminar flow in channels and tubes respectively. It was also tested and observed that the permeability of an irregular geometry predicted by the body force driven flow simulated by the 3D LBM simulator is very close to the experimental results performed by gravity driven flow.

This thesis contains a number of related studies, each of which provides unique contributions. In the first part of the work, the Lattice Boltzmann method utilizing different levels of Hermite polynomials expansions was used to investigate the flow regimes beyond the slip flow. The unique findings and contributions of this part of the thesis are listed below.

- A new formula ($Kn = \frac{\vartheta}{N_y c_s} \sqrt{\frac{\pi}{2}}$) was developed that relates Knudsen number and viscosity in lattice units. Using the proposed equation, the Knudsen's minimum was determined with three different orders of accuracies (D2Q9, D2Q21, and D2Q37), and it was observed that in all three cases the minimum happens around $Kn \approx 0.7$. That is consistent with experimental data reported in the literature.
- It was shown that there is not a linear direct relationship between the specular reflection coefficient (rf) and flow rate at low Kn flow. In fact, for the rf values of less than 0.8 the specular reflection did not affect the flow rate considerably. However, when rf was approaching 1, the flow rate was increased by 300 percent.
- A corrected bounceback method was presented for the D2Q21 scheme. Using the proposed scheme unique accommodation time can be applied to all discrete velocities.
- It was shown that the low order LBM combined with specular boundary condition does not represent the high Kn flow regimes very well. Actually the low order LBM method (D2Q9), over-predicts the flow rate when applied with the half-way bounceback condition. Using combined half-way bounceback and specular condition at the wall makes the results more inconsistent with the higher accurate LBM models (D2Q21, D2Q37).
- It was found that truncating the equilibrium distribution function at the 3rd and 4th order show the same prediction for mass flow rate in the channel at high Kn , while truncating at the 2nd order results in over-prediction.
- The constants of equation 4.6 ($K = K_{abs}(1 + 6C_1Kn + 12C_2Kn^2)$) for a two dimensional channel was calculated by the LBM simulation results. It was found that the constants of equation 4.6 should be calculated in different ranges of Kn . The

calculated values of the constants were compared with suggested values in the literature and the closest match was found to be with the values presented by Mitsuya (1993).

- It was shown by simulation results that the relationship of Kn and permeability is not linear, like the Klinkenberg equation, or second order polynomial, but it can be fitted with polynomials in different Kn ranges.
- The results of the current study showed that the first order Knudsen term in equation 4.6 has relatively low importance and it could be ignored.

In the second section of this research the full hydrodynamics of fluid flow in three dimensional porous geometries with varying flow path characteristics were simulated and the laminar inertial effects on the apparent permeability was studied. The unique findings and contributions of this part of the work are as follows:

- It was found that for each individual geometry with a single inlet and single outlet the introduced scaled permeability decreases with increasing mass flow rate in the system. The onset of the non-Darcy flow – where the inertial effects start to take an important part in the pressure drop – is very clear in each flow path. The onset of the non-Darcy flow in each porous geometry is different.
- It was observed in the simulation results that the laminar inertial effects cause the permeability to drop gradually with transition and inflection points. The transition point is the onset of the non-Darcy flow where permeability starts to drop by a quadratic trend with negative curvature and at the inflection point the curvature changes sign to be positive.
- It was demonstrated that the nature of the Forchheimer equation results in an absolute positive k_s'' . This means that it does not include any inflection point.

Although the Forchheimer equation fits some of the mass flow rate-scaled permeability results reasonably (with an error of lower than 10%), the Forchheimer type equation cannot fit the trend of permeability-mass flow rate data with an inflection point. This problem with the Forchheimer equation is more obvious in the range of low mass flow rate where k_s'' is negative.

- A new empirical correlation (equation 5.1) was proposed to fit the scaled permeability-mass flow rate relationship. The advantage of the proposed equation comparing to the Forchheimer equation is that equation 5.1 includes an inflection point while the Forchheimer equation leads in an absolute convex curve. Comparisons showed that the new empirical correlation proposed in this research matches the simulation and experimental results far better than the Forchheimer equation.

6.2 Recommendations for Future Studies

This study provides permeability reduction models for single phase flow in porous media in the full range of rarefied gas and laminar flow. However, additional work could be performed to add to the current knowledge. To do so, the following suggestion are proposed:

- To provide a global equation which predicts the mass flow rate and scaled permeability relationship with no fitting parameter that works for all types of porous geometries, the effective properties of the geometries must be included. Introducing a few general properties of the porous medium is not practically enough to accurately predict the flow properties in a complicated porous media. It is

suggested to investigate the relation of the constants of equation 5.1 with intrinsic characteristics of porous media (porosity, permeability and tortuosity).

- In this study body force driven flow was simulated and the inlet/outlet condition was modeled accurately by periodic boundary condition. However, in certain cases velocity and pressure boundary conditions need to be applied. It is suggested that the issue of applying the Dirichlet and Von-Neumann boundary conditions for higher order discrete velocity sets be studied in future works.
- In this study the curved boundaries in the pipes were built by fine mesh sizes and that would be equivalent to a rough curved surface. Since the roughness was not an issue in this research, there was no need to modify the applied methods to model smooth curved surfaces. Studying different methods that could be used to model smooth curved surfaces is recommended for future studies.

BIBLIOGRAPHY

- Anon, Berea sandstone, Imperial College London. Available at: <http://www.imperial.ac.uk/earth-science/research/research-groups/perm/research/pore-scale-modelling/micro-ct-images-and-networks/berea-sandstone/> [Accessed December 15, 2016].
- Arabjamaloei, R. & Ruth, D.W., 2016. Lattice Boltzmann based simulation of gas flow regimes in low permeability porous media: Klinkenberg's region and beyond. *Journal of Natural Gas Science and Engineering*, 31, pp.405–416.
- Aristov, V., 2001. *Direct methods for solving the Boltzmann equation and study of nonequilibrium flows*, Springer Science & Business Media.
- Arkilic, E.B., Breuer, K.S. & Schmidt, M.A., 2001. Mass flow and tangential momentum accommodation in silicon micromachines channels. *Journal of Fluid Mechanics*, 437, pp.29–43.
- Arkilic, E.B., Schmidt, M.A. & Breuer, K.S., 1997. Gaseous slip flow in long microchannels. *Journal of Microelectromechanical Systems*, 6(2), pp.167–178.
- Arns, C.H. et al., 2004. Virtual permeametry on microtomographic images. *Journal of Petroleum Science and Engineering*, 45(1), pp.41–46.
- Ashrafi Moghadam, A. & Chalaturnyk, R., 2014. Expansion of the Klinkenberg's slippage equation to low permeability porous media. *International Journal of Coal Geology*, 123, pp.2–9.
- Balhoff, M. & Wheeler, M., 2009. A predictive pore-scale model for non-Darcy flow in porous media. *SPE Journal*.
- Beskok, A. & Karniadakis, G., 1999. Report: A model for flows in channels, pipes, and ducts at micro and nano scales. *Microscale Thermophysical*.
- Bhatnagar, P.L., Gross, E.P. & Krook, M., 1954. A model for collision processes in gases. I. small amplitude processes in charged and neutral one-component systems. *Physical Review*, 94(3), pp.511–525.
- Bird, G.A., 1994. *Molecular gas dynamics and the direct simulation of gas flows*, Clarendon Press.
- Bourbie, T. & Walls, J., 1982. Pulse decay permeability: analytical solution and experimental test. *Society of Petroleum Engineers Journal*, 22(5), pp.719–721.
- Brace, W.F., Walsh, J.B. & Frangos, W.T., 1968. Permeability of granite under high pressure. *Journal of Geophysical Research*, 73(6), pp.2225–2236.
- Cai, C. et al., 2000. Direct simulation methods for low-speed microchannel flows. *Journal of Thermophysics and Heat Transfer*, 14(3), pp.368–378.
- Cercignani, C., 1964. *Higher order slip according to the linearized Boltzmann equation*,
- Chai, Z. et al., 2010. Gas flow through square arrays of circular cylinders with Klinkenberg effect: a Lattice Boltzmann study. *Communications in Computational Physics*.

- Chen, H. & Shan, X., 2008. Fundamental conditions for N-th-order accurate lattice Boltzmann models. *Physica D: Nonlinear Phenomena*.
- Chen, Z.A. & Ruth, D.W., 1993. On Viscosity Correlations Of Natural Gas. In *Annual Technical Meeting*. Petroleum Society of Canada.
- Chikatamarla, S.S. & Karlin, I. V., 2006. Entropy and Galilean invariance of lattice Boltzmann theories. *Physical Review Letters*, 97(19).
- Chikatamarla, S.S. & Karlin, I. V., 2009. Lattices for the lattice Boltzmann method. *Physical Review E*, 79(4), p.46701.
- Chukwudozie, C.P. et al., 2012. Prediction of non-Darcy coefficients for inertial flows through the Castlegate sandstone using image-based modeling. *Transport in Porous Media*, 95(3), pp.563–580.
- Chung, T.H., Lee, L.L. & Starling, K.E., 1984. Applications of kinetic gas theories and multiparameter correlation for prediction of dilute gas viscosity and thermal conductivity. *Industrial & Engineering Chemistry Fundamentals*, 23(1), pp.8–13.
- Cooke, C.E., 1973. Conductivity of Fracture Proppants in Multiple Layers. *Journal of Petroleum Technology*, 25(9), pp.1101–1107.
- Coulaud, O., Morel, P. & Caltagirone, J.P., 1988. Numerical modelling of nonlinear effects in laminar flow through a porous medium. *Journal of Fluid Mechanics*, 190(1), p.393.
- Dadzie, S.K. & Brenner, H., 2012. Predicting enhanced mass flow rates in gas microchannels using nonkinetic models. *Physical Review E*, 86(3), p.36318.
- Deissler, R.G., 1964. An analysis of second-order slip flow and temperature-jump boundary conditions for rarefied gases. *International Journal of Heat and Mass Transfer*, 7(6), pp.681–694.
- Dullien, F.A.L., 1992. *Porous media : fluid transport and pore structure* 2nd ed., San Diego : Academic Press.
- Dybbs, A. & Edwards, R. V., 1984. A New Look at Porous Media Fluid Mechanics — Darcy to Turbulent. In *Fundamentals of Transport Phenomena in Porous Media*. Dordrecht: Springer Netherlands, pp. 199–256.
- Ergun, S., 1952. Fluid flow through packed columns. *Chem. Eng. Prog.*
- Fan, J. & Shen, C., 2001. Statistical Simulation of Low-Speed Rarefied Gas Flows. *Journal of Computational Physics*, 167(2), pp.393–412.
- Fand, R., Kim, B. & Lam, A., 1987. Resistance to the flow of fluids through simple and complex porous media whose matrices are composed of randomly packed spheres. *Journal of*.
- Fathi, E., Tinni, A. & Akkutlu, I.Y., 2012. Correction to Klinkenberg slip theory for gas flow in nano-capillaries. *International Journal of Coal Geology*, 103, pp.51–59.
- Ferziger, J.H. & Kaper, H.G., 1972. *Mathematical theory of transport processes in gases.*, North-Holland Pub. Co.
- Forchheimer, P., 1901. Wasserbewegung durch boden. *Zeitschrift Des Vereines Deutscher Ingenieure*, p.1782:1788.

- Fourar, M. et al., 2004. On the non-linear behavior of a laminar single-phase flow through two and three-dimensional porous media. *Advances in Water*.
- Gad-el-Hak, M., 1999. The Fluid Mechanics of Microdevices—The Freeman Scholar Lecture. *Journal of Fluids Engineering*, 121(1), p.5.
- Geertsma, J., 1974. Estimating the Coefficient of Inertial Resistance in Fluid Flow Through Porous Media. *Society of Petroleum Engineers Journal*, 14(5), pp.445–450.
- Grad, H., 1949. On the kinetic theory of rarefied gases. *Communications on Pure and Applied Mathematics*, 2(4), pp.331–407.
- Guo, Z., Zheng, C. & Shi, B., 2002. An extrapolation method for boundary conditions in lattice Boltzmann method. *Physics of Fluids (1994-present)*.
- Hadjiconstantinou, N.G., 2003. Comment on Cercignani’s second-order slip coefficient. *Physics of Fluids*, 15(8), p.2352.
- Harley, J.C. et al., 1995. Gas flow in micro-channels. *Journal of Fluid Mechanics*, 284(1), p.257.
- He, X. et al., 1997. Analytic solutions of simple flows and analysis of nonslip boundary conditions for the lattice Boltzmann BGK model. *Journal of Statistical Physics*, 87(1–2), pp.115–136.
- He, X. & Doolen, G.D., 2002. Thermodynamic Foundations of Kinetic Theory and Lattice Boltzmann Models for Multiphase Flows. *Journal of Statistical Physics*, 107(1/2), pp.309–328.
- Hill, R., Koch, D. & Ladd, A., 2001. The first effects of fluid inertia on flows in ordered and random arrays of spheres. *Journal of Fluid Mechanics*.
- Ho, C.-M. & Tai, Y.-C., 1998. Micro-electro-mechanical-systems (MEMS) and fluid flows. *Annual Review of Fluid Mechanics*, 30(1), pp.579–612.
- Hsia, Y.-T. & Domoto, G.A., 1983. An Experimental Investigation of Molecular Rarefaction Effects in Gas Lubricated Bearings at Ultra-Low Clearances. *Journal of Lubrication Technology*, 105(1), p.120.
- Jakobsen, H.A., 2014. *Chemical reactor modeling: Multiphase reactive flows: Second edition*,
- Janicek, J.D. & Katz, D.L., 1995. Applications of unsteady state gas flow calculations. In *University of Michigan Research Conference*. Michigan.
- Javadpour, F., Fisher, D. & Unsworth, M., 2007. Nanoscale gas flow in shale gas sediments. *Journal of Canadian Petroleum Technology*, 46(10).
- Jones, S.C., 1997. A Technique for Faster Pulse-Decay Permeability Measurements in Tight Rocks. *SPE Formation Evaluation*, 12(1), pp.19–26.
- Kandlikar, S. et al., 2016. *Heat Transfer and Fluid Flow in Minichannels and Microchannels.*, Butterworth-Heinemann.
- Kardar, M., 2007. *Statistical physics of particles*, Cambridge University Press.
- Kennard, E., 1938. *Kinetic theory of gases : with an introduction to statistical mechanics* 1st ed., New York ;London: McGraw-Hill Book Co.

- Kim, S.H., Pitsch, H. & Boyd, I.D., 2008. Accuracy of higher-order lattice Boltzmann methods for microscale flows with finite Knudsen numbers. *Journal of Computational Physics*, 227(19), pp.8655–8671.
- Klinkenberg, L.J., 1941. The Permeability Of Porous Media To Liquids And Gases. *Drilling and Production Practice*, 1.
- Koch, D. & Ladd, A., 1997. Moderate Reynolds number flows through periodic and random arrays of aligned cylinders. *Journal of Fluid Mechanics*.
- Lee, S. & Yang, J., 1997. Modeling of Darcy-Forchheimer drag for fluid flow across a bank of circular cylinders. *International journal of heat and mass transfer*.
- Lee, T. & Lin, C.-L., 2005. Rarefaction and compressibility effects of the Lattice-Boltzmann-equation method in a gas microchannel. *Physical Review E*, 71(4), p.46706.
- Lim, C.Y. et al., 2002. Application of lattice Boltzmann method to simulate microchannel flows. *Physics of Fluids*, 14(7), p.2299.
- Liu, X., Civan, F. & Evans, R., 1995. Correlation of the non-Darcy flow coefficient. *of Canadian Petroleum Technology*.
- Lockerby, D.A., Reese, J.M. & Gallis, M.A., 2005. The usefulness of higher-order constitutive relations for describing the Knudsen layer. *Physics of Fluids*, 17(10), p.100609.
- Macdonald, I.F. et al., 1979. Flow through porous media-the Ergun equation revisited. *Industrial & Engineering Chemistry Fundamentals*, 18(3), pp.199–208.
- Mei, C.C. & Auriault, J.-L., 1991. The effect of weak inertia on flow through a porous medium. *Journal of Fluid Mechanics*, 222(1), p.647.
- Mei, R. et al., 2000. Lattice Boltzmann method for 3-D flows with curved boundary. *Journal of Computational Physics*, 161(2), pp.680–699.
- Meng, J., Zhang, Y. & Shan, X., 2011. Multiscale lattice Boltzmann approach to modeling gas flows. *Physical Review E*, 83(4), p.46701.
- Mitsuya, Y., 1993. Modified Reynolds equation for ultra-thin film gas lubrication using 1.5-order slip-flow model and considering surface accommodation coefficient. *Journal of Tribology*, 115(2), p.289.
- Mohamad, A.A., 2011. *Lattice Boltzmann Method*, London: Springer London.
- Muljadi, B. et al., 2015. The impact of porous media heterogeneity on non-Darcy flow behaviour from pore-scale simulation. *Advances in Water Resources*.
- Muljadi, B.P. et al., 2016. The impact of porous media heterogeneity on non-Darcy flow behaviour from pore-scale simulation. *Advances in Water Resources*, 95, pp.329–340.
- Newman, M. & Yin, X., 2013. Lattice Boltzmann simulation of non-Darcy flow in stochastically generated 2D porous media geometries. *SPE Journal*.
- Nie, X., Doolen, G.D. & Chen, S., 2002. Lattice-Boltzmann simulations of fluid flows in MEMS. *Journal of Statistical Physics*, 107(1/2), pp.279–289.
- Ohwada, T., Sone, Y. & Aoki, K., 1989. Temperature jump and Knudsen layer in a rarefied

- gas over a plane wall: Numerical analysis of the linearized Boltzmann equation for hard-sphere molecules. *Physics of Fluids A: Fluid Dynamics*, 1(2), p.363.
- Ohwada, T. & Kobayashi, S., 2004. Management of discontinuous reconstruction in kinetic schemes. *Journal of Computational Physics*, 197(1), pp.116–138.
- Oran, E.S., Oh, C.K. & Cybyk, B.Z., 1998. Direct simulation Monte Carlo: Recent advances and applications. *Annual Review of Fluid Mechanics*, 30(1), pp.403–441.
- Pan, C. & Miller, C.T., 2006. An evaluation of lattice Boltzmann schemes for porous medium flow simulation. *Computers & Fluids*, 35(8), pp.898–909.
- Piekos, E.S. & Breuer, K.S., 1996. Numerical Modeling of Micromechanical Devices Using the Direct Simulation Monte Carlo Method. *Journal of Fluids Engineering*, 118(3), p.464.
- Rao, P., 2015. *Kinetically Consistent Thermal Lattice Boltzmann Models*. University of Pittsburgh.
- Rojas, S. & Koplik, J., 1998. Nonlinear flow in porous media. *Physical Review E*, 58(4), pp.4776–4782.
- Ruth, D. & Ma, H., 1992. On the derivation of the Forchheimer equation by means of the averaging theorem. *Transport in Porous Media*, 7(3), pp.255–264.
- Sanaei, A. et al., 2015. A Novel Correlation for Prediction of Gas Viscosity. *Energy Sources, Part A: Recovery, Utilization, and Environmental Effects*, 37(18), pp.1943–1953.
- Schamberg, R., 1947. *The fundamental differential equations and the boundary conditions for high speed slip-flow, and their application to several specific problems*. California Institute of Technology.
- Seguin, D. et al., 1998. Experimental characterization of flow regimes in various porous media—II: Transition to turbulent regime. *Chemical engineering science*, 53(22), pp.3897–3909.
- Shan, X., 2010. General solution of lattices for Cartesian lattice Bhatnagar-Gross-Krook models. *Physical Review E*, 81(3), p.36702.
- Shan, X., Yuan, X.-F. & Chen, H., 2006. Kinetic theory representation of hydrodynamics: a way beyond the Navier–Stokes equation. *Journal of Fluid Mechanics*, 550(1), p.413.
- Sreekanth K., A., 1969. Slip flow of nitrogen gas through long circular tubes, measuring mass flow, pressure drop and cross sectional velocity profiles. In *Rarefied Gas Dynamics, Sixth International Symposium*. Cambridge: Academic Press, Inc., New York, United States.
- Suga, K. et al., 2010. Evaluation of a lattice Boltzmann method in a complex nanoflow. *Physical Review E*, 82(1), p.16701.
- Sukop, M.C. et al., 2013. Evaluation of permeability and non-Darcy flow in vuggy macroporous limestone aquifer samples with lattice Boltzmann methods. *Water Resources Research*, 49(1), pp.216–230.
- Szalmás, L. et al., 2007. Knudsen layer theory for high-order lattice Boltzmann models.

- Europhysics Letters (EPL)*, 80(2), p.24003.
- Takeuchi, S., Nakashima, S. & Tomiya, A., 2008. Permeability measurements of natural and experimental volcanic materials with a simple permeameter: Toward an understanding of magmatic degassing processes. *Journal of Volcanology and Geothermal Research*, 177(2), pp.329–339.
- Tang, G.H., He, Y.L. & Tao, W.Q., 2007. Comparison of gas slip models with solutions of linearized Boltzmann equation and direct simulation of Monte Carlo method. *International Journal of Modern Physics C*, 18(2), pp.203–216.
- Tang, G.H., Tao, W.Q. & He, Y.L., 2005a. Gas slippage effect on microscale porous flow using the lattice Boltzmann method. *Physical Review E*, 72(5), p.56301.
- Tang, G.H., Tao, W.Q. & He, Y.L., 2005b. Lattice Boltzmann method for gaseous microflows using kinetic theory boundary conditions. *Physics of Fluids*, 17(5), p.58101.
- Thauvin, F. & Mohanty, K., 1998. Network modeling of non-Darcy flow through porous media. *Transport in Porous Media*.
- Wang, X., Thauvin, F. & Mohanty, K., 1999. Non-Darcy flow through anisotropic porous media. *Chemical Engineering Science*.
- Xu, K., 2001. A Gas-Kinetic BGK Scheme for the Navier–Stokes Equations and Its Connection with Artificial Dissipation and Godunov Method. *Journal of Computational Physics*, 171(1), pp.289–335.
- Xu, K. & Li, Z., 2004. Microchannel flow in the slip regime: gas-kinetic BGK–Burnett solutions. *Journal of Fluid Mechanics*, 513, pp.87–110.
- Yan, F. & Farouk, B., 2002. Numerical Simulation of Gas Flow and Mixing in a Microchannel Using the Direct Simulation Monte Carlo Method. *Microscale Thermophysical Engineering*, 6(3), pp.235–251.
- Zhang, P. et al., 2015. Micro/Nano-pore network analysis of gas flow in shale matrix. *Scientific Reports*, 5, p.13501.
- Zhang, R., Shan, X. & Chen, H., 2006. Efficient kinetic method for fluid simulation beyond the Navier-Stokes equation. *Physical Review E*, 74(4), p.46703.
- Zhang, Y., Qin, R. & Emerson, D.R., 2005. Lattice Boltzmann simulation of rarefied gas flows in microchannels. *Physical Review E*, 71(4), p.47702.
- Zhang, Y.H. et al., 2005. Gas Flow in Microchannels – A Lattice Boltzmann Method Approach. *Journal of Statistical Physics*, 121(1–2), pp.257–267.
- Zheng, Y., Garcia, A.L. & Alder, B.J., 2002. Comparison of Kinetic Theory and Hydrodynamics for Poiseuille Flow. *Journal of Statistical Physics*, 109(3/4), pp.495–505.

APPENDIX A

Hermite polynomials are a set of orthogonal polynomials. These polynomials are expressed as:

$$H_n(x) = (-1)^n e^{x^2} \frac{d^n e^{-x^2}}{dx^n} \quad (\text{A.1})$$

The first five Hermite polynomials in one-dimensional space are:

$$H_0(x) = 1 \quad (\text{A.2})$$

$$H_1(x) = x \quad (\text{A.3})$$

$$H_2(x) = x^2 - 1 \quad (\text{A.4})$$

$$H_3(x) = x^3 - 3x \quad (\text{A.5})$$

$$H_4(x) = x^4 - 6x^2 + 3 \quad (\text{A.6})$$

where x is scalar. The Hermite polynomials are orthogonal with respect to the weight function:

$$\omega(x) = e^{-\frac{x^2}{2}} \quad (\text{A.7})$$

A function $f(x)$ is called square integrable if the integral:

$$\int_{-\infty}^{+\infty} |f(x)|^2 dx$$

is finite. Any square integrable function can be expanded on Hermite polynomial bases as:

$$f(x) = \sum_{n=0}^{\infty} a_n H_n(x) \quad (\text{A.8})$$

here a_n is calculated as:

$$a_n = \frac{1}{2^n n! \sqrt{\pi}} \int_{-\infty}^{+\infty} e^{-x^2} f(x) H_n(x) dx \quad (\text{A.9})$$

The tensor equivalence of the Hermite polynomials were introduced by Grad (1949) as:

$$\mathbf{H}^{(0)}(\vec{x}) = 1 \quad (\text{A.10})$$

$$\mathbf{H}^{(1)}(\vec{x}) = H_i^{(1)} = x_i \quad (\text{A.11})$$

$$\mathbf{H}^{(2)}(\vec{x}) = H_{ij}^{(2)} = x_i x_j - \delta_{ij} \quad (\text{A.12})$$

$$\mathbf{H}^{(3)}(\vec{x}) = H_{ijk}^{(3)} \quad (\text{A.13})$$

$$= x_i x_j x_k - x_i \delta_{jk} - x_j \delta_{ik} \\ - x_k \delta_{ij}$$

where $\vec{x} = x_i \vec{e}_i$ and \vec{e}_i is the unit vector of Cartesian co-ordinates. The recurrence relationship of Hermite polynomials relate different orders as:

$$x_i \mathbf{H}^{(n)}(\vec{x}) = \mathbf{H}^{(n+1)}(\vec{x}) + \delta_i \mathbf{H}^{(n-1)}(\vec{x}) \quad (\text{A.14})$$

The particle distribution function is a square integrable function. Therefore it could be expanded on Hermite polynomial bases as:

$$f(\vec{c}, \vec{x}, t) = \sum_{n=0}^{\infty} \mathbf{a}^{(n)}(\vec{x}, t) \mathbf{H}^{(n)}(\vec{c}) \quad (\text{A.15})$$

Here the expansion coefficients are calculated as:

$$\mathbf{a}^{(n)}(\vec{x}, t) = \int f(\vec{c}, \vec{x}, t) \mathbf{H}^{(n)}(\vec{c}) d\vec{c} \quad (\text{A.16})$$

Shan *et al.* (2006) showed that the particle distribution function can be expanded by using a finite number of terms of the series on the right hand side of equation A.15 without losing any information on the description of thermodynamics and hydrodynamics of the system.

$$f(\vec{c}, \vec{x}, t) \cong \sum_{n=0}^N \mathbf{a}^{(n)}(\vec{x}, t) \mathbf{H}^{(n)}(\vec{c}) \quad (\text{A.17})$$

where N is a finite integer.

APPENDIX B

In this section the mathematical model of the flow process in the falling head permeameter is developed. Figure A-1 represents the simple schematic of the flow test apparatus.

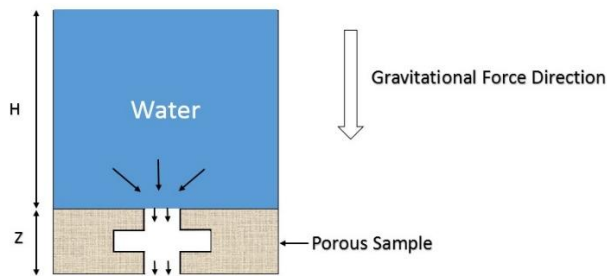


Figure B-1: The schematic of the falling head permeameter apparatus. H is the height of the water tank to be drained through the porous sample. Z is the height of the sample. Arrows represent the flow direction.

As seen in figure A-1, there is a tank filled with water on the top of the porous sample. The volume of the tank was measured by geometrical analysis (*i.e.* volume = area \times height). The tank and porous sample were filled with water at the initial point. As the experiment started, the water in the tank was allowed to drain through the sample and the time needed for all the volume of the water to drain was measured. This process was repeated several times and an average total time was measured to be used for permeability calculation. By Darcy's law the flow rate through the porous sample is:

$$Q = \frac{kA}{\mu} \frac{(-\Delta P + \rho g \Delta z)}{Z} \quad (\text{B.1})$$

Where A is the porous sample area. Pressure difference of the two faces of the sample is caused by the head of the water in the tank as:

$$-\Delta P = \frac{\rho V}{A_t} \quad (\text{B.2})$$

Where V is the volume of the water in the tank, ρ is the density of water and A_t is the inner cross sectional area of the tank. The volumetric flow rate of water through the porous sample is equal to the volume change of the water in the tank. Combining equations A.1 and A.2 and replacing volumetric flow rate with gradient of V with time (t) leads to:

$$Q = -\frac{dV}{dt} = \frac{kA}{\mu} \left(\frac{\rho V}{A_t Z} + \rho g \right) = \frac{kA}{\mu} \frac{\rho V}{A_t Z} + \frac{kA \rho g}{\mu} \quad (\text{B.3})$$

As the initial condition, at state $t=0$, the volume of the tank was calculated to be $314.3 \times 10^{-6} \text{ m}^3$. Therefore, equation A.3 could be solved with the initial condition to produce:

$$V(t) = 294 * 10^{-6} e^{-\frac{A k \rho}{A_t \mu Z} t} - 19.77 * 10^{-6} \quad (\text{B.4})$$

Rearranging equation A.4 will lead to equation 3.47.

APPENDIX C

In this section the semi-log plots of scaled permeability versus mass flow rate for the pipe-sphere, bent pipe and throat structures in table 5-1 are represented by figures B.1 to B.3.

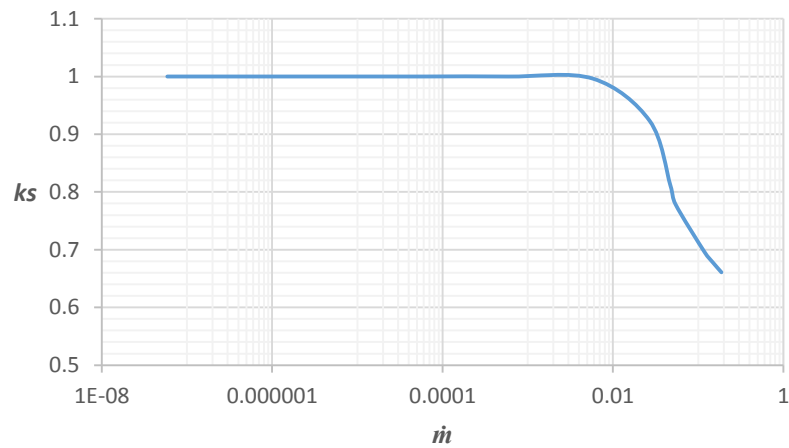


Figure C-1: The semi-log plots of mass flow rate in lattice units and scaled permeability for the pipe-sphere structure in table 5-1.

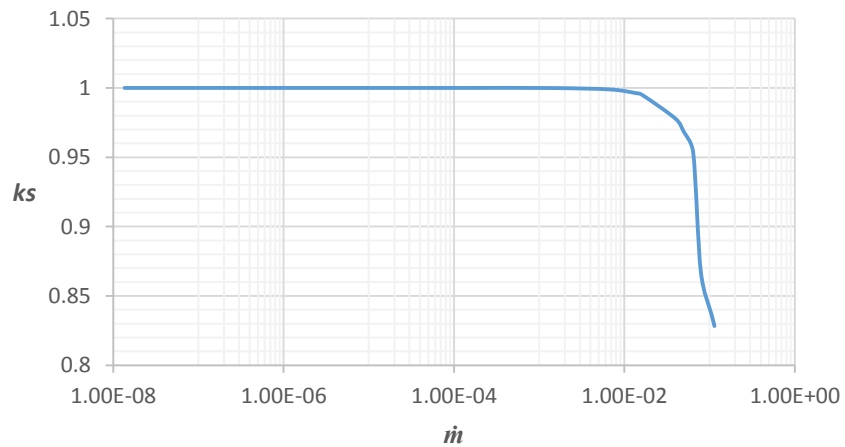


Figure C-2: The semi-log plots of mass flow rate in lattice units and scaled permeability for the bent channel structure in table 5-1.

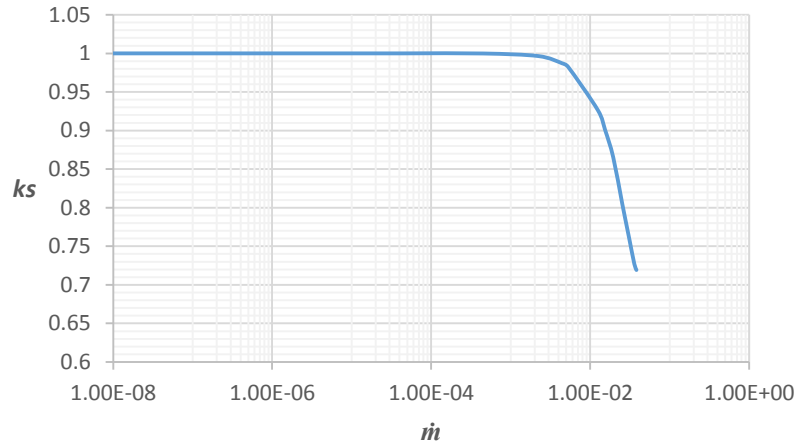


Figure C-3: The semi-log plots of mass flow rate in lattice units and scaled permeability for the throat structure in table 5-1.

In this part the LBM results of the scaled permeability and mass flow rate relationship and the best fit with equation 5.1 are presented.

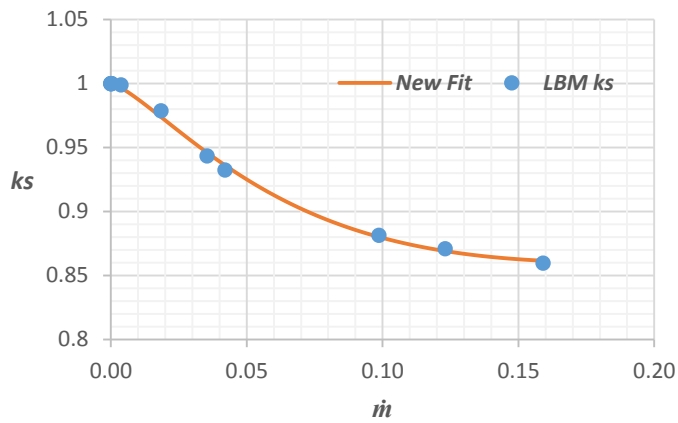


Figure C-4: The plot of mass flow rate in lattice units and scaled permeability predicted by LBM simulation for the pipe-sphere structure fitted with equation 5.1.

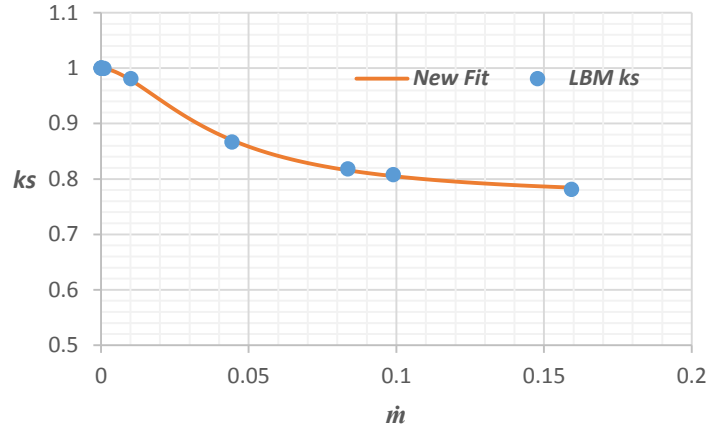


Figure C-5: The plot of mass flow rate in lattice units and scaled permeability predicted by LBM simulation for the pipe-cube structure fitted with equation 5.1.

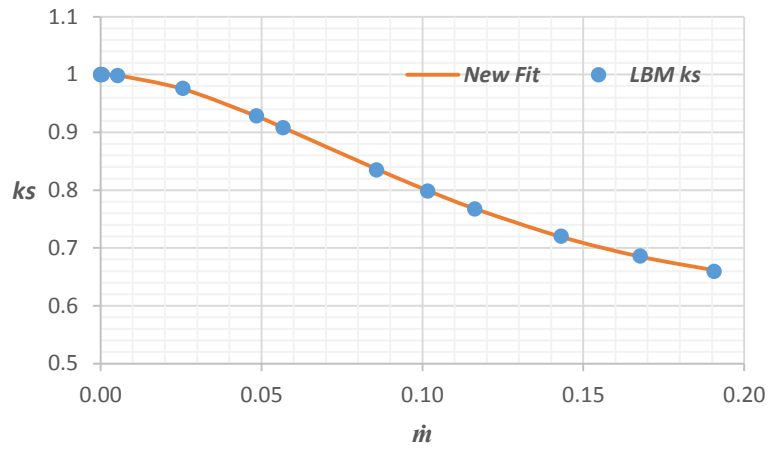


Figure C-6: The plot of mass flow rate in lattice units and scaled permeability predicted by LBM simulation for the pipe-ellipsoid structure fitted with equation 5.1.

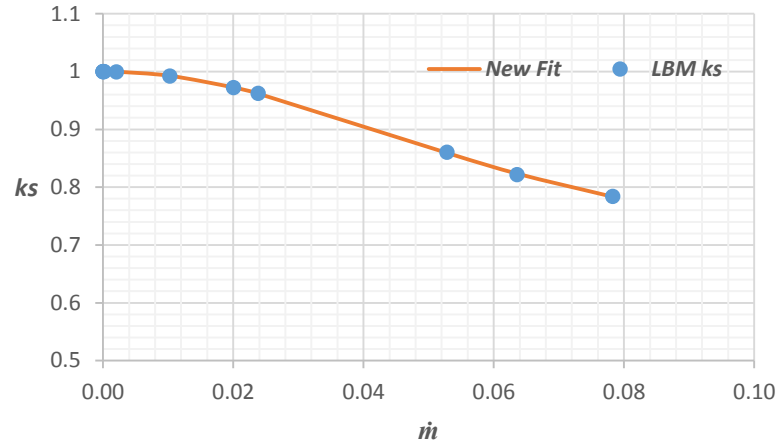


Figure C-7: The plot of mass flow rate in lattice units and scaled permeability predicted by LBM simulation for the bent channel structure fitted with equation 5.1.

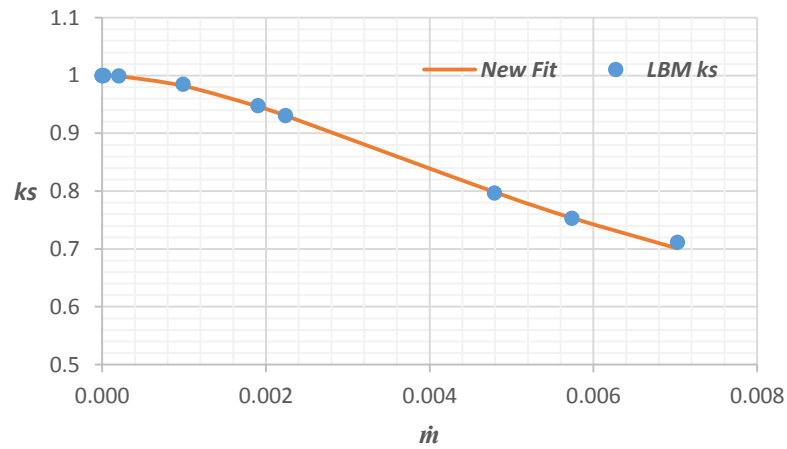


Figure C-8: The plot of mass flow rate in lattice units and scaled permeability predicted by LBM simulation for the throat structure fitted with equation 5.1.